

Fast electrostatic microinstability evaluation in arbitrary toroidal magnetic geometry using a variational approach

M.C.L. Morren,¹ P. Mulholland,¹ J.H.E. Proll,^{1,2} M.J. Pueschel,^{1,3,4} L. Podavini,² D.D. Kiszkiel,¹ J.A. Schuurmans,¹ and A. Zocco²

¹*Department of Applied Physics and Science Education, Eindhoven University of Technology, 5600 MB Eindhoven, The Netherlands*

²*Max-Planck-Institut für Plasmaphysik, 17491 Greifswald, Germany*

³*Dutch Institute for Fundamental Energy Research, 5612 AJ Eindhoven, The Netherlands*

⁴*Department of Physics & Astronomy, Ruhr-Universität Bochum, 44780 Bochum, Germany*

(*Electronic mail: m.c.l.morren@tue.nl)

(Dated: 5 December 2025)

Small-scale turbulence originating from microinstabilities limits the energy confinement time in magnetic confinement fusion. Here we develop a semi-analytical dispersion relation based on lowest-order solutions to the gyrokinetic equations in an asymptotic expansion in the ratio of transit (bounce) frequency to the mode frequency for ions (electrons), capable of describing two common instabilities: the ion temperature gradient (ITG) mode and trapped-electron mode (TEM), in the electrostatic limit. The dispersion relation, which is valid in arbitrary toroidal geometry, takes into account resonances with the magnetic ion and bounce-averaged electron drifts, incorporates non-local effects along the magnetic field line, is valid for arbitrary sign of the growth rate and magnetic curvature, and is shown to satisfy a variational property. Several common approximation models are introduced for both the magnetic drift and finite Larmor radius (FLR) damping, with the Padé approximation for FLR effect in particular resulting in remarkable agreement with the baseline dispersion relation model at significantly reduced costs. The baseline model is verified by comparing solutions of the dispersion relation model to high-fidelity linear gyrokinetic simulations, where the exact eigenfunction of the electrostatic potential from simulations is used as a trial function, showing good quantitative agreement for ITGs and TEMs in (shaped) tokamaks as well as low-magnetic-shear stellarators.

I. INTRODUCTION

For the successful exploitation of magnetic confinement fusion as an energy source, it is important that the extreme plasma conditions persist for a sufficiently long time. In both tokamaks and modern stellarators optimised for low neoclassical transport^{1,2}, the confinement losses are dominated by the anomalous transport channel. This transport is due to turbulent fluctuations, which are driven by microinstabilities in the plasma^{3,4}. In typical cases, most of the turbulent transport is driven by the ion-temperature gradient (ITG) mode and trapped-electron mode (TEM)^{5–8}, though in reactor-relevant scenarios, finite-pressure-gradient-driven magnetic instabilities such as kinetic ballooning modes (KBMs)^{9,10} or microtearing (MT)¹¹ modes may also contribute to turbulence-induced transport. Nevertheless, in the present work, we focus on the former class of electrostatic instabilities.

These microinstabilities can be investigated using (linear) gyrokinetics^{12–15}, which reveals a strong susceptibility to the magnetic geometry^{16–23}. In particular, TEMs, driven by resonances with the toroidal-precession drift of trapped electrons²⁴, may be avoided altogether in so-called maximum- J configurations^{25,26}, where all trapped particles experience a net-favourable bounce-averaged drift. While it is possible to design stellarators that provide a close approximation to such a maximum- J property^{27–29}, in tokamaks³⁰ and quasi-symmetric stellarators³¹ (both of which cannot be made maximum- J ³²), the stability of TEMs may alternatively be adjusted by reducing the trapped-particle fraction and modifying the cross-field drifts through flux-surface shaping. Likewise, the (toroidal) ITG instability is directly af-

ected by the magnetic geometry through the arrangement of bad-curvature regions and shear-enhanced finite-Larmor-radius (FLR) suppression^{33,34}.

It is thus clear that there is potential for optimising the magnetic geometry for increased resilience against these microinstabilities, especially for stellarators due to their substantial flexibility in magnetic-configuration space. For realistic geometries, detailed microstability investigations require direct numerical simulations using gyrokinetic codes. Whilst the involved linear calculations have relatively low computational cost in comparison to nonlinear simulations for the heat losses, they are still too computationally intense to be directly used inside optimisation routines, where instead simpler and cheaper geometry-based proxies for microstability have been opted for in the past^{35–39}. Noticeable exceptions include the work done by Refs. 40 and 41 where a quasi-linear mixing-length estimate and nonlinear heatflux of ITG, respectively, are directly included in the optimisation target, though both approaches necessitate an adiabatic treatment of electrons for numerical feasibility. Hence, there is a need for the development of fast reduced models to assess the stability of microturbulence.

Whilst in the past strides have been made to analytically investigate stability, in particular of ITG modes, these often rely on using “toy geometries” like a square drift-well embedded in a shearless constant magnetic field³⁴, or by invoking the so-called “local limit”^{42–45} where the variation of the geometry and eigenfunction along the field line are neglected. Only by invoking a non-resonant limit can effects of the geometry variation be retained in an analytically tractable form, though typically still requiring a simplification of the magnetic geometry

parameterisation^{33,43,44,46}. For TEMs, the salient geometric features are of much more importance due to the strong interplay between geometry and arrangement of trapped-particle populations, hence non-local treatments are rendered a necessity. Whilst binary statements regarding the existence of unstable TEMs in arbitrary toroidal geometry can be made using energy-budget calculations^{25,47,48}, obtaining quantitative growth rates in arbitrary geometry usually requires invoking a non-resonant expansion as well^{48,49}.

Here, we investigate the feasibility of a reduced-physics model for the dispersion relation of ITG and TEM, based on a lowest-order expansion of the collisionless electrostatic gyrokinetic system in the ratio of transit (bounce) frequency to the mode frequency for ions (electrons). The model retains gyrokinetic passing-ion and drift-kinetic (DK) trapped-electron responses to fluctuations in the electrostatic potential, includes impurities⁵⁰, is valid in arbitrary toroidal geometry, and accounts for non-local effects of the geometry along the magnetic field line. As a result of these approximations, the model lacks the physics associated with transit resonances, and essentially considers the passing electrons to be adiabatic, and therefore cannot describe the slab branch of the ITG mode^{33,51}, nor instabilities predominantly driven by passing electrons such as the electron-temperature gradient (ETG) mode^{5,51–55} or the universal instability (UI)^{47,56,57}. However, the model does allow for analytical treatment of kinetic resonances for both ions and electrons. Most importantly, we extend the validity range of these analytical expressions to arbitrary growth rate and curvature, where previous treatments typically implicitly assumed these to be positive. The model is *a posteriori* validated by comparing the growth rates and frequencies with those obtained from linear simulation with the GENE code⁵, using the exact gyrokinetic eigenfunctions as model input. To highlight the versatile geometry capabilities of the model, we consider a variety of realistic magnetic geometries based on experimental devices. These include the DIII-D tokamak⁵⁸, both positive- and negative-triangularity configurations of the TCV tokamak⁵⁹ (with equilibria corresponding to last closed-flux surface triangularities of $\delta_{LCFS} \approx \pm 0.4$), the standard quasi-symmetric configuration of the Helically Symmetric eXperiment (HSX) stellarator⁶⁰, and both the high- and negative-mirror configurations of the Wendelstein 7-X (W7-X) stellarator⁶¹. Here we will only present results for DIII-D, HSX and the high-mirror configuration of W7-X, with results for the remainder of configurations shown in the Supplementary Material.

The paper is organised as follows; in Section II, the collisionless electrostatic gyrokinetic system is briefly introduced and the dispersion relation model is derived. Next, in Section III, we describe the numerical solution strategy and normalisations used for solving the dispersion relation, as well as the setup of simulation parameters. We then present the results of the gyrokinetic simulations in Section IV, comparing these with the eigenfrequencies obtained by the dispersion model separately in the cases of adiabatic electrons (Section IV A) and kinetic electrons (Section IV B). Afterwards, in Section V we explore the feasibility of using further approximations for the FLR stabilisation and magnetic-drift resonance, aimed at

alleviating the need of numerical integration of the ion terms in the dispersion relation. These approximations allow for a fully analytical treatment of the ion terms, yielding simplified reduced versions of the dispersion relation with significantly lower computational costs. These reduced models are then subsequently tested against the baseline dispersion model to probe for the essential underlying physics necessary to resolve toroidal-instability drive. Lastly, in Section VI we provide a summary and brief outlook.

II. GYROKINETIC FORMULATION OF DISPERSION RELATION

The ITG and TEM microinstabilities may be described as electrostatic drift-wave fluctuations, hence we consider the $\beta \rightarrow 0$ limit of the gyrokinetic framework^{13,15}. Here $\beta = p/(B^2/2\mu_0)$, with p the total plasma pressure, μ_0 the vacuum permeability and B the magnetic field strength, expresses the ratio between kinetic- and magnetic pressures, such that magnetic fluctuations are neglected altogether in the electrostatic approximation ($\delta \mathbf{B} \approx 0$). Additionally, as we focus on microinstabilities responsible for core plasma turbulence we consider the collisionless limit. This collisionless electrostatic limit is commonly employed to describe both instabilities^{33,34,43,48,49}. However, both finite- β and finite collisionality tend to have a stabilising influence on the ITG and TEM^{10,62}, such that the modes governed by the collisionless electrostatic gyrokinetic system may be considered as upper bounds of instability.

The distribution function of each species s is split into equilibrium and fluctuating parts as

$$f_s(\mathbf{x}, \mathbf{v}, t) = F_{Ms}(\mathbf{x}, \mathbf{v}) \left(1 - \frac{q_s \phi(\mathbf{x}, t)}{T_s} \right) + g_s(\mathbf{R}, \mathbf{v}, t) \quad (1)$$

where the first term includes both the equilibrium Maxwellian distribution

$$F_{Ms}(\mathbf{x}, \mathbf{v}) = \frac{n_s(\mathbf{x})}{(\sqrt{2\pi}v_{Ts})^3} \exp\left(-\frac{v^2}{2v_{Ts}^2}\right) \quad (2)$$

and the adiabatic response. In Eqns. (1) and (2) n_s, T_s, q_s, m_s , and $v_{Ts} = \sqrt{T_s/m_s}$ denote the equilibrium density, equilibrium temperature, charge, mass and thermal velocity of species s , respectively, while $\mathbf{x}, \mathbf{v}, t$ denote position, velocity and time, respectively. Additionally, the last term in Eqn. (1) is the non-adiabatic response, which describes the distribution function of particle gyrocenters $\mathbf{R} = \mathbf{x} - \mathbf{e}_b \times \mathbf{v}/\Omega_s$, where $\mathbf{e}_b = \mathbf{B}/B$, with \mathbf{B} denoting the (equilibrium) magnetic flux density, $\Omega_s = q_s B/m_s$ the cyclotron frequency and $B = \|\mathbf{B}\|$. The gyrocenter distribution evolves according to the (linearised) gyrokinetic Vlasov equation¹²

$$v_{\parallel} \nabla_{\parallel} \hat{g}_s - i(\omega - \omega_{ds}) \hat{g}_s = -i \frac{q_s \hat{\phi}}{T_s} J_0(k_{\perp} \rho_s) (\omega - \omega_{*s}^T) F_{Ms} \quad (3)$$

where it has been assumed that we are dealing with low-frequency drift waves characterised by eigenfrequencies

$\omega/\Omega_s \ll 1$, and cross-field spatial scales λ_\perp much shorter than equilibrium length scales, $\lambda_\perp/a \ll 1$, with a the minor radius. With those conditions satisfied, each fluctuating quantity can be written as $\xi(\mathbf{x}, t) = \hat{\xi}(l) \exp(iS(\mathbf{x}) - i\omega t)$, where the eikonal e^{iS} describes the short-scale variation across the magnetic field, such that $\nabla S \cdot \mathbf{B} = 0$ and $\hat{\xi}(l)$ describes the long-scale variation of fluctuations along the magnetic field. Furthermore, in Eqn. (3), $\nabla_\parallel = \mathbf{e}_b \cdot \nabla$ is the differential operator along the field-line coordinate, $\omega_{ds} = \mathbf{k}_\perp \cdot \mathbf{v}_{ds}$ the magnetic drift frequency, where $\mathbf{k}_\perp = \nabla S$ is the perpendicular wavenumber, and $\mathbf{v}_{ds} = \mathbf{e}_b \times (\nabla_\parallel \kappa + v_\perp^2 \nabla \ln B/2)/\Omega_s$ is the magnetic drift velocity, with $\kappa = (\mathbf{e}_b \cdot \nabla) \mathbf{e}_b$ the magnetic curvature vector, and v_\parallel, v_\perp denote the velocity components decomposed with respect to their alignment to the magnetic field. Additionally, J_0 is the zeroth-order Bessel function of the first kind, $k_\perp = \|\mathbf{k}_\perp\|$ is the magnitude of the perpendicular wavenumber (such that $k_\perp \sim 1/\lambda_\perp$), $\rho_s = \|\mathbf{e}_b \times \mathbf{v}/\Omega_s\|$ the Larmor radius, such that $J_0(k_\perp \rho_s)$ describes the effect of gyroaveraging the fluctuations over the unperturbed particle orbit, and $\omega_{*s}^T = \omega_{\nabla n_s} + \omega_{\nabla T_s} (v^2/(2v_{Ts}^2) - 3/2)$ is the temperature-dependent diamagnetic frequency in terms of the two components of the pressure gradient $\omega_{\nabla\{n_s, T_s\}} = T_s(\mathbf{k}_\perp \times \mathbf{e}_b) \cdot \nabla \ln\{n_s, T_s\}/(q_s B)$, where $\omega_{\nabla n_s}$ is commonly referred to as the diamagnetic frequency. In interpreting Eqn. (3) as a one-dimensional differential equation in $\hat{g}_s(l)$ by introducing a perpendicular wavevector \mathbf{k}_\perp , the ballooning transform^{63–65} has been employed to reconcile the presence of sheared toroidal magnetic field lines with the periodicity constraint of Fourier modes.

The electrostatic potential is obtained self-consistently from Poisson's equation, which under reactor-relevant conditions where the length scales of interest far exceed the Debye length, reduces to a quasi-neutrality constraint on the density fluctuations $\delta n_s = \int (f_s - F_{Ms}) d^3 \mathbf{v}_s$

$$\sum_s \frac{q_s^2 n_s \hat{\phi}(\mathbf{x}, t)}{T_s} = \sum_s q_s \int \langle g_s(\mathbf{R}, \mathbf{v}, t) \rangle_{\mathbf{x}} d^3 \mathbf{v}_s \quad (4)$$

where $\langle \dots \rangle_{\mathbf{x}}$ denotes a ring-average over the gyrophase, performed at constant particle position⁶⁶. For the linear eigenmodes with strong spatial anisotropy with respect to the magnetic-field orientation considered here, Eqn. (4) reduces to a constitutive relation between the slowly varying parallel profiles (denoted by hats)

$$\sum_s \frac{q_s^2 n_s \hat{\phi}}{T_s} = \sum_s q_s \int J_0(k_\perp \rho_s) \hat{g}_s d^3 \mathbf{v}_s. \quad (5)$$

A. Approximate solutions and local dispersion relation

Whilst it is possible to find a general solution to Eqn. (3) in terms of an integrating factor⁶⁷, the resulting quasi-neutrality condition becomes expressed in terms of charge-density kernels⁶⁸, which tends to obscure some of the more salient physical features underlying the instability mechanisms due to their non-tractability (see e.g. Ref. 69 for such a general description of the ITG mode).

Instead here we focus on modes with characteristic frequencies ordered as

$$\omega_{bi} \ll \omega_{ri} \ll \omega \ll \omega_{be} \ll \omega_{te} \quad (6)$$

where ω_{bs} and respectively ω_{ts} represent the characteristic bounce- and transit frequencies of species s . The former is defined in terms of the time it takes a thermal trapped particle to bounce between regions of magnetic maxima on a flux surface, while the latter is defined in terms of the time it takes a thermal passing particle to traverse the connection length, i.e. the region between locations of good and bad magnetic curvature³³. In a tokamak, this simply corresponds to the distance along the field line between the inboard and outboard side, but can be considerably shorter in a stellarator. The frequency ordering of Eqn. (6) is equivalent to the condition for the mode to avoid strong Landau damping, and has also been considered in e.g. Refs. 21, 33, 44, 48, 49, 68–71. Applying the frequency ordering of Eqn. (6) to the gyrokinetic Vlasov equation [Eqn. (3)], we can obtain asymptotic solutions for \hat{g}_i and \hat{g}_e in the limit of $\omega_{ri}/\omega \sim \omega/\omega_{be} \ll 1$, which effectively weights the significance of the two terms of the left-hand side, as the streaming term $v_\parallel \nabla_\parallel$ can be associated with the bounce- and transit motion. For the ions by neglecting the streaming term to lowest order we straightforwardly obtain

$$\hat{g}_i \approx \frac{Z_i e \hat{\phi}}{T_i} \frac{\omega - \omega_{*i}^T}{\omega - \omega_{di}} J_0(k_\perp \rho_i) F_{Mi}, \quad (7)$$

where $Z_i = q_i/e$ is the charge number and e denotes the elementary charge. Meanwhile, for the electrons the streaming term dominates, and to lowest order the distribution \hat{g}_e is constant along the field line. By taking a bounce-average of the gyrokinetic Vlasov equation [Eqn. (3)], the electron gyrocenter distribution is found as⁷²

$$\hat{g}_e \approx \frac{-e}{T_e} \frac{\omega - \omega_{*e}^T}{\omega - \omega_{de}} \overline{J_0(k_\perp \rho_e) \hat{\phi}} F_{Me} \quad (8)$$

where $\overline{\dots}$ denotes the bounce-average (transit-average) operator

$$\overline{\dots} = \frac{\oint \frac{d(\dots)}{|v_\parallel|}}{\oint \frac{d\ell}{|v_\parallel|}},$$

where the integral is taken along subsequent bounce-points (along the entire field line), defined as the positions along the field line where $|v_\parallel| = \sqrt{2(E - \mu B(l))} = 0$, with $E = mv^2/2$ the particle kinetic energy and $\mu = mv_\perp^2/(2B)$ the magnetic moment, for trapped (passing) particles. We invoke one final approximation with regard to the spatial scales, where we consider modes characterised by $k_\perp \rho_{Ti} \sim \mathcal{O}(0.1) - \mathcal{O}(1)$ where $\rho_{Ti} = v_{Ti}/\Omega_i$ is the characteristic ion Larmor radius at thermal speed, which corresponds to the scales of interests where the bulk of the transport is typically observed in nonlinear simulations^{6,9,10,73–75}. At these scales, we may approximate $k_\perp \rho_e \approx 0$ in the argument of the Bessel function in Eqn. (8), thereby effectively treating the electrons drift-kinetically, as also considered in e.g. Refs. 48, 51, and 68.

As a result of these simplifying assumptions on the parameter regime, we effectively treat all ions as passing particles, thus ignoring the possibility of trapped-ion modes, though such instabilities would require much larger spatial scales than supported by our $k_\perp \rho_{Ti} \sim \mathcal{O}(0.1) - \mathcal{O}(1)$ ordering^{51,76}. Moreover, we effectively treat passing electrons adiabatically, as passing particles will experience a net vanishing perturbation $\hat{\phi} \rightarrow 0$ due to the finite extent of the modes along the field lines. Therefore, within the drift-kinetic (DK) treatment for

electrons, the non-adiabatic response of electrons [Eqn. (8)] vanishes for passing particles. As a consequence, short-wavelength (i.e. electron-scale) instabilities associated with drift-resonances from passing particles like ETG modes^{5,51–55} are absent from the model we present here. With these simplifications in mind, substituting Eqns. (7) and (8) into the quasi-neutrality constraint Eqn. (5) yields the following local dispersion relation

$$D_{\text{loc}}(\omega, \mathbf{k}_\perp, \{\text{geo}\}, \{\text{plasma}\}, l) = \left(1 + \sum_j \frac{Z_j^2 n_j}{n_e} \frac{T_e}{T_j} - \sum_j \frac{Z_j^2 n_j}{n_e} \frac{T_e}{T_j} \int \frac{\omega - \omega_{*j}^T}{\omega - \omega_{dj}(l)} \mathcal{F}_{Mj} J_0(k_\perp \rho_j(l))^2 d^3 \mathbf{v}_j \right) \hat{\phi}(l) - \int_{\text{trap}(l)} \frac{\omega - \omega_{*e}^T}{\omega - \omega_{de}} \hat{\phi} \mathcal{F}_{Me} d^3 \mathbf{v}_e = 0 \quad (9)$$

where the sum over j accounts for all ion species present in the plasma. In obtaining Eqn. (9) it has been assumed that the non-adiabatic part of the perturbed distribution function for all ion species can accurately be described by the gyrokinetic Vlasov equation [Eqn. (3)] and its approximate solution of Eqn. (7), as e.g. also considered in the impurity model of Ref. 45, which are benign assumptions for all but the heaviest of impurities (see⁵⁰). Henceforth, the subscript i shall exclusively refer to the main ion species. In Eqn. (9) we have introduced the single-particle Maxwellian as $\mathcal{F}_{Ms} = F_{Ms}/n_s$. This dispersion relation depends on the geometric parameterisation through the magnetic drifts, as well as the FLR damping terms of the ions, as the magnitude of the perpendicular wavevector $\mathbf{k}_\perp = k_\psi \nabla \psi + k_\alpha \nabla \alpha$ is determined by

$$k_\perp = \sqrt{g^{\psi\psi} k_\psi^2 + g^{\alpha\alpha} k_\alpha^2 + 2g^{\psi\alpha} k_\psi k_\alpha} \quad (10)$$

where $g^{mn} = \nabla x^m \cdot \nabla x^n$ are the components of the contravariant metric tensor, ψ the (poloidal) magnetic flux function and $\alpha = q\theta - \zeta$ the Clebsch angle, corresponding to the magnetic flux density $\mathbf{B} = \nabla \psi \times \nabla \alpha$. Additionally, θ, ζ denote the poloidal- and toroidal Boozer angles, respectively, while $q(\psi)$ is the inverse of the rotational transform, commonly known as the safety factor in tokamak literature⁷⁷. In Eqn. (9), the dependency on parameters like the plasma composition and kinetic profiles are combined in $\{\text{plasma}\}$, which like the magnetic-configuration dependency $\{\text{geo}\}$ are considered as external parameters set by macroscopic considerations. The trapped region of velocity space is delimited by pitch angles $\lambda = \mu/E = v_\perp^2/(v^2 B)$ in the range of $1/B_{\text{max}} \leq \lambda \leq 1/B(l)$, where B_{max} is the global maximum of the magnetic field strength on a flux surface, and depends on the position along the field line, hence the nomen “local” for Eqn. (9) despite the appearance of the bounce-averages.

By virtue of the approximations made above, we now gain physical insight regarding the underlying physics of the instabilities, for Eqn. (9) provides two singularities in the non-

adiabatic density fluctuations of ions ($\omega \approx \omega_{dj}$) and electrons ($\omega \approx \omega_{de}^T$), leading to the resonance conditions for the (toroidal) ITG and TEM, respectively. This, however, results in an oversimplified picture, where it is assumed that the mode frequency is purely real-valued $\omega = \omega_R$ (corresponding to a stable drift wave), while such electrostatic fluctuations must have a finite growth ($\gamma > 0$) or damping rate ($\gamma < 0$), per $\omega = \omega_R + i\gamma$, producing Landau damping in homogeneous plasmas⁷⁸, which can further be driven unstable at sufficiently large gradients⁵¹.

In order to solve the kinetic integrals analytically, the drift resonances need to be carefully resolved. We propose here a generalisation of the method introduced in Ref. 44 to resolve the ITG resonance in the DK limit, by writing the frequency denominators as

$$\frac{1}{\omega - \omega_{ds}} = \frac{1}{i\sigma_\gamma} \int_0^\infty d\xi e^{i\sigma_\gamma(\omega - \omega_{ds})\xi} \quad \text{iff } \text{Im}[\omega] \neq 0 \quad (11)$$

where $\sigma_\gamma = \text{sgn } \gamma = \pm 1$ ensures absolute convergence of the auxiliary integral, which is strictly evaluated along \mathbb{R}^+ , and therefore integrability of the resonance. A fundamental limitation of Eqn. (11), however, is that the right-hand side is undefined for pure drift waves with $\omega = \omega_R$, though the left hand-side is, with exception of the point $\omega_R = \omega_{ds}$. For a given ω_R , however, such a point will always occur while evaluating Eqn. (9), such that pure drift waves cannot constitute a valid solution to the dispersion relation. As conjectured above, solutions to the dispersion relation, which we seek to obtain using Eqn. (11), must thus have finite γ .

Typically, this auxiliary integral approach to integrate the resonance is only considered for unstable modes^{79–82}, in which case it reduces to the approach taken by Biglari, Diamond and Rosenbluth⁴⁴, hereafter referred to as BDR. We note that Eqn. (11) closely resembles the form used in Eqn 3.5 from Ref. 42 to similarly extend the applicability of the BDR approach to damped modes, where instead the upper bound

is considered to be $\sigma_\gamma \infty$ for robust numerical integration regardless of whether modes are damped or growing. Though, as we shall see in Section A, maintaining the integration path along the positive real line is beneficial when solving the resulting velocity integrals from the dispersion relation analytically.

After applying Eqn. (11) to Eqn. (9), the remainder of the derivation involves exchanging the order of integration between ξ and velocity-space variables, followed by a series of changes of integration variables, each tailored to maintain the absolute convergence that is guaranteed by Eqn. (11), and is deferred to Section A, resulting in

$$D_{\text{loc}}(\omega, k_\psi, k_\alpha, \{\text{geo}\}, \{\text{plasma}\}, l) = \left(1 + \sum_j \frac{Z_j^2 n_j}{n_e} \frac{T_e}{T_j} - \sum_j \frac{Z_j^2 n_j}{n_e} \frac{T_e}{T_j} \left[\Gamma_0(b_j) - \frac{\omega_{\nabla n_j} - \frac{3}{2} \omega_{\nabla T_j}}{\omega} J_j^{(0)}(\omega, \{\text{geo}\}, \mathbf{k}_\perp, l) \right. \right. \\ \left. \left. + \frac{\omega_{j, \nabla B} - \omega_{\nabla T_j}}{2\omega} J_{j, \perp}^{(2)}(\omega, \{\text{geo}\}, \mathbf{k}_\perp, l) + \frac{\omega_{j, \kappa} - \frac{\omega_{\nabla T_j}}{2}}{\omega} J_{j, \parallel}^2(\omega, \{\text{geo}\}, \mathbf{k}_\perp, l) \right] \right) \hat{\phi}(l) - B(l) \int_{1/B_{\text{max}}}^{1/B(l)} d\lambda \frac{\bar{\hat{\phi}}(\lambda)}{\sqrt{1 - \lambda B(l)}} \times \\ \left[\frac{1}{2} + \frac{3}{4} \frac{\overline{\omega_{de}^T}(\lambda) - \omega_{\nabla T_e}}{\omega} J_{\text{tr-el}}^{(2)}(\omega, \lambda, \{\text{geo}\}, \mathbf{k}_\perp) - \frac{\omega_{\nabla n_e} - \frac{3}{2} \omega_{\nabla T_e}}{2\omega} J_{\text{tr-el}}^{(1)}(\omega, \lambda, \{\text{geo}\}, \mathbf{k}_\perp) \right] = 0. \quad (12)$$

In Eqn. (12) we have absorbed the variation of \mathbf{k}_\perp due to the metric into the geometric dependency $\{\text{geo}\}$, while $\omega_{s, \kappa} = \mathbf{k}_\perp \cdot (\mathbf{e}_b \times \kappa) v_{Ts}^2 / \Omega_s$ and $\omega_{s, \nabla B} = \mathbf{k}_\perp \cdot (\mathbf{e}_b \times \nabla \ln B) v_{Ts}^2 / \Omega_s$ are the usual thermal curvature and ∇B components of the magnetic drift frequency, $b_j = (k_\perp \rho_{Tj})^2$ represents the magnitude of the perpendicular wavenumber normalised to thermal ion Larmor radius, and $\Gamma_n(z) = \exp(-z) I_n(z)$ denotes the exponentially scaled n^{th} -order modified Bessel functions of the first kind. Additionally, we have used an energy and pitch angle representation of velocity space for electrons, such that the bounce-average operator

$$\overline{\cdots} = \frac{\oint \frac{dl}{\sqrt{1 - \lambda B(l)}} (\cdots)}{\oint \frac{dl}{\sqrt{1 - \lambda B(l)}}} \quad (13)$$

becomes a function of pitch angle only, and $\omega_{de}^T(\lambda, l) = 2\omega_{e, \kappa}(l)(1 - \lambda B(l)) + \omega_{e, \nabla B}(l)\lambda B(l)$ is the orbit-modulated total drift frequency of an electron at thermal energy $E = T_e$ with pitch angle λ . In Eqn. (12), the following ion integrals appear associated with the drift resonance:

$$J_j^{(0)} = \frac{\omega}{i\sigma_\gamma} \int_0^\infty d\xi \frac{e^{i\sigma_\gamma \omega \xi} \Gamma_0(\hat{b}_j(\xi))}{\sqrt{1 + 2i\sigma_\gamma \omega_{j, \kappa} \xi} (1 + i\sigma_\gamma \omega_{j, \nabla B} \xi)} \\ J_{j, \perp}^{(2)} = \frac{2\omega}{i\sigma_\gamma} \int_0^\infty d\xi \frac{e^{i\sigma_\gamma \omega \xi} (\Gamma_0(\hat{b}_j(\xi)) + \hat{b}_j(\xi) [\Gamma_1(\hat{b}_j(\xi)) - \Gamma_0(\hat{b}_j(\xi))])}{\sqrt{1 + 2i\sigma_\gamma \omega_{j, \kappa} \xi} (1 + i\sigma_\gamma \omega_{j, \nabla B} \xi)^2} \\ J_{j, \parallel}^{(2)} = \frac{\omega}{i\sigma_\gamma} \int_0^\infty d\xi \frac{e^{i\sigma_\gamma \omega \xi} \Gamma_0(\hat{b}_j(\xi))}{(1 + 2i\sigma_\gamma \omega_{j, \kappa} \xi)^{3/2} (1 + i\sigma_\gamma \omega_{j, \nabla B} \xi)} \quad (14)$$

where $\hat{b}_j(\xi) = b_j / (1 + i\sigma_\gamma \omega_{j, \nabla B} \xi)$. Likewise, in Eqn. (12) we have introduced the resonant electron integrals

$$J_{\text{tr-el}}^{(1)} = -2 \left(a_e + a_e^{3/2} \sigma_\gamma \sigma_{de} Z(\sigma_\gamma \sigma_{de} \sqrt{a_e}) \right), \quad (15) \\ J_{\text{tr-el}}^{(2)} = -2 \left(\frac{a_e}{3} (1 + 2a_e) + \frac{2}{3} a_e^{5/2} \sigma_\gamma \sigma_{de} Z(\sigma_\gamma \sigma_{de} \sqrt{a_e}) \right),$$

where $a_e = \omega / \overline{\omega_{de}^T}$, and $\sigma_{de} = \text{sgn} \overline{\omega_{de}^T}$, and the plasma dispersion function $Z(\zeta) = i\sqrt{\pi} \mathcal{W}(\zeta)$ here appears explicitly in

the form of its fundamental definition in terms of the Faddeeva function⁸³ $\mathcal{W}(\zeta) = \exp(-\zeta^2) \text{erfc}(-i\zeta)$. We note that the kinetic-ion-related terms from Eqns. (12) and (14) match with the expressions given in Appendix A of Ref. 43 – corrected for the typo $J_{j, \parallel}^2 \leftrightarrow J_{j, \perp}^2$ that was recently also identified by Ref. 84 – in the case of $\sigma_\gamma = +1$, consistent with their use of the original BDR approach to integrate the resonant denominator. Meanwhile, the trapped-electron-related terms in Eqns. (12) and (15) match with Eqn. (25) of Ref. 68 in the case

of $\sigma_\gamma \sigma_{de} = +1$. Here, this discrepancy is caused by the use in Ref. 68 of the integral representation of the plasma dispersion function

$$Z(\zeta) = \frac{1}{\sqrt{\pi}} \int_{-\infty}^{\infty} \frac{\exp(-z^2)}{z - \zeta} dz \quad \text{iff } \text{Im}[\zeta] > 0 \quad (16)$$

as defined by Fried and Conte⁸⁵, though this representation suffers from the restriction that it is only valid in the upper half-plane, unlike the definition in terms of a scaled Faddeeva function used throughout this work, which is valid throughout the complex plane⁸³. In the context of Laplace-Fourier transform for the distribution function and potential fluctuations the plasma dispersion function is commonly analytically continued to extend application of Eqn. (16) to damped fluctuations^{42,86,87}. However, we omit such an approach in this work as the resulting damped fluctuations do not correspond to pure eigenmodes of the linear gyrokinetic system, which contradicts our prior fluctuation ansatz of $\xi(\mathbf{x}, t) \propto \xi(\mathbf{x})e^{-i\omega t}$ for all fluctuating quantities. Meanwhile, pure damped eigenmodes of the linear gyrokinetic system do exist and are known to play an important role in turbulence saturation through nonlinear interactions^{88,89}, and are hence of interest to model. Regardless of the approach taken to model damped fluctuations, the validity constraint of Eqn. (16) is nonetheless restrictive in the accurate modelling of unstable modes – which is the main use case of the model in Section IV – for among the various trapping wells along the field line the bounce-averaged trapped-electron drift, appearing in the argument of the plasma dispersion function in Eqn. (15), will change its sign in some regions. This influence of the magnetic drift on the validity plasma dispersion function is often disregarded, though noticeable exceptions are the work from Ref. 87, which considers a similar sign generalisation of $Z(\zeta) = \sigma Z(\sigma\zeta)$ where $\sigma = \text{sgn Im}[\zeta]$ in the context of ITG modes, and the TEM model recently developed by Ref. 90 where the role of $\text{sgn } \overline{\omega_{de}^T}$ (equivalent to ε in their notation) has been accounted for in the evaluation of the plasma dispersion function, though their TEM model neglects the role of kinetic ions and is limited to geometry of shaped tokamaks.

Additionally, we note that using our form of the plasma dispersion function as in Eqn. (15), is crucial to satisfy the fundamental property that the trapped-electron energy integral $I_{\text{tr-el}}$ [see Eqn. (A9)] is complex-conjugate symmetric, i.e. it has the property that $I_{\text{tr-el}}(\omega^*) = [I_{\text{tr-el}}(\omega)]^*$, with $*$ denoting the complex conjugate, as can readily be proven using the symmetry property of the Faddeeva function⁸³ $\mathcal{W}(\zeta^*) = [\mathcal{W}(-\zeta)]^*$. Similar considerations regarding complex-conjugate symmetry also hold for the resonant ion velocity integrals (i.e. the first term in square brackets in Eqn. (12)).

Lastly, before continuing with presenting the global dispersion model, we briefly remark about the influence of transit resonances due to the streaming term in the gyrokinetic Vlasov equation [Eqn. (3)]. One particular analytically tractable case, is that of a plasma in a constant and unshaped magnetic field. In such a slab geometry fluctuations do not resonate with the magnetic drift frequency, but may resonate with the transit frequency $\omega \approx \omega_{ts} = k_{\parallel} v_{Ts}$ where $k_{\parallel} = 2\pi/L_{\parallel}$

is the wavenumber of fluctuations aligned with the magnetic field. For completeness the derivation of the dispersion relation belonging to such slab-ITG modes is presented in Section B, and can be similarly expressed in terms of the sign generalised plasma dispersion function as occur in our prescription of the trapped-electron resonant integral Eqn. (15). In literature the effect of transit resonances on the curvature-driven, i.e. toroidal, ITG mode is often modelled by modifying the resonant denominator in Eqn. (7) to $1/(\omega - \omega_{ds} - k_{\parallel} v_{\parallel})$ creating quasi-local models^{42,79,80,82,86,91,92}. While forming a perfect analogy to the slab-branch of ITG instability, it should be noted that the use of a parallel wavenumber is formally ill-founded as the geometry is varying along the field line, and such a k_{\parallel} should be considered as an ad-hoc effective parallel wavenumber meant to heuristically reincorporate the effects of Landau resonances in a toroidal system, while a proper inclusion of streaming effects in a toroidal system requires k_{\parallel} to be considered as the streaming operator.

B. Global dispersion relation

We now turn our attention to a problematic issue in the local dispersion relation, which makes Eqn. (12) inadequate for obtaining meaningful eigenfrequencies in toroidal geometry. If we consider a location along a field line in close proximity of B_{max} , the trapped-electron response will vanish and Eqn. (12) reduces to the form $D_{\text{loc}} = h(\omega, \{\text{geo}\}, \{\text{plasma}\}, l_{\text{max}}) \times \hat{\phi}(l_{\text{max}}) = 0$, where l_{max} is (one of) the position(s) along the field line where the $B(l) = B_{\text{max}}$, which has either the trivial solution that the eigenmode must vanish at l_{max} consistent with an instability driven solely by trapped electrons, or we obtain a family of purely local eigenmode solutions $\omega(l_{\text{max}})$ determined by the plasma composition and local geometry at l_{max} . In the class of (approximately) omnigenous devices of interest for fusion applications, there will be multiple equivalent magnetic maxima, all spread equidistantly along the field line^{93,94}. However, in the presence of finite (global) magnetic shear $dq/d\psi$, the perpendicular wavevector \mathbf{k}_{\perp} is secular (i.e. increasing along the field line without bound)^{33,95}, resulting in neither the FLR damping nor the magnetic drift being equivalent between these magnetic maxima. Consequently, this local family of eigenfrequency solutions becomes disjoint between the various magnetic maxima. This problem is further exacerbated in the limit of the adiabatic electron model, in which case the trapped-electron contribution to Eqn. (12) vanishes altogether, propagating the locality issue to all points on the field line as $D_{\text{loc}} = 0$ reduces to $h(\omega, \{\text{geo}\}, \{\text{plasma}\}, l) = 0$, yielding purely local eigenfrequency solutions $\omega_{\text{loc}}(l)$ determined solely by the local geometry. The variation of these local solutions can be quite significant, even in the axisymmetric limit where the connection length (proportional to the characteristic length scale of variation in the geometry along the field line) is much larger than in a typical stellarator³³, see Figure 1. The interplay between drive (magnetic drift) and damping factors (FLR effects) is clear, with the (local) propagation frequency ω_R adjusting itself to the profile of the magnetic drift to maximise the resonance $\omega_R \approx \omega_{di}$ in the thermal bulk

of the distribution, whilst the (local) growth rate decreases as $\|\mathbf{k}_\perp\|$ increases away from $\theta = 0$ (corresponding to the out-board midplane) due to FLR damping. The growth rate eventually vanishes (asymptotically) as the magnetic drift changes sign (around $\theta \approx \pm 0.85\pi$), thus locally rendering ion diamagnetic drift waves ($\omega_R \sim \omega \nabla_{n_i} < 0$ under conventional radially peaked profiles) stable against magnetic drift resonances.

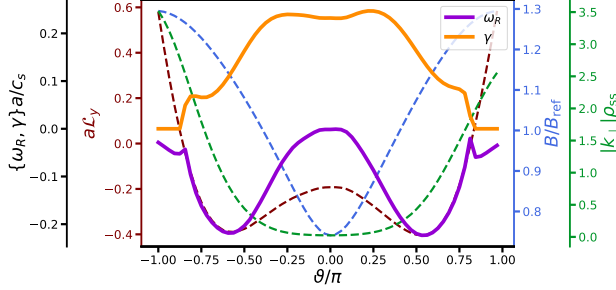


FIG. 1: Variation along the magnetic field line of the normalised local eigenfrequency $\omega_{\text{loc}}(l)$ solution to Eqn. (9) in the adiabatic-electron limit, for a toroidal ITG instability characterised by radial and bi-normal wavenumbers $k_x \rho_{ss} = 0, k_y \rho_{ss} = 0.3$ driven by density and temperature gradients of $a/L_{ni} = 2$ and $a/L_{Ti} = 4$, respectively, in the flux tube of the DIII-D tokamak considered in this work (see Section III). The plasma consists of only a single ion species with $Z_i = 1$ and $T_i = T_e$. Contrasted against the eigenfrequency (solid lines; split into growth rate and propagation frequency) are the variation of the magnetic geometry (dashed lines) focussing on the magnetic field strength in blue, the magnitude of the (normalised) perpendicular wavevector in green and the bi-normal component of the ∇B drift operator (see Section III A) in maroon. For reference, the corresponding eigenfrequency obtained by GENE is $\omega a/c_s = -0.048 + 0.1820i$, being within the extremes of the local solutions.

Clearly, such a collection of local solutions to the eigenfrequency are incompatible with the fundamental notion of

an eigenmode, whose characteristics should be a global system property set by the overall magnetic configuration. This discrepancy between local and global solutions is a consequence of the frequency ordering Eqn. (6), which results in the streaming term of the gyrokinetic Vlasov equation [Eqn. (3)] being neglected for ions, resulting in purely local solutions for the non-adiabatic part of the perturbed ion distribution function Eqn. (7). Without the effect of particle streaming, the adiabatic electron dispersion relation $D_{\text{loc}}^{\text{ae}} = h(\omega, \{\text{geo}\}, \{\text{plasma}\}, l) \hat{\phi}(l)$ formally has an eigenfunction basis consisting of Dirac delta functions ($\hat{\phi} \sim \delta(l - l_0)$)⁶⁸, which violate the underlying assumption that the eigenmodes are characterised by a long-scale variation along the field lines. The streaming term provides the necessary regularising effect on the admissible eigenfunctions, as it introduces non-local (along the field line) physics to the dispersion relation. When kinetic electrons are reintroduced, such regularisation is naturally provided by the bounce-average operator, resulting in an integral problem necessitating self-consistent solutions for $\hat{\phi}(l)$ as well-behaved smooth functions. In the adiabatic-electron limit, however, non-local effects can be re-introduced by not completely neglecting the influence of particle streaming, but considering an asymptotic expansion in $\omega_{ti}/\omega \ll 1$ for the ion gyrocenter distribution (to which Eqn. (7) would be the leading zeroth-order term), resulting to lowest order in an $\mathcal{O}((\omega_{ti}/\omega)^2)$ correction to the dispersion relation which introduces differential operators acting on $\hat{\phi}(l)$, providing the necessary regularising non-local effects^{33,69}. As this ion sound term is formally only $\mathcal{O}((\omega_{ti}/\omega)^2)$, its effects are negligible compared with the regularising influence introduced by the bounce-averaged trapped electrons when kinetic electrons are retained⁶⁸.

Here we propose an alternative approach to reintroduce non-local effects to the electrostatic dispersion relation, which equally applies to the adiabatic and kinetic treatments of the electrons. We construct a global (along the field line) dispersion relation by multiplying by $\hat{\phi}/B(l)$ and integrating along the entire field line, which facilitates a variational principle as is shown below, yielding

$$D_{\text{glob}}(\omega, k_\psi, k_\alpha, \{\text{geo}\}, \{\text{plasma}\}) = \int dl \frac{D_{\text{loc}}(\omega, \mathbf{k}_\perp, \{\text{geo}\}, \{\text{plasma}\}, l) \hat{\phi}}{B} = \left(1 + \sum_j \frac{Z_j^2 n_j}{n_e} \frac{T_e}{T_j}\right) \int dl \frac{\hat{\phi}^2}{B} - \sum_j \frac{Z_j^2 n_j}{n_e} \frac{T_e}{T_j} \int dl \frac{h_{\text{ion},j}(\omega, \mathbf{k}_\perp, \{\text{geo}\}, \{\text{plasma}\}, l) \hat{\phi}^2}{B} - \int_{1/B_{\text{max}}}^{1/B_{\text{min}}} d\lambda \sum_{\text{wells}(\lambda)} K_{\text{tr-el,well}}(\omega, \mathbf{k}_\perp, \lambda, \{\text{geo}\}, \{\text{plasma}\}) \bar{\hat{\phi}}_{\text{well}}^2 L_{\text{well}}^{\text{eff}} \quad (17)$$

where we have reversed the order of integration over pitch angle and field line for the trapped-electron contribution. The summation takes into account the different disconnected trapping wells for a given pitch angle λ along the field line, which corresponds to the various (non-equivalent) populations of

trapped particles, each with their intrinsic bounce-average

$$\bar{\hat{\phi}}_{\text{well}} = \frac{\int_{l_{a,\text{well}}}^{l_{b,\text{well}}} \frac{dl \hat{\phi}(l)}{\sqrt{1-\lambda B(l)}}}{\int_{l_{a,\text{well}}}^{l_{b,\text{well}}} \frac{dl}{\sqrt{1-\lambda B(l)}}} \equiv \frac{\int_{l_{a,\text{well}}}^{l_{b,\text{well}}} \frac{dl \hat{\phi}(l)}{\sqrt{1-\lambda B(l)}}}{L_{\text{well}}^{\text{eff}}},$$

where $l_{\{a,b\},\text{well}}$ are the successive bounce-points of a magnetic well, now formally defined as each simply connected region along the field line where $B(l) \leq 1/\lambda$ is satisfied, and we have introduced $L_{\text{well}}^{\text{eff}}$ as the effective arc-length of each well, which defines the bounce time as $\tau_b^{\text{well}} = L_{\text{well}}^{\text{eff}}/|\mathbf{v}|$. In writing Eqn. (17), we have introduced the short-hand notations for the resonant integrals (with explicit dependencies suppressed)

$$\begin{aligned} h_{\text{ion},j} &= \Gamma_0(b_j) - \frac{\omega \nabla n_j - \frac{3}{2} \omega \nabla T_j}{\omega} J_j^{(0)} \\ &+ \frac{\omega_{j,\nabla B} - \omega \nabla T_j}{2\omega} J_{j,\perp}^{(2)} + \frac{\omega_{j,\kappa} - \frac{1}{2} \omega \nabla T_j}{\omega} J_{j,\parallel}^{(2)}, \\ K_{\text{tr-el}} &= \frac{1}{2} + \frac{3}{4} \frac{\omega_{\text{de}}^T(\lambda) - \omega \nabla T_e}{\omega} J_{\text{tr-el}}^{(2)} - \frac{\omega \nabla n_e - \frac{3}{2} \omega \nabla T_e}{2\omega} J_{\text{tr-el}}^{(1)}, \end{aligned} \quad (18)$$

which respectively provide the kernels for the normalised fluctuating ion number density and trapped-electron pitch-angle density.

Analogous approaches for considering global geometric effects have been considered ranging from perturbative approaches to include the effect of the TEM precession resonance on the eigenmode frequency^{12,21,72,96–98}, energy budget analyses to determine stability properties^{25,47,48,99} and general instability limits^{100,101}, to obtaining quadratic forms of the dispersion relation which closely resemble a traditional

variational formalism^{12,48,49,102–104} as commonly used in e.g. reduced transport models based on quasilinear mixing-length approaches in tokamaks^{105,106}. Here, however, in light of recent findings from Ref. 107, we deviate from the aforementioned works by multiplying with $\hat{\phi}$ rather than $\hat{\phi}^*$, as is formally required to render the non-Hermitian gyrokinetic system variational, as is proven momentarily. Therefore, our work can be regarded as both a correction and an extension to the work from Refs. 48 and 49, where such approaches for electrostatic drift waves have been generalised to stellarator geometry, though only applied in the high-frequency limit where the drift resonances are expanded, and are obtained by multiplying with $\hat{\phi}^*$ instead. Adopting the notation of the aforementioned works, we consider Eqn. (17) as a functional $D_{\text{glob}}(\omega) \rightarrow S[\omega, \hat{\phi}]$ where we suppress the dependence on other fixed quantities. Within the framework of the trapped-electron model, where admissible self-consistent eigenmodes are characterised by $D_{\text{loc}} = 0$, it follows that $S[\omega_0, \hat{\phi}_0] = 0$ for the same frequency-eigenmode pair $(\omega_0, \hat{\phi}_0)$. If the mode structure were to be perturbed $\hat{\phi} \rightarrow \hat{\phi}_0 + \delta \hat{\phi}$, then the mode frequency will necessarily change according to $\omega \rightarrow \omega_0 + \delta \omega$ so that $S[\omega_0 + \delta \omega, \hat{\phi}_0 + \delta \hat{\phi}] = 0$, and consequently $\Delta S = 0$ to all orders in δ . Let us now consider some arbitrary ω and $\hat{\phi}$, and require the functional S to be stationary under small perturbations such that

$$\begin{aligned} \delta S = 0 = & \left(1 + \sum_j \frac{Z_j^2 n_j T_e}{n_e T_j} \right) \int \frac{dl}{B} 2\hat{\phi} \delta \hat{\phi} - \sum_j \frac{Z_j^2 n_j T_e}{n_e T_j} \int \frac{dl}{B} \left(2h_{\text{ion},j}(\omega, l) \hat{\phi} \delta \hat{\phi} + \frac{\partial h_{\text{ion},j}}{\partial \omega} \delta \omega \hat{\phi}^2 \right) \\ & - \int_{1/B_{\text{max}}}^{1/B_{\text{min}}} d\lambda \sum_{\text{wells}(\lambda)} L_{\text{well}}^{\text{eff}} \left(2K_{\text{tr-el,well}}(\omega, \lambda) \hat{\phi}_{\text{well}} \overline{\delta \hat{\phi}_{\text{well}}} + \frac{\partial K_{\text{tr-el,well}}}{\partial \omega} \delta \omega \hat{\phi}_{\text{well}}^2 \right) \end{aligned} \quad (19)$$

and consequently $\Delta S \sim \mathcal{O}(\delta^2)$. The vanishing of the right hand side of Eqn. (19) requires that the derivatives of the kernels Eqn. (18) exist despite sharp resonances in the velocity integrals. Both $\partial h_{\text{ion},j}/\partial \omega$ and $\partial K_{\text{tr-el,well}}/\partial \omega$ are well defined and finite provided that ω is sufficiently far away from

marginality ($\gamma = 0$), such that $\sigma_\gamma = \text{sgn Im}[\omega]$ remains fixed during the variation $\omega \rightarrow \omega + \delta \omega$, which is slightly stricter than the validity condition for Eqn. (11), which guarantees the existence of the ion- [Eqn. (14)] and electron velocity integrals [Eqn. (15)]. The frequency modification is then obtained from Eqn. (19) and reads

$$\delta \omega = \frac{2 \times \int \frac{dl}{B} \delta \hat{\phi} \left[\left(1 + \sum_j \frac{Z_j^2 n_j T_e}{n_e T_j} (1 - h_{\text{ion},j}) \right) \hat{\phi} - B \int_{1/B_{\text{max}}}^{1/B} d\lambda \frac{\hat{\phi}}{\sqrt{1-\lambda B}} K_{\text{tr-el}} \right]}{\sum_j \frac{Z_j^2 n_j T_e}{n_e T_j} \int \frac{dl}{B} \frac{\partial h_{\text{ion},j}}{\partial \omega} \hat{\phi}^2 + \int_{1/B_{\text{max}}}^{1/B_{\text{min}}} d\lambda \sum_{\text{wells}(\lambda)} L_{\text{well}}^{\text{eff}} \frac{\partial K_{\text{tr-el,well}}}{\partial \omega} \hat{\phi}_{\text{well}}^2} \equiv \frac{2A[\omega, \delta \hat{\phi}, \hat{\phi}]}{C[\omega, \hat{\phi}]} \quad (20)$$

where we have unravelled the sum over the various magnetic

wells back into a field line integral by changing the order

of integration in the numerator and introduced two new functionals for notational convenience. Note that these emergent functionals can be written succinctly in terms of the local dispersion relation [Eqn. (12)] as $C[\omega, \hat{\phi}] = -\int dl (\hat{\phi} \delta D_{\text{loc}}[\omega, \hat{\phi}] / \delta \omega) / B = -\delta D_{\text{glob}}[\omega, \hat{\phi}] / \delta \omega$ and $A[\omega, \delta \hat{\phi}, \hat{\phi}] = \int dl \delta \hat{\phi} D_{\text{loc}}[\omega, \hat{\phi}] / B$, where $\delta f / \delta g$ denotes the functional derivative and we require $C[\omega, \hat{\phi}] \neq 0$. We note that upon replacing the kernel functions [Eqn. (18)] by their non-resonant expansions [Eqns. (D3) and (D7) for $h_{\text{ion},j}$ and $K_{\text{tr-el}}$, respectively] and assuming the absence of impurities, Eqn. (20) almost reduces to the variational form in Ref. 48 where $\delta \omega = 2A[\omega, \delta \hat{\phi}, \hat{\phi}] / C[\omega, |\hat{\phi}|]$ is obtained. In the aforementioned work, however, not only was the dispersion relation multiplied by $\hat{\phi}^*$, but $\hat{\phi}$ and $\hat{\phi}^*$ were not considered as separate variables when constructing δS , as formally required in e.g. analogous variational formulations of quantum mechanics, where the Hermitian nature of the Schrödinger equation facilitates the construction of a Lagrangian density in terms of the wavefunction and its complex conjugate^{108–110}. If one would propagate this rationale to the non-Hermitian gyrokinetic system under consideration here, one would instead have obtained $\delta \omega = (A[\omega, \delta \hat{\phi}^*, \hat{\phi}] + A[\omega, \delta \hat{\phi}, \hat{\phi}^*]) / C[\omega, |\hat{\phi}|]$ for the frequency variation if the functional were constructed by multiplying the (local) dispersion relation [Eqn. (9)] with $\hat{\phi}^*$ instead of $\hat{\phi}$.

We now state our variational principle: it follows that $\delta \omega = 0$ when $A[\omega, \delta \hat{\phi}, \hat{\phi}] = 0$, whilst simultaneously $A[\omega, \delta \hat{\phi}, \hat{\phi}] = 0$ if $(\omega, \hat{\phi}) \rightarrow (\omega_0, \hat{\phi}_0)$ are a proper frequency-eigenmode pair solving the (local) dispersion relation [Eqn. (12)]. Conversely, if $\delta \omega = 0$ for all variations $\delta \hat{\phi}$, then Eqn. (12) must be satisfied by the $(\omega, \hat{\phi})$ pair under consideration. Hence, in a liberal sense, this resembles a conventional variational principle.

This variational formalism of Eqn. (17) is only applicable when the effect of kinetic electrons is included such that Eqn. (12) is a properly regularised integral problem. If, however, we consider Eqn. (17) in the context of the adiabatic-electron model, it follows that a root of D_{glob} provides an frequency-eigenmode pair $(\tilde{\omega}, \tilde{\phi})$ with a suitable eigenmode $\tilde{\phi} \neq \delta(l - l_0)$ and a global eigenmode frequency $\tilde{\omega}$. Whilst this frequency-eigenmode pair does not solve $D_{\text{loc}} = 0$ (and therefore $\tilde{\omega}$ deviates from $\omega_{\text{loc}}(l)$), it provides a measure of the overall instability drive to the mode as a result of FLR damping and the distribution of good- and bad-curvature regions along the field line. In the adiabatic-electron limit, one may therefore instead interpret Eqn. (17) not as being variational, but as an eigenmode-weighted average of D_{loc} along the field line. Electrostatic instabilities within the intermediate-frequency regime considered here, see Eqn. (6), always have eigenmodes of the electrostatic potential localised within regions of bad curvature⁹⁹. Weighting the local dispersion relation by an appropriate $\hat{\phi}$ informed about mode localisation physics (as e.g. obtained from first principles by considering the effect of ion sound dynamics or data-driven proxies) will thus result in a stronger influence of the bad-curvature regions on the global dispersion relation, resulting in global eigenfrequencies with $\text{Im}[\tilde{\omega}] > 0$. Therefore, for now, we shall consider Eqn. (17) as an ad-hoc means to

introduce non-local effects to the dispersion relation in the adiabatic-electron limit, and verify *a posteriori* that the obtained eigenfrequencies from this method are in agreement with linear gyrokinetic simulations.

III. GYROKINETIC SIMULATION SETUP AND DISPERSION RELATION SOLUTION STRATEGY

In order to test the validity of the global dispersion relation Eqn. (17), we perform linear gyrokinetic simulations with the flux-tube version of the GENE code⁵. These simulations allow us to assess the ability of Eqn. (17) to describe (toroidal) ITG and TEM by using the GENE linear eigenfunctions as a guess for $\hat{\phi}$. As these eigenfunctions are exact (to within convergence precision), formally $\delta \hat{\phi} = 0$, and ergo from Eqn. (20), it follows that $\delta \omega = 0$. Consequently, any deviation between the eigenfrequency of GENE simulations and the (roots of) global dispersion relation [Eqn. (17)] should therefore be directly attributable to missing physics in our model. Whilst the variational principle only strictly holds for TEMs, the same approach allows us to verify the ad-hoc applicability of Eqn. (17) to describe adiabatic-electron ITGs. A similar approach for verifying the variational principle has been considered in Ref. 104 for KBMs.

A. Geometric considerations for flux-tubes

In the flux-tube approach¹¹¹, the equilibrium gradients are considered fixed (valid for systems with small $\rho^* = \rho/a$), as the simulation domain is typically limited to a perpendicular extent of a few tens of (ion) gyroradii whilst extending along a magnetic field line for N_{pol} poloidal turns. As a consequence, the geometry (predominantly determined by $\nabla \mathbf{B}$) varies along the field line, as the salient geometric features only change over macroscopic length-scales. In order to capture the anisotropy of the fluctuations with respect to the alignment of the a magnetic field, a (non-Cartesian) coordinate system (x, y, z) is adopted

$$x = L_{\text{ref}} \sqrt{s}, \quad y = L_{\text{ref}} \sqrt{s_0} \alpha / q_0, \quad z = \theta \quad (21)$$

where $s = \Phi / \Phi_{\text{edge}}$ is the normalised (toroidal) magnetic flux function, L_{ref} denotes the macroscopic normalisation length scale (typically taken to be the minor radius), s_0 indicates the radial position position at the centre of the flux tube, $q = d\Phi/d\psi$ and q_0 is a short-hand notation for $q(s_0)$. As a result of Eqn. (21), the magnetic field within the flux tube is characterised by $\mathbf{B} = B_{\text{ref}}(x) \nabla x \times \nabla y$, with B_{ref} a reference magnetic field strength as determined by the MHD equilibrium such that $\psi_{\text{edge}} = B_{\text{ref}} a^2 / 2$, therefore rendering z as the field-aligned coordinate, which is taken to be the poloidal angle. Periodic boundary conditions are enforced across the perpendicular domain, while a twist-and-shift boundary condition^{112,113} is applied along z :

$$\tilde{\phi}_{k_x, k_y}(z, t) = \tilde{\phi}_{k_x + p \Delta k_x, k_y}(z + 2\pi p N_{\text{pol}}, t) \tilde{C}_{k_y}^p \quad (22)$$

where $\tilde{\phi}_{k_x, k_y}$ represents a perpendicular Fourier mode of the electrostatic potential, $p \in \mathbb{Z}$, $\Delta k_x = 2\pi N_{\text{pol}} \delta k_y$ with $\delta = d \ln q / d \ln x|_{x=x_0}$ being the global magnetic shear, and \tilde{C}_{k_y} is a phase factor with $|\tilde{C}_{k_y}| = 1$. Whilst Eqn. (22) explicitly shows the application of the twist-and-shift boundary condition for the electrostatic potential, the same rule is applied to all fluctuations. Although this twist-and-shift boundary condition is formally incorrect in stellarators due to the general lack of periodicity in the magnetic geometry after N_{pol} poloidal turns, reasonably accurate results can be obtained if the parallel extent of the flux tube is large enough such that the modes experience the proper drive and damping mechanisms as set by the real geometry over a turbulent correlation length^{112,113}.

In terms of these flux-tube coordinates, the relevant geometric quantities in the (linear) gyrokinetic Vlasov equation [Eqn. (3)] can all be computed from the elements of the corresponding contravariant metric tensor^{114–116} $g^{nm} = \nabla x^n \cdot \nabla x^m$, where $\{x^1, x^2, x^3\} = \{x, y, z\}$. In particular, the perpendicular wavenumber $\|\mathbf{k}_\perp\|$ can be computed from Eqn. (10) under the substitution $\psi \rightarrow x$ and $\alpha \rightarrow y$, while the parallel derivative follows as $\nabla_\parallel = 1/(\sqrt{g} B_N) \frac{\partial}{\partial z}$, where $B_N = B/B_{\text{ref}}$ represents the normalised magnetic field strength and $\sqrt{g} = ((\nabla x \times \nabla y) \cdot \nabla z)^{-1}$ is the determinant of the metric tensor. Meanwhile the geometric component of the ∇B drift is given by $(\mathbf{e}_b \times \ln B) \cdot \mathbf{k}_\perp = k_x \mathcal{L}_x + k_y \mathcal{L}_y$ in terms of the drift operators

$$\begin{aligned} \mathcal{L}_x &= - \left(\frac{\partial B_N}{\partial y} \Big|_{x,z} + \frac{\gamma^2}{\gamma^1} \frac{\partial B_N}{\partial z} \Big|_{x,y} \right) \\ \mathcal{L}_y &= \frac{\partial B_N}{\partial x} \Big|_{y,z} + \frac{\gamma^3}{\gamma^1} \frac{\partial B_N}{\partial z} \Big|_{x,y} \end{aligned} \quad (23)$$

where $\gamma^1 = g^{xx} g^{yy} - (g^{xy})^2$, $\gamma^2 = g^{yz} g^{xx} - g^{xz} g^{xy}$ and $\gamma^3 = g^{xz} g^{yy} - g^{xy} g^{yz}$. Analogously, the geometric component of the curvature drift can be written as $(\mathbf{e}_b \times \kappa) \cdot \mathbf{k}_\perp = k_x \mathcal{K}_x + k_y \mathcal{K}_y$. Since the curvature vector can be expressed as¹¹⁷

$$\kappa = \nabla_\perp \ln B + 2\beta \nabla \ln p, \quad (24)$$

it follows, due to the (assumed) existence of (isobaric) flux surfaces, that the drift-operators for the curvature drift are $\mathcal{K}_x = \mathcal{L}_x$ and $\mathcal{K}_y = \mathcal{L}_y + (d\beta_{\text{ref}}/dx)/(2B_N)$, where β_{ref} is the normalised total plasma pressure with respect to magnetic pressure of B_{ref} .

B. Description of geometries and simulation parameters

In order to assess the capabilities of the global dispersion model Eqn. (17) to describe ITG and TEM instabilities in arbitrary toroidal geometry, we compare against gyrokinetic simulations in a variety of realistic configurations of existing devices. The flux-tube geometry information is generated by the Geometry Interface for Tokamaks and Stellarators (GIST) code¹¹⁵ from the magnetic equilibrium of each configuration. For each device we perform GENE simulations using a single flux-tube, which is sufficient to capture all salient geometric features on a tokamak flux surface. For the stellarator

configurations, we choose the so-called *bean flux tube* – corresponding to the flux tube where the bean-shaped poloidal cross-section is intersected at the out-board midplane – which for both HSX⁷³ and W7-X^{118,119} tends to be the most unstable flux tube. The global (i.e. MHD) geometric parameters determining the flux-tube domain for each of the considered magnetic configurations are shown in Table I. Note that all flux tubes are centred at a normalised radius of $s_0 = 0.5$, chosen to be sufficiently far radially outward to have both appreciable gradients as well as an appreciable trapped-electron fraction, with the exception of the TCV flux tubes. These are placed more radially outward at $s_0 = 0.774$ where the effects of triangular shaping of the last closed-flux surface are more discernable^{120,121}, resulting in flux tubes characterised by local triangularities of $\delta(s_0) \approx \pm 0.2$. For consistency with the electrostatic approximation, all flux tubes correspond to vacuum configurations of their respective devices.

As discussed in Section III A, a flux tube spanning a single poloidal turn contains all essential geometry information for a tokamak, however, for stellarators, N_{pol} has to be chosen carefully such that the modes experience a sufficient amount of the physical driving and damping forces set by the real geometry, as opposed to the artificial geometry generated by the twist-and-shift boundary condition (see Section III C on this matter). In previous studies, flux tubes spanning $N_{\text{pol}} = 1$ and $N_{\text{pol}} = 4$ poloidal turns have been found to be sufficiently long for W7-X^{112,118} and HSX¹¹³, respectively, as are also considered for the flux tubes used in this work.

For both ITG and TEM we perform linear initial-value GENE simulations for a various scenarios. First, to focus on the relevant ITG physics, we perform adiabatic-electron simulations at fixed density gradient $a/L_n = 2$ while varying the temperature gradient $a/L_{T_i} = [3, 4, 5, 6]$, where $1/L_{T_s} = -d \ln T_s / dx$ is the inverse temperature gradient scale length of species s (with an analogous definition for $1/L_{ns}$), defined such that $L_{T_s}, L_{ns} > 0$ for centrally peaked profiles. At low concentrations, the presence of impurities in the plasma results in dilution effects that weaken the ITG instability, see Ref. 122 and references therein. These dilution effects are due to ambipolarity (i.e. quasi-neutrality for the equilibrium density profiles), which, assuming the electron density profile to be fixed to focus on impact of impurities, limits the main ion density and its gradient to

$$\begin{aligned} \frac{n_i}{n_e} &= 1 - \sum_{\text{imp}} \frac{Z_{\text{imp}}}{Z_i} \frac{n_{\text{imp}}}{n_e} \\ \frac{L_{ne}}{L_{ni}} &= \frac{1 - \sum_{\text{imp}} Z_{\text{imp}} \frac{n_{\text{imp}}}{n_e} \frac{L_{ne}}{L_{n\text{imp}}}}{1 - \sum_{\text{imp}} Z_{\text{imp}} \frac{n_{\text{imp}}}{n_e}} \end{aligned} \quad (25)$$

where we have explicitly split the sum over ion quantities into the main species and impurities. From Eqn. (25) it is evident that the ion concentration decreases as the impurity concentration increases, leading to a decrease in resonant population for ITGs. The presence of impurities can also modify the ITG drive by either enhancing or reducing the ion density gradient with respect to the (nominal) electron density gradient, depending on the shape of the impurity density profile

TABLE I: Global geometric parameters that determine the flux-tube coordinate system Eqn. (21) for the various geometries.

	DIII-D	TCV δ^+	TCV δ^-	HSX	W7-X (hm)	W7-X (nm)
s_0	0.5	0.774	0.774	0.5	0.5	0.5
q_0	2.566	1.052	1.052	0.941	1.102	1.135
\hat{s}	1.579	0.705	0.705	-0.046	-0.129	-0.141
N_{pol}	1	1	1	4	1	1

(with respect to the electron density profile). This trend in enhancement/reduction of linear drive depending on the shape of the impurity density profile has also recently been reported to carry over to turbulent heat fluxes in nonlinear simulations¹²³. Lastly, when the impurity concentration becomes significantly large, an impurity-driven ITG may emerge as the dominant instability. For all simulations in this paper, we consider fully ionised carbon C^{6+} as the only impurity species, such that the effective charge $Z_{\text{eff}} = \sum_j Z_j^2 n_j / n_e$ together with the impurity (and electron) density gradient(s) fully determines the ion quantities through Eqn. (25). We perform two sets of simulations at fixed nominal gradients of $a/L_{ne} = 2$, $a/L_{Ti} = a/L_{TC} = 4$, one scanning over $Z_{\text{eff}} = [1.2, 1.4, \dots, 2]$ while considering $a/L_{nC} = 2$ (such that Eqn. (25) implies $a/L_{ni} = 2$ as well) to isolate the density dilution effect, and one scanning over $a/L_{nC} = [-4, -2, \dots, 6]$ at fixed value of $Z_{\text{eff}} = 1.4$ to isolate the effect of density gradient dilution. In present-day experiments, values of $Z_{\text{eff}} \approx 1.4$ – 1.6 are commonly observed in devices with a carbon wall^{124–127}, though higher values of $Z_{\text{eff}} > 2$ are achievable through deliberate impurity seeding, as will be the case for future reactor-scale devices^{128,129}. Additionally, realistic impurity density profiles typically tend to be flat ($a/L_{nC} = 0$)¹²⁵, though hollow impurity profiles with an off-axis peak have also been observed in both tokamaks^{126,130} and the Large Helical Device stellarator¹³¹.

Secondly, in simulations including kinetic electrons we obtain TEMs by considering artificial profiles with finite density and (optionally) electron temperature gradient, but a vanishing ion temperature gradient $\nabla T_i = 0$ to eliminate the possibility of ITGs. This generates two datasets, one for density-gradient-driven TEMs (where in addition we assume $\nabla T_e = 0$) scanning over $a/L_n = [1, 2, 3, 4]$, and one where we scan over $a/L_{Te} = [1, 2, \dots, 6]$ at fixed $a/L_n = 3$ to probe the predictive capabilities of the global dispersion model with respect to electron-temperature-gradient-driven TEMs. Furthermore, the inclusion of kinetic electrons also has an effect on the ITG instability, hence we consider a third set where we scan over $a/L_{Ti} = [1, 2, \dots, 6]$ in presence of a fixed density gradient $a/L_n = 3$, while assuming a vanishing electron temperature gradient to limit the drive of TEMs in favour of ITGs as the ion temperature gradient is increased. Lastly, a fourth kinetic-electron dataset is considered based on realistic profiles where both ion and electron temperature gradient are finite and are separately modified to $a/L_{Ts} \rightarrow \{1, 5\}$ with respect to a nominal scenario of $a/L_n = 3$, $a/L_{Ti} = 3$, $a/L_{Te} = 3$. For all simulations with kinetic electrons, impurities are excluded.

For all simulations, we consider a deuterium plasma, with a mass ratio of $m_i/m_e = 3670$ when electrons are treated kinetically, and assume $T_i = T_e$, corresponding to reactor-relevant

fusion conditions. Whenever impurities are considered, we assume thermal equilibrium between ion species, $T_i = T_e$, due to the fast collisional relaxation timescale between species with similar mass¹²⁵, which implies likewise that $L_{Ti} = L_{Te}$, as has been considered in all simulations including impurities. Similar assumptions regarding the impurity temperature have been applied by e.g. Refs.^{62,123}. For each scenario, we scan over the bi-normal wavenumber $k_y \rho_{ss} = [0.1, 0.2, \dots, 2]$ and the driving gradient (or Z_{eff} in case of impurities). The ballooning space of modes has been centred at $k_x = 0$, which typically corresponds to the most unstable mode in axisymmetric configurations¹³² as well as the bean flux tube in stellarators^{73,118,119}. For each scenario, we have performed convergence tests in the number of grid points used to discretise the velocity-space variables v_{\parallel} and μ as well as the total extent of ballooning space as set by $2\pi N_{\text{pol}} n_{kx}$ at both extremities of the driving gradient to ensure that the eigenfrequencies are converged within $\leq 5\%$. The resulting resolutions for each configuration and scenario are shown in Table II.

C. Solving the global dispersion relation

In order to facilitate a direct comparison between the eigenfrequencies obtained by the global dispersion relation model and the linear gyrokinetic simulations we consider a similar normalisation scheme as used in GENE. This entails that equilibrium (gradient) length scales are normalised to L_{ref} , whilst the perpendicular fluctuation length scales are normalised to a reference gyroradius $\rho_{\text{ref}} = c_{\text{ref}}/\Omega_{\text{ref}}$, where $c_{\text{ref}} = \sqrt{T_{\text{ref}}/m_{\text{ref}}}$ and $\Omega_{\text{ref}} = eB_{\text{ref}}/m_{\text{ref}}$. Here we choose $m_{\text{ref}} = m_i$ and $T_{\text{ref}} = T_e$ such that ρ_{ref} is the ion gyroradius at sound speed ρ_{ss} (note the distinction from ρ_s – as commonly used in literature to denote the sound ion Larmor radius^{22,31,57,119} – defined in Section II). Subsequently, all temperatures are normalised by T_{ref} , masses by m_{ref} , and densities by n_{ref} , the latter taken to be the electron density. Consequently, time scales are subsequently normalised by $L_{\text{ref}}/c_{\text{ref}}$, while the electrostatic potential is normalised to e/T_{ref} . By choosing L_{ref} to coincide with minor radius a , compatibility with the GIST code providing normalised flux-tube geometry information is ensured. In terms of these normalisations and the flux-tube coordinates from Eqn. (21), the expressions for the various quantities appearing in Eqns. (17) and (18) are summarised in Table III.

One key concern for the global dispersion relation model is the geometry representation. Since we obtain the electrostatic potential from GENE simulations using the twist-and-shift boundary condition, see Eqn. (22), we consider the extended ballooning representation of the eigenmode beyond

TABLE II: Numerical resolutions for the GENE simulations for various geometries and drive-scenarios. The numbers in the table correspond to the tuple $(n_{kx}, n_z, n_v, n_\mu)$ representing the number of radial Fourier modes included in the extended eigenmode envelope, and the number of grid points used for the field-line following coordinate, the parallel velocity space and the magnetic moment. Below “ae” denotes an adiabatic electron simulation, “ke” refers to a simulation with kinetic electrons, whilst “full gradient” indicates that the effect of finite ion and electron temperature gradient drive are both included.

	DIII-D	TCV δ^+	TCV δ^-	HSX	W7-X (hm)	W7-X (nm)
ae ITG	(11,64,24,8)	(21,64,32,12)	(21,64,24,8)	(21,512,24,8)	(43,96,32,12)	(43,128,32,12)
ae ITG + impurity	(11,64,24,8)	(21,64,48,16)	(21,64,36,18)	(21,512,24,8)	(43,96,32,12)	(43,128,32,12)
∇n -TEM	(21,64,48,12)	(33,64,64,12)	(33,64,64,16)	(31,512,48,18)	(43,96,64,24)	(33,128,64,24)
ke ITG	(21,64,64,18)	(33,64,48,12)	(33,64,64,16)	(21,512,48,18)	(43,96,64,24)	(43,128,48,18)
∇T_e -TEM	(21,64,36,8)	(33,64,36,8)	(33,64,48,12)	(41,512,48,18)	(43,96,48,18)	(43,128,48,18)
Full gradient	(21,64,64,18)	(33,64,48,12)	(33,64,48,12)	(31,512,48,18)	(43,96,64,24)	(43,128,48,18)

TABLE III: Overview of normalised terms appearing in the global dispersion relation. Whenever applicable, the terms are expressed in quantities related to the flux-tube coordinates Eqn. (21), and in terms of various geometric quantities defined in Section III A.

dl	$L_{\text{ref}} \sqrt{g} B dz / B_{\text{ref}}$
B	$B_{\text{ref}} \sqrt{g^{xx} g^{yy} - (g^{xy})^2}$
b_j	$[(k_x \rho_{\text{ref}})^2 g^{xx} + (k_y \rho_{\text{ref}})^2 g^{yy} + 2k_x k_y \rho_{\text{ref}}^2 g^{xy}] m_j T_j B_{\text{ref}}^2 / (Z_j^2 B^2 T_{\text{ref}} m_{\text{ref}})$
$\omega_{\nabla n_j}$	$- [k_y \rho_{\text{ref}} T_j L_{\text{ref}} / (Z_j T_{\text{ref}} L_{n_j})] c_{\text{ref}} / L_{\text{ref}}$
$\omega_{\nabla T_j}$	$- [k_y \rho_{\text{ref}} T_j L_{\text{ref}} / (Z_j T_{\text{ref}} L_{T_j})] c_{\text{ref}} / L_{\text{ref}}$
$\omega_{j, \nabla B}$	$[T_j B_{\text{ref}} (k_x \rho_{\text{ref}} \mathcal{L}_x L_{\text{ref}} + k_y \rho_{\text{ref}} \mathcal{L}_y L_{\text{ref}}) / (Z_j T_{\text{ref}} B)] c_{\text{ref}} / L_{\text{ref}}$
$\omega_{j, \kappa}$	$[T_j B_{\text{ref}} (k_x \rho_{\text{ref}} \mathcal{K}_x L_{\text{ref}} + k_y \rho_{\text{ref}} \mathcal{K}_y L_{\text{ref}}) / (Z_j T_{\text{ref}} B)] c_{\text{ref}} / L_{\text{ref}}$

the original $2\pi N_{\text{pol}}$ extent of the flux tube where geometric quantities are defined, allowing us to consider only the effect of a $k_x = 0$ mode with a vanishing amplitude $|\hat{\phi}(\theta)| \rightarrow 0$ as $|\theta| \rightarrow \infty$, which is a required boundary condition on the fluctuations in the ballooning formalism⁶⁸. As this formalism was used to obtain the gyrokinetic Vlasov equation [Eqn. (3)] from which we derived our dispersion relation, it should be respected, while the eigenmode amplitude is typically not vanishing at the flux-tube boundaries of $|\theta| = \pi N_{\text{pol}}$ unless N_{pol} is large, hence necessitating a description of the geometry beyond its original domain. The geometry-related terms appearing in Table III are therefore expanded in ballooning space (see Supplemental Material) as

$$\begin{aligned}
\sqrt{g}(\theta + 2\pi p N_{\text{pol}}) &= \sqrt{g}(\theta) \\
g^{xx}(\theta + 2\pi p N_{\text{pol}}) &= g^{xx}(\theta) \\
g^{xy}(\theta + 2\pi p N_{\text{pol}}) &= g^{xy}(\theta) + 2\pi p N_{\text{pol}} \hat{\delta} g^{xx}(\theta) \\
g^{yy}(\theta + 2\pi p N_{\text{pol}}) &= g^{yy}(\theta) + 4\pi p N_{\text{pol}} \hat{\delta} g^{xy}(\theta) \\
&\quad + (2\pi p N_{\text{pol}} \hat{\delta})^2 g^{xx}(\theta) \\
B(\theta + 2\pi p N_{\text{pol}}) &= B(\theta) \\
\mathcal{L}_x(\theta + 2\pi p N_{\text{pol}}) &= \mathcal{L}_x(\theta) \\
\mathcal{K}_x(\theta + 2\pi p N_{\text{pol}}) &= \mathcal{K}_x(\theta) \\
\mathcal{L}_y(\theta + 2\pi p N_{\text{pol}}) &= \mathcal{L}_y(\theta) + 2\pi p N_{\text{pol}} \hat{\delta} \mathcal{L}_x(\theta) \\
\mathcal{K}_y(\theta + 2\pi p N_{\text{pol}}) &= \mathcal{K}_y(\theta) + 2\pi p N_{\text{pol}} \hat{\delta} \mathcal{L}_x(\theta). \quad (26)
\end{aligned}$$

where $p \in \mathbb{Z}$ defines the extended ballooning angle as $\theta_p = \theta + 2\pi p N_{\text{pol}}$ as related to the parallel boundary condition

[Eqn. (22)]. It should be noted that Eqn. (26) is formally incorrect for stellarators, as the toroidal variation of the geometry has been neglected, resulting in discontinuities in e.g. the drift-operators and $\|\mathbf{k}_\perp\|$ proportional to the global shear, though the consequences of this discrepancy on the linear eigenmode properties are fairly benign¹¹². A last geometric consideration is the calculation of the bounce-averages, since the involved bounce-integrals are formally divergent as one approaches the bounce-points. As we consider realistic 3D geometries, we cannot make use of analytical expressions for trapped-particle precession as exist for tokamaks^{90,133}. Rather we use the specialised trapezoidal method developed by Ref. 134 for these bounce-integrals with a $1/\sqrt{f(x)}$ singularity.

In order to evaluate $D_{\text{glob}}(\omega|k_x, k_y, \{\text{geo}\}, \{\text{plasma}\})$, the ion integrals in Eqn. (14) are evaluated numerically, whilst the analytical expressions for Eqn. (15) are used, except in magnetic wells where the bounce-averaged drift is close to vanishing. In the latter case, the argument of the plasma dispersion function diverges, which makes the analytical expressions ill-defined. Hence, whenever $|\omega/\omega_{de}^T| > 250$ we use a cubic asymptotic expansion [see Eqn. (D6)] for $J_{\text{tr-el}}^{(1)}, J_{\text{tr-el}}^{(2)}$ instead. Finally, in order to obtain the roots of Eqn. (17), we make use of a quasi-Newton method employing a combination of the so-called “good” Broyden algorithm^{135,136} with line search¹³⁷ to allow for adaptive step-sizing. In order to guarantee convergence of this method, both a good initial guess for both the mode frequency and the Jacobian are necessary^{138–140}. The initial guess for the eigenfrequency is

obtained by considering a high-frequency expansion of the ion- and electron resonant integrals of Eqns. (14) and (15) to approximate their respective density kernels [Eqn. (18)]. Such a high-frequency expansion can be made physically valid in

the limit of strong drive, which, as shown in Section D, yields to first order in $\omega_{ds}/\omega \ll 1$ a quadratic dispersion relation in the mode frequency

$$D_{\text{glob}}(\omega, k_x, k_y, \{\text{geo}\}, \{\text{plasma}\}) \approx \left(1 + \sum_j \frac{Z_j^2 n_j T_e}{n_e T_j} \right) \int dl \frac{\hat{\phi}^2}{B} - \sum_j \frac{Z_j^2 n_j T_e}{n_e T_j} \int dl \frac{\hat{\phi}^2}{B} \left(\Gamma_0(b_j) \left[1 - \frac{\omega_{\nabla n_j}}{\omega} + \frac{\omega_{j,\kappa} + \omega_{j,\nabla B}}{\omega} \right. \right. \\ \left. \left. - \frac{(\omega_{\nabla n_j} + \omega_{\nabla T_j})(\omega_{j,\nabla B} + \omega_{j,\kappa})}{\omega^2} + b_j \frac{\omega_{\nabla T_j} \omega_{j,\nabla B}}{\omega^2} \right] + b_j (\Gamma_1(b_j) - \Gamma_0(b_j)) \times \right. \\ \left. \left[\frac{\omega_{j,\nabla B}}{\omega} - \frac{\omega_{\nabla T_j}}{\omega} - \frac{\omega_{j,\nabla B}(\omega_{\nabla n_j} + \omega_{\nabla T_j})}{\omega^2} - \frac{\omega_{\nabla T_j}(\omega_{j,\kappa} + \omega_{j,\nabla B})}{\omega^2} + 2b_j \frac{\omega_{\nabla T_j} \omega_{j,\nabla B}}{\omega^2} \right] \right) \\ - \int_{1/B_{\text{max}}}^{1/B_{\text{min}}} d\lambda \sum_{\text{wells}(\lambda)} \left[\frac{1}{2} \left(1 - \frac{\omega_{\nabla n_e}}{\omega} \right) + \frac{3}{4} \frac{\overline{\omega_{de,\text{well}}^T}}{\omega} \left(1 - \frac{\omega_{\nabla n_e} + \omega_{\nabla T_e}}{\omega} \right) \right] \hat{\phi}_{\text{well}}^2 L_{\text{well}}^{\text{eff}}, \quad (27)$$

where we have reflected the change to the flux-tube coordinate system discussed in Section III A by denoting the radial and bi-normal wavenumbers as $k_\psi \rightarrow k_x$ and $k_\alpha \rightarrow k_y$, respectively. In the limit of a single ion species, Eqn. (27) reduces to the dispersion relation found in e.g. Refs. 48 and 49, where the high-frequency expansion was directly applied to the resonant denominators, i.e. $1/(\omega - \omega_{ds}) \approx (1 + \omega_{ds}/\omega)/\omega$. Additionally, within the adiabatic-electron approximation, upon taking the DK limit $b_j \approx 0$ and assuming the ions to be far from marginality ($\omega_{\nabla T_j}/\omega_{\nabla n_j} \gg 1$), the local equivalent of Eqn. (27) (i.e. neglecting the role of the $\int dl \hat{\phi}^2/B$ operator) further reduces to the dispersion relation model used to describe the role of impurities on the ITG instability developed in Ref. 45. Precomputing the geometry-dependent field-line and pitch-angle integrals in Eqn. (27) allows for an analytical solution for the approximate eigenfrequency ω , which maintains the essential physics of instability drive by (unfavourable) magnetic drifts being balanced by FLR damping, as well as frequency scalings proportional to the driving gradients. The approximate eigenfrequency obtained from the quadratic dispersion relation [Eqn. (27)] corresponding to an unstable mode is used as an initial guess for root-finding. Meanwhile the initial guess for the Jacobian is obtained using second-order finite differences. It has been verified that using a regular Newton method yields similar results at increased computational cost due to the need to re-estimate derivatives at every iteration. In cases where root finding algorithm does not reach convergence, a conventional grid-search approach is used instead to solve the dispersion relation.

IV. DISPERSION MODEL VERSUS LINEAR GYROKINETIC SIMULATIONS

In this section we present the main findings of the work comparing the (complex) eigenmode frequency obtained by

the global dispersion model developed in Section II to the eigenfrequency obtained from GENE simulations. For all results presented in this section, the GENE eigenfunction of the electrostatic potential is used as input to the model to test its variational nature according to Eqn. (20). The variational aspect of the model (with regard to the eigenfunction) is further assessed in Section V where rudimentary trial functions are used instead. In all cases, a radial wavenumber of $k_x = 0$ is considered, consistent with centering of ballooning space of eigenmodes at $k_x = 0$ in the simulations. Here we will focus on (a subset of) results for the DIII-D tokamak, HSX stellarator and high-mirror configuration of the W7-X stellarator only, with the results for the remainder of geometries and scenarios listed in Table II available in the Supplementary Material, which further extend our validation to include geometric sensitivity effects due to differences in triangularity (for TCX cases) and degree of maximum- J -ness (for W7-X cases), as well as additional scalings with respect to instability drive parameters.

The focus on these configurations allows us to cover both realistic axisymmetric geometry with (moderate) shaping beyond circular cross-sections as relevant for exploitation of higher fusion yields in ITER and beyond¹²⁹, as well as different classes of stellarators (quasi-helically symmetric and approximately quasi-isodynamic for HSX and W7-X, respectively), hence offering a wide range of salient geometric features that affect microinstability. Here, quasi-isodynamicity refers to configurations where the contours of $\|\mathbf{B}\|$ are poloidally closed, and the second adiabatic invariant J is constant on a flux surface, a key requirement for achieving a maximum- J configuration^{29,141}. The most relevant geometric quantities in the HSX and the high-mirror configuration W7-X flux tubes used in this work are shown in Figure 2, while those in the DIII-D flux tube geometry are displayed in Figure 1. Comparing geometries, we find qualitative similarity between the arrangement of magnetic wells and re-

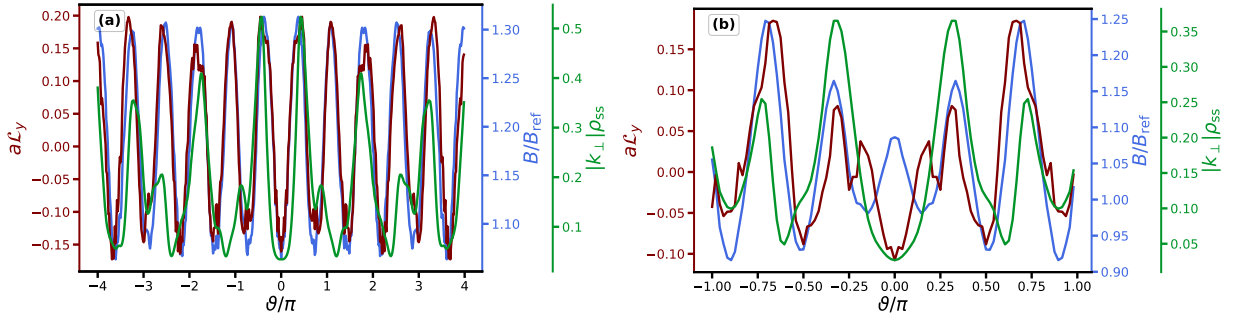


FIG. 2: Flux-tube geometries for (a) the HSX stellarator and (b) high-mirror configuration of the W7-X stellarator showing the variation of the magnetic field strength (blue), bi-normal component of the ∇B drift (maroon) and magnitude of the perpendicular wavenumber (green) along the field line. In the latter we have taken $k_x \rho_{ss} = 0$, $k_y \rho_{ss} = 0.3$, such that a direct comparison to $\|\mathbf{k}_\perp\| \rho_s$ in the DIII-D geometry from Figure 1 is facilitated. Note that the W7-X flux-tube spans only a single poloidal turn, whereas the HSX flux-tube contains the geometric data of four poloidal turns.

gions of unfavourable magnetic curvature (characterised by $\mathcal{L}_y < 0$) between DIII-D and HSX, exemplifying axisymmetry and quasi-helical symmetry, respectively¹⁴², whilst such alignments are minimised in W7-X, corresponding to the key feature of a maximum- J configuration¹⁴². While this feature is only partially achieved by the vacuum field considered in this work, the degree of maximum- J -ness generally increases at higher β ^{32,143,144}. The most striking difference between the stellarator configurations and DIII-D is the magnitude of the perpendicular wavenumber, defined as in Eqn. (10) under substitutions $\{\psi, \alpha\} \rightarrow \{x, y\}$ to match flux-tube coordinates used by GENE, which is an order of magnitude larger in the latter case at the same bi-normal wavenumber. This can be attributed to the significantly lower global shear \hat{s} for both stellarator configurations, resulting in a much weaker effect of the secular term in the g^{yy} component of the magnetic tensor.

We note that in our analytical theory, we prescribed a time dependence of $\exp(-i\omega t)$, which results in a sign discrepancy for the propagation frequency ω_R between the analytical theory from Section II and high-fidelity GENE simulations. In what follows, we shall always adopt the GENE convention, where $\omega_R > 0$ corresponds to propagation in the ion diamagnetic direction, thereby inverting the sign of $\text{Re}[\omega]$ obtained by the global dispersion model.

A. Adiabatic-electron density-dilution scenario

Here we present the scenario probing for the density dilution effect for the adiabatic-electron simulations including C^{6+} as an impurity while varying Z_{eff} , therefore simultaneously verifying the multi-species capabilities of the model and testing the validity of the ad-hoc method of introducing non-local effects along the field line by operating on the local dispersion relation [Eqn. (9)] with $\int dl \hat{\phi}/B$ in the absence of a regularising trapped-electron term. Results for the driving gradient scans in a/L_{Ti} (no impurity) and a/L_{nC} can be found in the Supplementary Material and show similar degrees of agreement.

The results obtained for the Z_{eff} scan obtained with the

global dispersion model are contrasted with GENE eigenfrequencies, and are shown in Figure 3. A general trend observable across all geometries is that both the growth rate and the propagation frequency monotonically decrease as Z_{eff} increases, consistent with the dilution of the main-ion density. The global dispersion model universally predicts larger growth rates, which can be attributed to the lack of finite-transit effects which provide Landau damping. Since, at a given bi-normal wavenumber k_y , this overestimation is roughly constant, it suggests that Landau damping could be heuristically included as $\gamma \rightarrow \gamma - \nu_{Ti}/(\sqrt{2}L_\parallel)$ where L_\parallel is the connection length³³. The larger discrepancies in the growth rate observed in W7-X can therefore be attributed to the shorter connection length ($L_\parallel/(\pi q R) \approx 0.12$, taking $R = 5.5\text{m}$ for W7-X) compared with typical tokamaks, where one commonly estimates $L_\parallel \approx \pi q R$ ^{7,33}. The propagation frequency varies monotonically in DIII-D, whilst several mode transitions (indicated by non-monotonous behaviour in ω_R) occur in GENE simulations for both stellarator geometries, where multiple unstable eigenmodes co-exist partly due to the presence of multiple non-equivalent magnetic and drift wells. These mode transitions are reproduced by the global dispersion model, though with greater accuracy in the propagation frequency in HSX compared with W7-X. The corresponding eigenmodes range from being broad in ballooning space at the lowest wavenumbers to strongly ballooned around the out-board midplane ($\theta = 0$) for $k_y \rho_{ss} \gtrsim 1$. These extended eigenmodes are a typical feature of low-shear stellarators, where FLR suppression is weaker due to the limited role of the secularity in g^{yy} , keeping $\|\mathbf{k}_\perp\|$ small. These findings illustrate the utility of adopting an extension of the flux-tube geometry beyond its original $2\pi N_{\text{pol}}$ domain using Eqn. (26) to describe the drive of these broad eigenmodes by magnetic drift resonances. Additionally, the results from the Z_{eff} scan in Figure 3 and the a/L_{nC} scan in the Supplementary Material show that the global dispersion solver is capable of predicting how the presence of impurities directly affects the absolute ITG growth rates, which can be considered as an extension of the recent perturbative impurity model from Ref. 45 which predicts the relative modification to the ITG growth rates due to

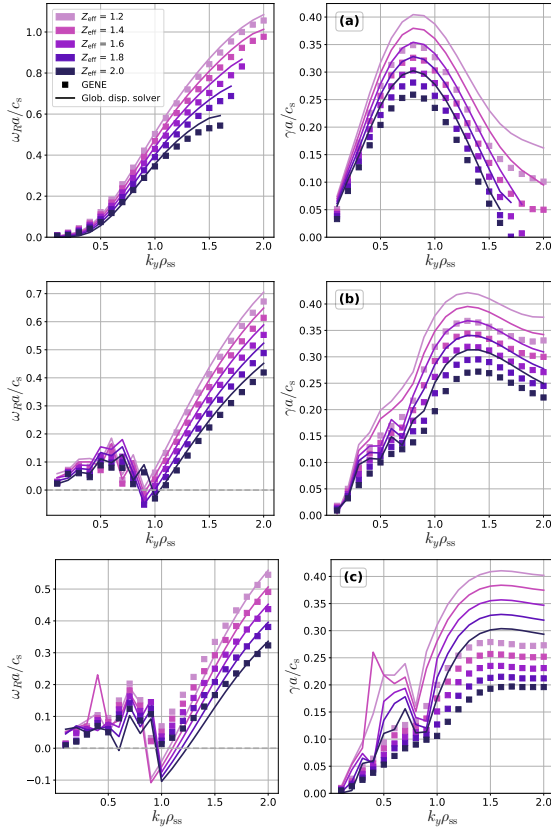


FIG. 3: Eigenfrequency solutions of the global dispersion relation model (solid lines) contrasted with GENE simulations (symbols) for adiabatic-electron ITG in the presence of C^{6+} impurities, while varying the impurity concentration by modifying Z_{eff} (darker colours indicate larger impurity concentration). Shown are results for (a) the DIII-D tokamak, (b) the HSX stellarator and (c) the high-mirror configuration of the W7-X stellarator. In all cases, a density- and temperature gradient of $a/L_{n_s} = 2$ and $a/L_{T_s} = 4$, respectively, are considered for both deuterium ions and the carbon impurity.

impurities.

B. Kinetic-electron scenarios

Here we present the result for both the a/L_{Te} and a/L_{Ti} gradient scans including kinetic electrons, while results for the a/L_n scan (no temperature gradients) and non-synthetic profiles with non-zero gradients for both species are shown in the Supplementary Material. As the variational nature of the model is retained when kinetic electrons are included, these scenarios allow us to verify the variational property of Eqn. (17), in both electron-dominated and ion-dominated scenarios.

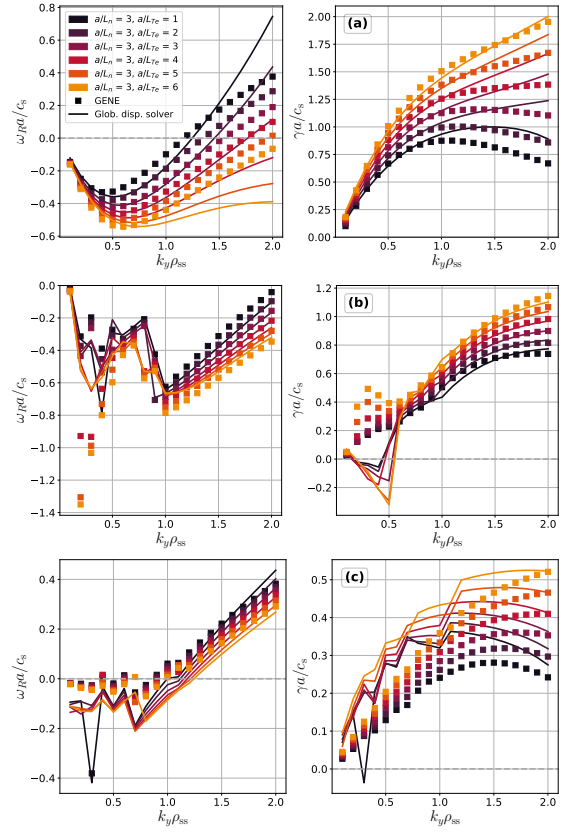


FIG. 4: Eigenfrequency solutions of the global dispersion relation model (solid lines) contrasted with GENE simulations (symbols) including kinetic electrons while varying the electron temperature gradient a/L_{Te} (lighter colours indicate a stronger temperature gradient). Shown are results for (a) the DIII-D tokamak, (b) the HSX stellarator and (c) the high-mirror configuration of the W7-X stellarator. In all cases, the density gradient is fixed at $a/L_n = 3$ whilst the ion temperature gradient is suppressed ($a/L_{Ti} = 0$).

Application to pure TEM case

First, we focus on the physics associated with the precession resonance by testing the model against GENE simulations without an ion temperature gradient. Here, only TEMs are expected to emerge, and results for the a/L_{Te} scan are shown in Figure 4. The results for the density gradient scan of density-gradient-driven TEMs in absence of both temperature gradients are shown in the Supplementary Material, which show similar levels of agreement at high a/L_n , with agreement further improving at smaller a/L_n .

Unlike in the adiabatic-electron case, there is no universal overprediction of the growth rates across devices: Growth rates are being slightly overpredicted in DIII-D for higher wavenumbers ($k_y \rho_{ss} \gtrsim 1.0$) – though this overprediction decreases with increasing electron-temperature gradient – while growth rates in HSX mostly match those from GENE simulations, with exception of the cluster of modes appearing in the low-wavenumber regime of $k_y \rho_{ss} = 0.2$ -0.5. Meanwhile

a consistent overprediction of growth rates persists in W7-X, though the latter is less severe compared with the adiabatic-electron ITG scenario. With regard to the propagation frequency, the inclusion of kinetic electrons has led to a deterioration in the quantitative agreement between the global dispersion model and GENE simulations, with the disagreement being most pronounced in DIII-D (especially at larger wavenumber), while the disagreement in both stellarator configurations has only increased in low- k_y region. Nonetheless, the pertinent qualitative trends of increasing destabilisation and downshift of propagation frequencies into the electron diamagnetic direction as the electron temperature gradient increases are reproduced by the global dispersion model. Obtaining perfect agreement between the model and simulation is, despite the use of exact eigenfunctions for the electrostatic potential in the variational formalism, not expected since the passing electrons have been assumed to be adiabatic in the model.

Analogous to the adiabatic-electron ITG case, we observe a continuous propagation frequency for DIII-D, indicating that the same eigenmode remains the dominant instability at all scales, whereas mode transitions again occur in both HSX and W7-X. The qualitative behaviour of ω_R differs between configurations, which is to be expected as the response of trapped electrons to electrostatic fluctuations is strongly influenced by the details of the magnetic configuration in which they are embedded. Note that despite the fact that in DIII-D ω_R changes from the electron diamagnetic direction to the ion diamagnetic direction as k_y is increased, the underlying instability is not in fact an ITG as temperature gradients are absent, but corresponds to a ubiquitous mode (UM)¹⁰², which is an instability non-resonantly driven by a combination of the ion magnetic drift and bounce-averaged electron drift. As the electron temperature gradient is increased, the destabilising contribution from the electrons to this mode is enhanced (with the latter scaling as⁴⁹ $\gamma \propto \sqrt{1 + \eta_e}$, with $\eta_s = \|\nabla T_s\|/\|\nabla n_s\|$ the gradient-length ratio of kinetic profiles for species s) causing the shift of ω_R to the electron diamagnetic direction. The TEM-UM transition is characterised by the existence of a growth-rate extremum between the drive from resonantly driven TEMs and the non-resonantly driven instability (which coincides with the sign change of ω_R in the absence of temperature gradients¹⁰²). As such a growth-rate extremum is absent for the high-wavenumber modes for $a/L_{Te} \geq 4$, these modes likely correspond to temperature-gradient-driven TEMs, as supported by the stronger scaling of the growth rate with the electron temperature gradient and propagation frequencies that are persistently in the electron diamagnetic direction, where resonances with the precession drift are possible.

Much of the above discussion applies to the high-mirror configuration of W7-X as well, where the majority of the modes are found to propagate in the ion diamagnetic direction, corresponding to the so-called ion-driven trapped electron mode (iTEM)⁴⁹, which may be considered as a general-geometry equivalent to UMs observed in tokamaks. The existence of this instability, originally discovered through gyrokinetic simulations¹¹⁹, is attributable to the (approximate) maximum- J property of this configuration, which makes classical TEMs driven by resonances with the trapped-electron

precession drift (near) impossible. Though, originally this resilience of maximum- J configurations to instabilities driven by the trapped-electron precession drift was shown to hold up to at least²⁵ $\eta_e = 2/3$, it was later proven to persist for arbitrary electron temperature gradients⁴⁹. This finding supports the fairly weak scaling (in comparison to DIII-D) of the propagation frequency with a/L_{Te} in W7-X, despite the $\eta_e = 2/3$ threshold being exceeded. The vacuum high-mirror configuration does not achieve exact maximum- J , with the magnetic wells closer to the inboard side having an overlap between regions of unfavourable curvature (see Figure 2), and indeed, the low-wavenumber modes ($k_y \rho_{ss} \leq 0.6$) are found to propagate in the electron diamagnetic direction and correspond to conventional TEMs – with the exception of the $k_y = 0.3$ mode for $a/L_{Te} = 1$ which corresponds to a different instability as discussed below – though their destabilisation is weak. Likewise, as the configuration is not exactly maximum- J , the electrons are expected to contribute to the drive of the iTEM, explaining the stronger scaling of the eigenfrequency with a/L_{Te} for high-wavenumber modes. The fact that these qualitative trends are observed in both the high-fidelity simulations as well as in the global dispersion relation model, demonstrates the substantial predictive capabilities of the latter.

The most striking differences between the model and GENE simulations are observed in HSX. Whilst good agreement is achieved at high wavenumber and the mode at $k_y \rho_{ss} = 0.1$, there is a strong discrepancy for the modes at $k_y \rho_{ss} = 0.2-0.5$ which show a significantly stronger scaling of the eigenfrequency with a/L_{Te} . The $k_y \rho_{ss} = 0.1$ and high- k_y modes correspond to conventional TEMs, as expected from the driving gradients and the isomorphism of the equilibrium for a quasi-symmetric stellarator and a tokamak, and scale similarly with a/L_{Te} as in DIII-D. The modes within the $k_y \rho_{ss} = 0.2-0.5$ interval are characterised by a unique range in ω_R much larger than those corresponding to TEMs at comparable wavenumbers, and are subject to strong destabilisation by the electron temperature gradient. These modes correspond to the so-called universal instability (UI)^{47,56}, which are characterised by broad eigenmodes along the field line without preferential localisation to any geometric features, occurring typically at long wavelength and low global shear \hat{s} , and are predominantly driven by transit resonances of passing electrons¹⁴⁹. While this instability thrives in weakly sheared slab-like geometries, in other geometries the existence of a shear threshold tends to prevent their presence (with the critical parameter being^{56,150} L_s/L_n , with $L_s \propto \hat{s}$). Therefore, by a combination of the low shear in HSX as well as the high density gradient of $a/L_n = 3$, an ideal situation for the emergence of the UI is created, and in Ref. 57 such modes have been shown to exist in HSX at similar wavenumbers and frequencies. Despite the adiabatic treatment of passing electrons, the global dispersion model manages to qualitatively reproduce the trends in the propagation frequency ω_R for these UI modes, at least for $\eta_e \leq 1$, though erroneously predicting these UI modes to be damped rather than unstable. It should be mentioned, however, that we used the damped approximate eigenfrequency solution to the quadratic dispersion relation [Eqn. (27)] instead of the unstable one as an initial guess for root finding

to obtain this matching solution in ω_R . These results are consistent with the findings of Ref. 47, where it is argued that in the limit of steep density gradients (equivalent to $\eta_e \ll 1$) the UI mode frequency is, to lowest order, purely real and determined by a balance of ion and trapped-electron density fluctuations. To next order, the destabilisation of this mode would subsequently be dominated by the non-adiabatic response of passing electrons. As the latter is absent in our model, we do not expect agreement in the growth rate, and indeed the model predicts that these modes cannot be driven unstable at all. The subsequent deterioration of agreement in the propagation frequency of these UI modes as a/L_{Te} is increased may be attributed to the increasing non-adiabaticity of passing electrons, which no longer perturbatively affect the eigenfrequency like in the steep-density-gradient limit. The emergence of the UI is not a feature unique to HSX, and has also been observed in the high-mirror configuration of W7-X^{21,57}, where despite the higher shear, the TEM drive is sufficiently weakened by the maximum- J property for the UI to become the dominant instability. In fact, the aforementioned non-TEM mode at $k_y \rho_{ss} = 0.3$ observed at the lowest temperature gradient in W7-X in Figure 4 also corresponds to a UI, explaining the erroneously predicted damping rate of that mode by the model.

Application to mixed ITG-TEM case

When a finite ion temperature gradient is considered, the presence of trapped electrons will modify the ITG eigenfrequency with respect to an adiabatic-electron ITG mode at the same gradients, and ITGs and TEMs may now coexist, leading to potential mode transitions between the two instabilities. Whilst the global dispersion model has been shown to adequately resolve the physics of drift resonances for ITG and TEM individually, it needs to be validated in mixed-mode scenarios as well. Here we focus on the results for the a/L_{Ti} scan in absence of electron temperature gradients, shown in Figure 5, where TEMs are driven only by the fixed density gradient. Results for simulations with a finite temperature gradient for both species are shown in the Supplementary Material, in which case with the inclusion of an electron temperature gradient the model generally exhibits even better agreement.

In DIII-D, at moderate temperature gradients ($\eta_i \leq 1$) only a single mode transition is found to occur between $k_y \rho_{ss} = 1.8$ -1.9 for the $a/L_{Ti} = 2$ simulation, which is reproduced by the dispersion model. At those lower temperature gradients the TEM generally transitions to a UM as the wavenumber is increased, with the transition wavenumber decreasing with a/L_{Ti} , as is consistent with analytical theory of Ref. 102. However, as the TEM-to-UM transition occurs close to the growth rate peak, this renders UM increasingly stable at shorter wavelengths. At higher temperature gradients of $a/L_{Ti} \geq 4$ a transition from UM to ITG modes is observed at these shorter wavelengths – with these ITG modes persisting up to $k_y \rho_{ss} = 2$ for $a/L_{Ti} \geq 5$, though transitioning back into UM at $k_y \rho_{ss} = 1.9$ for the $a/L_{Ti} = 4$ case – close to the wavenumber where the growth rate attains a local

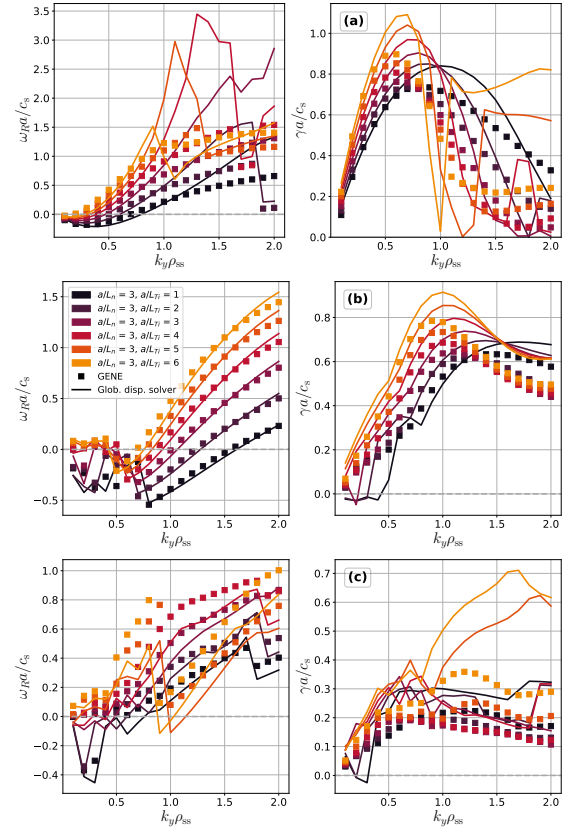


FIG. 5: Eigenfrequency solutions of the global dispersion relation model (solid lines) contrasted with GENE simulations (symbols) including kinetic electrons while varying the ion temperature gradient a/L_{Ti} (lighter colours indicate a stronger temperature gradient). Shown are results for (a) the DIII-D tokamak, (b) the HSX stellarator and (c) the high-mirror configuration of the W7-X stellarator. In all cases, the density gradient is fixed at $a/L_n = 3$ whilst the electron temperature gradient is suppressed ($a/L_{Te} = 0$).

minimum. While the qualitative trends of these mode transitions and the dispersion of the eigenfrequency in DIII-D are captured by the dispersion model, the quantitative agreement with GENE simulations has significantly deteriorated, especially at large a/L_{Ti} , compared with the TEM-dominated case of Figure 4. Remarkably, the model predicts the propagation frequency for these high-wavenumber ITG modes more accurately than for the intermediate-wavenumber UM modes at large a/L_{Ti} , though at the cost of a significantly overestimated growth rate. The eigenmodes of these high-wavenumber high-gradient ITG modes were found to be characterised by more finer-scale substructure (in both $\text{Re}\{\hat{\phi}\}$, $\text{Im}\{\hat{\phi}\}$) beneath the mode envelope (i.e. $|\hat{\phi}|$), thereby classifying them as higher-excitation state ITG. Such higher-excitation state ITG modes are characterised by higher critical gradients for destabilisation, as well as increased stiffness of growth rate with respect to driving gradient once destabilised compared to those of conventional ground-state ITG eigenmodes (i.e. without finer-scale substructure)^{92,151,152}. As a result from this finer-scale

substructure in the eigenfunction, these higher-excitation state ITGs are subjected to stronger Landau damping from parallel dynamics^{34,151}, which is explicitly absent from our model and may explain the strong overprediction of the growth rate for these modes. By contrast, for the intermediate-wavenumber UMs observed for these higher gradients, the model significantly underpredicts the growth rates and overpredicts the propagation frequency, particularly so close to the mode transitions to ITGs. It should be emphasized, however, that these observations about the model's reduced performance in the intermediate-to-high wavenumber range with increasing a/L_{Ti} are specific to the DIII-D flux-tube geometry, rather than a generic property of the model for axisymmetric configurations. Indeed, as shown in the Supplementary Material, the model results are in close agreement with GENE simulations in both of the considered triangularity configurations of the TCV tokamak over the full range of wavenumbers and temperature gradients. As the most significant geometric differences between TCV and DIII-D are found in the safety factor q_0 and magnetic shear \hat{s} [see Table I], with both being $\approx 2.2 - 2.4$ times larger in DIII-D, respectively, the reduction of the model's performance may be attributed to the stronger FLR damping – represented by the modified Bessel functions in the ion resonant integrals of Eqn. (14) – due to the stronger secular increase in $\|\mathbf{k}_\perp\|$. Additionally, the combination of high propagation frequency and low growth rate renders the numerical integration of these resonant integrals increasingly more challenging to accurately resolve, while simultaneously these integrals have a more dominant effect on the dispersion relation, as they are weighted by $\omega_{\nabla T_i} \propto a/L_{Ti}$ in the ion-density kernel [Eqn. (18)]. Both of these explanations do not contradict the high accuracy achieved by the model in the low wavenumber range, where both $\|\mathbf{k}_\perp\|$ as well as the ratio ω_R/γ are much smaller.

For HSX, there is a much clearer distinction between ITG modes and trapped-particle modes compared with DIII-D, with low-wavenumber modes ($k_y \rho_{ss} \leq 0.5$) changing from UI modes to ITG modes, as clearly indicated by the sign reversal of the propagation frequency when the ion temperature gradient exceeds $\eta_i \geq 1$, with the exception of the $k_y \rho_{ss} = 0.2$ mode for $a/L_{Ti} = 3$. In contrast, at higher wavenumber a monotonic change of propagation frequency between electron and ion diamagnetic frequencies occurs, with the associated transition wavenumber and the growth-rate maximum gradually shifting to lower k_y , with the latter also increasing with the ion temperature gradient. By convention, these modes are labelled as iTEMs due to the increasing influence of ions to the instability drive. Remarkably the global dispersion model accurately predicts both growth rates and propagation frequencies – with the exception of the UI modes at $k_y \rho_{ss} \leq 0.4$ being damped, and the $k_y \rho_{ss} = 0.5$ mode at $a/L_{Ti} = 1$ which shows a hybridization between TEM and UI features – for the full temperature gradient and wavenumber range, unlike what has been observed in DIII-D. The growth rates for the intermediate-to-high wavenumber iTEM modes are, however, consistently overestimated, resulting in a small mismatch for the wavenumber at which the growth rate maximum is attained between the high-fidelity simulations and the model,

though the trend of growth rates with k_y are generally preserved for each gradient. As HSX shares many of the main qualitative geometric features with DIII-D due to its quasi-helical symmetry, the main differences being only the lack of exact physical symmetry and a significantly lower magnetic shear [see Table I]. This further enhances the argument of the model's reduced performance in DIII-D being a numerical issue caused by large $\|\mathbf{k}_\perp\|$.

Lastly, for the high-mirror configuration of W7-X we find similar trends as observed in HSX. Aside from the modes at $k_y \rho_{ss} = 0.2, 0.3$ for $a/L_{Ti} \leq 2$ where UIs appear, the presence of a finite ion temperature gradient is sufficient to shift the propagation frequency of all trapped-particle modes that appeared for the a/L_{Te} scan in Figure 4 into the ion diamagnetic direction. By convention this classifies the majority of these modes as iTEMs at lower temperature gradients. At higher temperature gradients $a/L_{Ti} \geq 5$, however, two mode transitions occur around $k_y \rho_{ss} \approx 0.5$ and $k_y \rho_{ss} \approx 0.9$ corresponding to an ITG-to-iTEM and iTEM-to-ITG transition, respectively. At intermediate temperature gradient of $a/L_{Ti} = 4$ ITG modes occur only at $k_y \rho_{ss} = 0.3-0.4$, with remaining modes being iTEM. Whilst these mode transitions between ITG and iTEMs and the qualitative trends among them are well captured by the model, the growth rates are again significantly overestimated, especially for the high-wavenumber ($k_y \rho_{ss} \gtrsim 1$) ITG modes observed for $a/L_{Ti} \geq 5$. The eigenmodes of these high-wavenumber high-gradient ITGs also show higher-excitation state features, similar to what was observed in the DIII-D simulations, explaining the strong overestimation of growth rates for these modes due to the lack of parallel ion dynamics. Unlike the DIII-D case, however, the model does not suffer from a significant overprediction of propagation frequency and underprediction of growth rate of the intermediate wavenumber iTEMs close to the transition point to these higher-excitation state ITG modes. This may again be attributed to the smaller global shear of W7-X, preventing numerical issues from arising due to very large $\|\mathbf{k}_\perp\|$. The global dispersion relation model, however, does predict both propagation frequency and growth rate for the low-wavenumber ITG modes with greater accuracy than the low-wavenumber iTEMs. This may be attributed to the lesser role (compared with iTEMs) of trapped electrons in determining the ITG mode properties, such that the influence of the maximum- \mathcal{J} feature of the geometry – which tends to increase the relative importance of non-adiabatic passing electron response with respect to the trapped-electron response⁴⁷ – is not as prominent for these instabilities.

V. REDUCED FIDELITY PHYSICS MODEL

A. Description of reduced models

Despite the success of the global dispersion relation Eqn. (17) in predicting eigenfrequencies (given a correct eigenmode for $\hat{\phi}$ is provided), its main drawback is the lack of an analytical solution for the resonant ion integrals [Eqn. (14)], requiring evaluation through numerical integra-

tion instead. As this integral contains an oscillatory component, it is prone to either high computational cost or risk of not being well-resolved, which as we have seen in Section IV B is most likely to occur in high-shear devices. By contrast, the trapped-electron resonant integrals [Eqn. (15)] are fully analytic and can thus be computed at relatively low computational cost to machine precision; the resulting pitch angle integral is thus fairly robust to numerical integration, containing no singularities or oscillatory components. Indeed, solving for the eigenfrequency requires no significant additional cost when switching between an adiabatic- and a kinetic-electron description in the model. As Eqn. (17) contains most of the linear collisionless electrostatic physics embedded in the Vlasov-Poisson system, aside from finite ion-transit-effects and a kinetic model for passing electrons, it may be advantageous to consider some reduced-fidelity physics models which allow for analytical solutions to the ion integrals.

FLR effect approximations

The main issue preventing analytical solutions to Eqn. (14) is the coupling between the drift resonance and FLR physics through the Bessel function argument $\hat{b}_j(\xi) = b_j / (1 + i\omega_{j,\nabla B}\xi)$, which arises as a result of the velocity-space asymmetry between the magnetic drift components $\omega_{ds} = \omega_{s,\kappa}(v_{\parallel}/v_{Ts})^2 + \omega_{s,\nabla B}(v_{\perp}/v_{Ts})^2/2$, and the Larmor radius dependence on v_{\perp} . Hence, by leveraging adequate approximations for the magnetic drift and FLR effects, the desired complexity reduction of the ion integral may be obtained. Aside from providing a reduction in computational load for the global dispersion model, the inclusion of such approximations for the drift and FLR physics also allows for probing the sensitivity of a particular instability to the various driving and damping mechanisms, enabling one to make decisions on which physics should be retained when constructing a reduced model to yield eigenmode frequencies within a desired accuracy.

The FLR and toroidal-resonance physics are most straightforwardly decoupled by invoking the DK approximation for the ions as well, therefore taking the $b_j \rightarrow 0$ limit⁴⁴. However, the complete suppression of FLR effects, together with the assumption of streamer-like instabilities with a radial wavenumber $k_x = 0$, implies the eigenfrequency spectrum to be roughly linear in k_y [compare Eqn. (9) and Table III], which only applies up to $k_y\rho_{ss} \approx 0.5$ for most of the cases considered in Section IV. Hence, this approximation will likely be too egre-

gious – as e.g. recently shown by Ref. 153 where growth rates beyond $k_y\rho_{ss} \approx 0.3$ were significantly overpredicted in the DK approximation compared with simulations retaining full FLR effects – and FLR effects should be retained to some degree. In previous works, a Taylor series approach to the FLR damping has been considered, expanding either Γ_0 after integration⁸¹ or expanding J_0^2 before integrating^{42,70}. While these methods yield analytically tractable solutions for the ion integral, they are restrictively limited in their validity to small b , as these (truncated) power series expansions introduce artificial zero crossings at $b \sim \mathcal{O}(1)$ when expanded to any odd order, and rapidly grow without bound beyond $b \sim \mathcal{O}(1)$ for both even and odd order expansions, whilst their unapproximated counterparts are strictly positive and bounded between $[0, 1]$. As $b \propto g^{yy}k_y^2$ and the metric component contains a secular term, such approximations will introduce erroneous physics in our dispersion model even at low k_y when the full effects along the field line are taken into account, especially in high magnetic shear configurations. An alternative approximation to account for FLR damping effects is the Padé approximation $\Gamma_0(b_j) \approx 1/(1+b_j)$, originally considered to remove the deleterious effects introduced by Taylor series approach for intermediate-wavelength modes in gyrofluid models¹⁵⁴. Unlike their Taylor series counterpart, this Padé approximation does not introduce spurious zero crossings, closely captures the behaviour of the modified Bessel function even at $b_j \sim \mathcal{O}(1)$, and smoothly decays at decreasing wavelengths like $\Gamma_0(b_j)$. Although, at very short wavelengths $b_j \gg 1$ the effect of FLR damping is overestimated in the Padé approximation as the proper asymptotic form⁸³ $\Gamma_0(b_j) \sim 1/\sqrt{b_j}$ decays more slowly. As the transport-relevant scales for ITG-TEM driven turbulence are typically long-wavelength, the Padé approximation is thus expected to be adequate to describe the behaviour of the instabilities at the length-scales of interest, since it alleviates the issues that render the Taylor-series approach unsuitable for our model.

The application of the Padé approximation to include FLR effects in the toroidal ITG dispersion relation has recently been considered by Ref. 43, where for unstable modes ($\sigma_\gamma = +1$) and regions of positive curvature it was shown that the ion integrals [Eqn. (14)] have analytical solutions. In Section C 1, we extend the validity of this treatment to arbitrary growth rate and arbitrary sign of the magnetic curvature and derive an alternative derivative-free expression for $J_{j,\parallel}^{(2)}, J_{j,\perp}^{(2)}$. Applying the Padé approximation to the resonant ion integrals of Eqn. (14) as shown in Section C 1 results in the following analytical expressions for the resonant ion integrals:

$$\begin{aligned} J_j^{\text{Padé},0} &= \frac{a_{j,\nabla B}}{\sqrt{g_{\kappa,\nabla B,b}}} \left(i\sqrt{\pi}e^{-\frac{\omega}{2\omega_{j,\kappa}}} Z \left(\sigma_\gamma \sigma_\kappa \sqrt{\frac{a_{j,\kappa}}{2}} \sqrt{g_{\kappa,\nabla B,b}} \right) + 4\pi e^{-a_{j,\nabla B}(1+b_j)} T \left[-i\sigma_\gamma \sigma_\kappa \sqrt{a_{j,\kappa}} \sqrt{g_{\kappa,\nabla B,b}}, \frac{1}{\sqrt{g_{\kappa,\nabla B,b}}} \right] \right), \\ J_{j,\parallel}^{\text{Padé},2} &= -\frac{1}{g_{\kappa,\nabla B,b}} \left(J_j^{\text{Padé},0} + 2a_{j,\nabla B} \left[1 + \sigma_\gamma \sigma_\kappa \sqrt{a_{j,\kappa}} Z \left(\sigma_\gamma \sigma_\kappa \sqrt{\frac{a_{j,\kappa}}{2}} \right) \right] \right), \\ J_{j,\perp}^{\text{Padé},2} &= 2a_{j,\nabla B} \left(J_j^{\text{Padé},0} - \frac{1}{1+b_j} \right) - 2\frac{\omega_{j,\kappa}}{\omega_{j,\nabla B}} J_{j,\parallel}^{\text{Padé},2}, \end{aligned} \quad (28)$$

where we have introduced $a_{j,\kappa} = \omega/\omega_{j,\kappa}$, $a_{j,\nabla B} = \omega/\omega_{j,\nabla B}$ and $\sigma_\kappa = \text{sgn } \omega_{j,\kappa}$, use the short-hand notation $g_{\kappa,\nabla B,b} = 2\omega_{j,\kappa}(1+b_j)/\omega_{j,\nabla B} - 1$, and $T[h,a]$ is the Owen's T-function¹⁵⁵. The only remaining validity limit to Eqn. (28) is that the expression for $J_j^{\text{Padé},0}$ was obtained under the assumption that $\omega_{j,\kappa}/\omega_{j,\nabla B} > 0$ [though the expressions for $J_{j,\parallel}^{\text{Padé},2}$ and $J_{j,\perp}^{\text{Padé},2}$ are generally valid if one computes $J_j^{\text{Padé},0}$ numerically from Eqn. (C1) in those cases instead]. Using Eqn. (24), the validity of this assumption can be estimated to hold up to plasma pressures of $\beta^{\text{crit}} \sim \mathcal{O}(a/R)$, with R the major radius. For the devices considered here, the tokamaks are characterised by $\beta^{\text{crit}} \approx 0.3$, while for the stellarators $\beta^{\text{crit}} \approx 0.1$, far above the thresholds where electromagnetic effects have a non-negligible influence on the ITG^{9,10}, such that Eqn. (28) is adequate within the electrostatic approximation considered in this work. In the limit of $\sigma_\kappa = \sigma_\gamma = +1$, the expression of $J_j^{\text{Padé},0}$ reduces to that obtained in Appendix B of Ref. 43. The DK limit is then straightforwardly obtained from Eqn. (28) by setting $b_j = 0$, and in Section C 2 we show if one further assumes $\omega_{j,\kappa} \approx \omega_{j,\nabla B}$, consistent with $\beta \approx 0$, that $J_j^{\text{Padé},0}$ reduces to

$$J_j^{\text{DK},0} = \lim_{\omega_\kappa \rightarrow \omega_{\nabla B}} \lim_{b \rightarrow 0} J_j^{\text{Padé},0} = \frac{a_{j,\kappa}}{2} Z \left(\sigma_\gamma \sigma_\kappa \sqrt{\frac{a_{j,\kappa}}{2}} \right)^2,$$

which when substituted in Eqn. (28) to obtain expressions for $J_{j,\perp}^{(2)}$ and $J_{j,\parallel}^{(2)}$ in the DK limit, reduces the adiabatic-electron dispersion relation for ITG modes [Eqn. (12) with the trapped-particle contribution suppressed] to the well-known BDR result⁴⁴ [D_0 in Eqn. (3) therein] under the conventional assumptions of $\sigma_\gamma = \sigma_\kappa = +1$, see Eqn. (C15).

Magnetic drift approximations

Aside from approximating the FLR effects, another method to decrease the complexity of the resonant ion integrals in Eqn. (14) is to reduce the velocity-space asymmetry of the magnetic drift. By noting that, in the absence of temperature anisotropy, the equipartition theorem predicts that $\langle v_\parallel^2 \rangle = \langle v_\perp^2 \rangle/2$, we can consider two approximations to the magnetic drift⁷⁰,

$$\omega_{ds} \approx \begin{cases} (\omega_{s,\kappa} + \omega_{s,\nabla B}) \frac{v_\parallel^2}{v_{Tj}^2} & \text{curvature model} \\ (\omega_{s,\kappa} + \omega_{s,\nabla B}) \frac{v_\perp^2}{2v_{Tj}^2} & \nabla B \text{ model} \end{cases}. \quad (29)$$

Henceforth, we shall refer to the unapproximated drift $\omega_{ds} = \omega_{s,\kappa}(v_\parallel/v_{Ts})^2 + \omega_{s,\nabla B}(v_\perp/v_{Ts})^2/2$ as the “full-drift” model. Comparing the “full drift” case to Eqn. (29), we observe that these drift models effectively reduce to a pure curvature or ∇B drift, but at an augmented magnitude, which in turn reduces the resonance condition $\omega \sim \omega_{ds}$ from a curved surface in velocity space to a simple plane¹⁵⁶. Those approximations alleviate the complexity of the denominators in Eqn. (14), as the integer power terms are attributable to the ∇B drift, while

the half-integer powers are attributable to the curvature drift. In Section C 3, we show that with the curvature model, it is possible to obtain analytical expressions for Eqn. (14) as

$$\begin{aligned} J_j^{\text{curv},0} &= -\Gamma_0(b_j) \sigma_\gamma \sigma_{d,j} \sqrt{\frac{a_{d,j}}{2}} Z \left(\sigma_\gamma \sigma_{d,j} \sqrt{\frac{a_{d,j}}{2}} \right), \\ J_{j,\perp}^{\text{curv},2} &= -2 \frac{d(b_j \Gamma_0(b_j))}{db_j} \sigma_\gamma \sigma_{d,j} \sqrt{\frac{a_{d,j}}{2}} Z \left(\sigma_\gamma \sigma_{d,j} \sqrt{\frac{a_{d,j}}{2}} \right), \\ J_{j,\parallel}^{\text{curv},2} &= -\Gamma_0(b_j) a_{d,j} \left[1 + \sigma_\gamma \sigma_{d,j} \sqrt{\frac{a_{d,j}}{2}} Z \left(\sigma_\gamma \sigma_{d,j} \sqrt{\frac{a_{d,j}}{2}} \right) \right], \end{aligned} \quad (30)$$

where we have introduced $a_{d,j} = \omega/(\omega_{j,\kappa} + \omega_{j,\nabla B})$ and $\sigma_{d,j} = \text{sgn}(\omega_{j,\kappa} + \omega_{j,\nabla B})$. This analytical simplification is facilitated by a decoupling of the FLR and drift physics, since by virtue of the curvature model we have $\hat{b}_j(\xi) \rightarrow b_j$. With these approximations, the ion-density kernel in Eqn. (18) reduces to

$$\begin{aligned} h_{\text{ion},j}^{\text{curv}} &= \frac{\omega_{\nabla T_j}}{2\omega} \Gamma_0(b_j) a_d \left(1 + \sigma_\gamma \sigma_{d,j} \sqrt{\frac{a_{d,j}}{2}} Z \left(\sigma_\gamma \sigma_{d,j} \sqrt{\frac{a_{d,j}}{2}} \right) \right) \\ &\quad - \sigma_\gamma \sigma_{d,j} \sqrt{\frac{a_{d,j}}{2}} Z \left[\sigma_\gamma \sigma_{d,j} \sqrt{\frac{a_{d,j}}{2}} \right] \left(\Gamma_0(b_j) \times \right. \\ &\quad \left. \left[1 - \frac{\omega_{\nabla n_j}}{\omega} + \frac{\omega_{\nabla T_j}}{2\omega} \right] - \frac{\omega_{\nabla T_j}}{\omega} b_j [\Gamma_1(b_j) - \Gamma_0(b_j)] \right), \end{aligned} \quad (31)$$

which under the conventional assumptions of $\sigma_\gamma = \sigma_{d,j} = +1$ reduces to the form obtained by Refs. 156 and 157 in Eqns. (11) and (18), respectively.

The ∇B model does not allow for similar simplifications of Eqn. (14), as the coupling between FLR and drift physics remains in $\hat{b}_j(\xi)$. Nonetheless, the ∇B model does provide a reduction in the numerical cost of calculating the resonant ion integrals, as it reduces $J_{j,\parallel}^{\nabla B,2} \rightarrow J_{j,\parallel}^{\nabla B,0}$, thereby making one of the integrals redundant. It has been shown that the ∇B model provides a better approximation to the full-drift model than the curvature model⁷⁰ (at small wavenumbers), whilst simultaneously providing reasonable agreement with the full-drift model even at intermediate wavenumbers $b \approx 0.6$ where FLR effects become more relevant. Although this latter observation is attributable to the coupling between FLR and drift physics, which is lost in the curvature model, the former observation at low wavenumbers $b \ll 1$ is due to the fact that the v_\perp^2 resonance of the ∇B model is accessible in a larger region of velocity space than the v_\parallel^2 resonance of the curvature model, and thus more closely approximates the true resonant surface of the full-drift model. By additionally invoking the Padé approximation for the Bessel function, we show in Section C 4 that, again, the resonant ion integrals become analyt-

ically tractable,

$$\begin{aligned}
J_j^{\nabla B + \text{Padé},0} &= -a_{d,j} e^{-a_{d,j}(1+b_j)} E_1 \left(-a_{d,j}(1+b_j) \right), \\
J_{j,\perp}^{\nabla B + \text{Padé},2} &= -2a_{d,j} \left[\frac{1}{1+b_j} + a_{d,j} e^{-a_{d,j}(1+b_j)} \times \right. \\
&\quad \left. E_1 \left(-a_{d,j}(1+b_j) \right) \right], \\
J_{j,\parallel}^{\nabla B + \text{Padé},2} &= J_j^{\nabla B + \text{Padé},0},
\end{aligned} \tag{32}$$

where $E_1(z) = \int_z^\infty dt e^{-t}/t$ is the exponential integral. For this double approximation, the ion-density kernel in Eqn. (18) becomes

$$\begin{aligned}
h_{\text{ion},j}^{\nabla B + \text{Padé}} &= \left(\frac{\omega \nabla n_j}{\omega} - 1 + \frac{\omega \nabla T_j}{\omega} (a_{d,j} - 1) \right) a_{d,j} \times \\
&\quad e^{-a_{d,j}(1+b_j)} E_1 \left(-a_{d,j}(1+b_j) \right) + \frac{\omega \nabla T_j}{\omega} \frac{a_{d,j}}{1+b_j},
\end{aligned} \tag{33}$$

which in the DK limit of $b_j \rightarrow 0$ agrees with Eqn. (19) from Ref. 69. We note, however, that while we focus on the explicit simplification of the ion-density kernel in these reduced models, the trapped-electron pitch-angle density kernel $K_{\text{tr-el}}$ in Eqn. (18) is also implicitly modified when invoking the curvature- or ∇B -model, as this affects the computation of the bounce-averaged drift accordingly,

$$\overline{\omega_{de}^T} \approx \begin{cases} \overline{(\omega_{e,\kappa} + \omega_{e,\nabla B}) (1 - \lambda B)} & \text{curvature model} \\ \overline{(\omega_{e,\kappa} + \omega_{e,\nabla B}) \lambda B} & \nabla B \text{ model} \end{cases}. \tag{34}$$

Making simplifications to the FLR term leaves $K_{\text{tr-el}}$ unaffected, as the trapped electrons have been treated drift-kinetically.

Eigenmode proxies

Additionally, though the global dispersion model is not fully self-consistent, its variational nature allows us to use simplified proxy functions for the eigenmode structure to obtain a close approximation to the eigenmode frequency, provided the $\hat{\phi}$ proxy is reasonably accurate. Here we briefly and non-exhaustively consider two choices for an eigenmode guess: the so-called flute mode $\hat{\phi} \approx \phi_0$ with ϕ_0 constant or a Gaussian $\hat{\phi}(z) = e^{-z^2/2}$. Although a relatively severe approximation, flute modes are considered in TEM stability analysis to study geometric effects^{21,24,158}, which, unlike the eigenfunction, are known a priori. Meanwhile, Gaussian trial functions can be justified from ITG theory, where the lowest-order eigenfunction in a quadratic drift well is Gaussian^{33,34,159}, though with a width parameter that needs to be determined self-consistently. In reduced modelling efforts for tokamaks, a similar basis-function expansion as for the quadratic well is applied to the eigenmode, where the (Gaussian) eigenmode width is an exploitable variational parameter^{160–163}. Our main

goal of adopting these eigenmode proxies is to probe the model's sensitivity to the eigenfunction shape. The results presented here therefore mainly serve as a baseline for the model's performance with poor proxy functions when compared with the exact GENE eigenfunctions, rather than providing any degree of fidelity. The flute mode is expected to be a particularly poor eigenfunction, as it fails to localise the instability to geometric features, while the fixed Gaussian-width approach captures localisation to the outboard magnetic well, though it fails to capture the increasing mode localisation with k_y due to FLR effects. As there is only one magnetic well in a tokamak to which the eigenmode can be localised, with curvature typically being worst at the outboard, we expect better performance of this proxy in axisymmetric configurations than in low-shear stellarators, where the exact mode may be highly extended at low k_y or localised to other magnetic wells at high k_y when FLR damping increases in importance. Ultimately, the variational nature of the model would most benefit from more intermediate-fidelity proxies that are better informed about the underlying instability physics.

In case of the Gaussian trial function we adopt the same ballooning-space domain for the eigenmode as considered in the GENE simulations, i.e. we use the same n_{kx} as in Table II to construct the geometry beyond the $2\pi N_{\text{pol}}$ extent of the flux tube. The flute mode proxy, however, violates the boundary condition of the ballooning formalism (see Section III C), and would consequently result in spurious unbounded contributions to the mode drive in the global dispersion relation [Eqn. (17)] in an (infinitely) extended geometry. Hence, to accommodate this artificial proxy, we assume an unsheared magnetic field (consistent with periodicity of the eigenmode proxy), allowing us to limit the effects of geometry on the eigenfrequency to within the original $2\pi N_{\text{pol}}$ extent of the flux tube.

In order to assess the effect of these approximations on the eigenfrequency, as well as whether they affect our ability to maintain the fundamental physics for toroidal ITGs and TEMs, we apply each set of these reduced models to one adiabatic-electron ITG case at gradients of $a/L_n = 2$, $a/L_{Ti} = 4$, and one purely density-gradient-driven kinetic electron case at $a/L_n = 3$ in the absence of temperature gradients. For simplicity, the adiabatic-electron case does not contain impurities, though the chosen gradients correspond to the nominal values considered for the Z_{eff} scan discussed in Section IV A. Likewise, the density gradient considered for the kinetic-electron case corresponds to the nominal value considered in both the a/L_{Ti} and a/L_{Te} scans discussed in Section IV B, where the absence of temperature gradients prompts the instabilities to be either a trapped-particle mode or, if the shear is sufficiently low, a UI.

B. Application to DIII-D

The results for eigenfrequencies obtained by the global dispersion model in DIII-D geometry using the various reduced models are shown in Figure 6. The results obtained from the GENE simulations as well as from the baseline global dis-

persion model in absence of further approximations are also shown to provide a reference. Focussing on the adiabatic-electron ITG scenario (see Figure 6a) – where we expect the model reductions to have most significant impact as they directly modify the functional properties of the ion resonant integrals [Eqn. (14)], whilst the mapping properties of the trapped-electron resonant integrals [Eqn. (15)] into the complex plane remain unaltered aside from a change in the value of $\overline{\omega_{de}^T}$ – we observe that, in general, the introduction of the Padé approximation (orange lines) yields the smallest discrepancy with respect to the baseline model (blue lines), with noticeable differences emerging particularly in the growth rate from $k_y \rho_{ss} \approx 0.8$ onwards; the higher- k_y growth rates are systematically overpredicted up to $k_y \rho_{ss} \approx 1.7$ compared with when full FLR effects are retained, and thereafter underpredicted at higher wavenumber. This observation is consistent with the fact that the Padé approximation $\Gamma_0(\hat{b}_j) \approx 1/(1 + \hat{b}_j)$ decays less rapidly than $\Gamma_0(\hat{b}_j)$ itself from $|\hat{b}_j| \leq 3$, while thereafter decaying more rapidly for larger $|\hat{b}_j|$. With respect to the drift models, the ∇B -model (in combination with the Padé approximation) better captures the growth rate than the curvature model does, which is consistent with the observation from Ref. 70 about the relative areas of the resonant surfaces in velocity space between these two models; the opposite trend between drift models occurs for the propagation frequencies. Note, however, that with the curvature model approximation, the global dispersion relation model could not find any solutions for $k_y \rho_{ss} = 0.1$ and $k_y \rho_{ss} > 1.3$ satisfying $D = 0$, with root finding methods converging onto modes with vanishingly small numerical growth/damping rates, for which the validity condition for Eqn. (11) used to derive Eqn. (32) is stretched to its limits, and are hence omitted from Figure 6a. Lastly, with respect to the proxy functions for the electrostatic potential, the Gaussian proxy yields significantly better results than the flute mode proxy, as would be expected, thereby further cementing the variational aspect of the dispersion relation. Additionally, when using the flute mode proxy the model is only capable of finding solutions for $k_y \rho_{ss} \leq 1.4$. At higher wavenumbers the initial guesses obtained from the high-frequency limit of the dispersion relation [Eqn. (27)] only yield purely real-valued frequencies for the flute mode proxy, for which the validity of Eqn. (11) is violated, hence such points are also omitted from Figure 6a. With regard to the Gaussian trial function, it should be noted, however, that the closer agreement (compared with the baseline model using high-fidelity eigenfunction) between growth rates predicted by the dispersion model and GENE for intermediate wavenumbers should be considered as coincidental, as the model is still lacking the physics associated with finite-transit effects that would be required to obtain a one-to-one match.

Many of the observations regarding the influence of approximations in the model for adiabatic-electron ITG case are also directly reflected in the TEM scenario, with the discrepancy between the Padé and full-FLR model being quantitatively comparable to the adiabatic-electron ITG case, though qualitatively less severe as the discrepancy is consistent at high k_y . This is to be expected as the mode is predominantly driven by the trapped-electron precession resonance

and thus less strongly affected by FLR damping. Similarly as in the ITG case, the curvature model does yield consistently lower growth rates than the ∇B model, though there is a stronger discrepancy in ω_R with respect to the baseline model in comparison to the adiabatic-electron ITG scenario. Remarkably, the ∇B model exhibits only a moderate discrepancy in growth rate (up to $k_y \rho_{ss} \approx 1$) though a similar mismatch in ω_R is observed as in the ITG case. The lower sensitivity of the growth rate to the chosen drift model can be explained from Eqn. (34), as the bounce-averaged drift is dominated by contributions near the bounce points ($\lambda B \approx 1$) where trapped-particles spend most of their time, for which the curvature component to the magnetic drift is nearly vanishing, such that the ∇B model does not significantly affect which trapped-particle population is in resonance. However, as these particles now experience an augmented drift frequency, the mode frequency ω_R must be equivalently increased to remain in resonance, explaining the stronger discrepancy in ω_R compared with the adiabatic-electron ITG case. Likewise, the Gaussian proxy yields eigenfrequencies close to those obtained with the GENE eigenfunction with the baseline model at low wavenumber, though significant deviations occur in the growth rate beyond $k_y \rho_{ss} \approx 1$. This may be attributed to the widening and flattening observed in the GENE UM eigenmode structures compared with the GENE TEM mode structures, while the proxies' width is fixed. Additionally, the flute mode proxy, despite its relentless simplicity, manages to provide reasonably accurate predictions for the propagation frequencies – outperforming even both options for reduced drift models when high-fidelity eigenfunctions are used – though provides a less accurate predictions for the growth rate. Nonetheless, the growth rate predictions are comparable to those obtained with the curvature model up to $k_y \rho_{ss} \approx 1$ with errors further decreasing for higher wavenumber, while with respect to the ∇B model the opposite trend is observed. This further exemplifies the variational nature of the model when kinetic electron physics is included.

C. Application to W7-X

Results for the use of reduced models on the eigenfrequency of adiabatic-electron ITG and density-gradient-driven TEM in the high-mirror configuration of W7-X are shown in Figures 7a and 7b, respectively. Many of the pertinent features observed in DIII-D carry over to the high-mirror configuration of W7-X, with in particular the Padé approximation continuing to yield the best match to the baseline model. The most notable differences are the lack of mode transitions occurring when using the eigenmode proxies, which is to be expected as these are facilitated by changes in $\hat{\phi}$ obtained from GENE, as well as the worsening of the discrepancies between the use of proxies and the baseline model using exact eigenfunctions.

In particular both proxies suffer considerably from the existence of a finite range of wavenumbers for which the high-frequency limit of the dispersion relation [Eqn. (27)] predicts complex-valued rather than real-valued eigenfrequencies, which renders the applicability of the model invalid out-

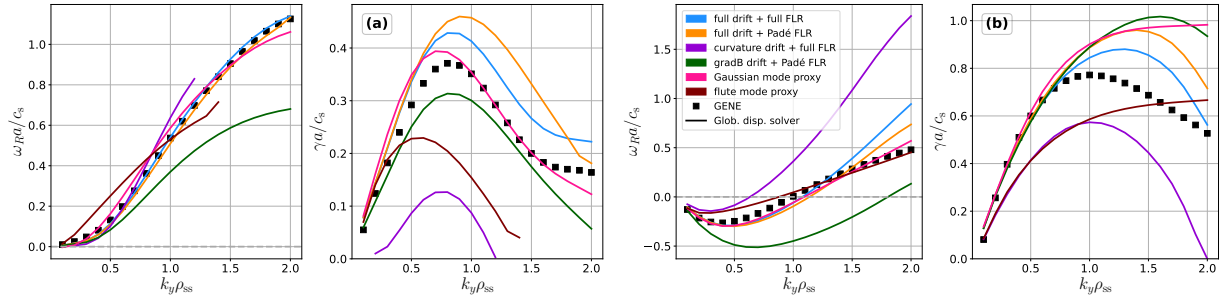


FIG. 6: Influence of the different reduced models for the FLR damping, drift approximation, and eigenfunction proxies on the eigenfrequency solutions obtained by the global dispersion relation model (solid lines) contrasted with GENE simulations (symbols) in DIII-D geometry. Shown are (a) an adiabatic-electron ITG case with $a/L_n = 2$, $a/L_{Ti} = 4$, and (b) adensity-gradient-driven TEM case with $a/L_n = 3$. For comparison, the solution of the baseline global dispersion model without any of the aforementioned approximations is added in blue. Note that the GENE eigenfunctions for $\hat{\phi}$ are used for the cases with drift and FLR approximations, while the eigenfunction proxy cases retain the full FLR and drift physics.

side of those ranges, with this issue significantly exacerbated in W7-X compared with DIII-D. Remarkably, the range of wavenumbers where the model's validity is not violated is slightly smaller for the kinetic-electron TEM case compared with the adiabatic-electron ITG case. The poorer performance of the proxies in W7-X indicates that mode localisation is more complicated in (low-shear) stellarators like W7-X compared with tokamaks, necessitating the development of more realistic mode proxies than considered in this work. The fact that the kinetic-electron TEM scenario is more susceptible to this issue compared with the adiabatic-electron ITG scenario – despite the proper variational nature of the model in the former compared with the ad-hoc applicability in the latter – may be explained from the variation of the magnetic field strength along the field line, see Figure 2. The trapped-electron populations are strongly affected by $\|\mathbf{B}\|$ through the distribution of the magnetic wells and corresponding bounce-averages. In the tokamak case, there is only one of those wells (though infinitely repeated in ballooning space), spanning the extent of a single poloidal turn, which is similar to the extent of both eigenfunction proxies. In W7-X, by contrast, there are multiple non-equivalent wells within a single poloidal turn, resulting in a mismatch between the broad extents of the eigenfunction proxies and the more narrow extents along the field line that are accessible to different trapped-particle populations, which are crucial to mode localisation for TEMs. By comparison, the variation of $\|\mathbf{B}\|$ only affects the ions by slightly modifying the argument of the Bessel function and the amplitude of the magnetic drifts (see Table III), though this variation is negligible compared with the change in $\|\mathbf{k}_\perp\|$ and the drift-operator \mathcal{L}_y , which have broader extents along the field line compared with the magnetic wells.

With regard to the use of the drift approximations, the most striking difference compared with DIII-D occurs in the adiabatic-electron ITG scenario. In W7-X we observe that the ∇B model no longer universally yields larger (and more accurate) growth rates compared with the curvature model. In fact, for the adiabatic-electron ITG case at high k_y , the curva-

ture model yields better ω_R and γ (with respect to the baseline model). This may be explained in terms of the significantly weaker FLR damping due to the lower shear, which quenches instability drive in DIII-D. Hence, it must be concluded that as far as the ITG is concerned, FLR damping is a more crucial component to determining the overall stability than the total area of the resonant surface in velocity space, otherwise the performance of the reduced model would have been universal across the two geometries. This is in line with the observation that mode localisation of adiabatic-electron ITG is most strongly correlated with $\|\mathbf{k}_\perp\|$, while growth rates are subsequently most strongly correlated with the regions of curvature that are sampled within the extent of the mode¹³². However, no substantial qualitative differences between W7-X and DIII-D occur for the behaviour of the reduced drift models in the TEM scenario.

VI. SUMMARY

We have developed a field-line global dispersion relation for electrostatic (toroidal) ITG and TEM in arbitrary toroidal geometry, retaining FLR damping for ions and drift resonances for both ionic and electron species (semi-)analytically. This model is not only shown to satisfy a variational property, but is valid for arbitrary sign of the growth rate and magnetic curvature, and is shown to agree with conventional treatments for unstable modes with matching sign of curvature, for which the dispersion relation is more straightforward to obtain based on the integral formulation of the plasma dispersion function [Eqn. (16)]. Such a sign generalisation is crucial for the variational formulation, as the latter is obtained by integrating the dispersion relation along the helical magnetic field line, on which the curvature drift is bound to change sign. Although this variational formulation only applies when the effect of kinetic electrons is considered, the same global dispersion relation is considered as an ad-hoc model for including non-local effects along the field line for adiabatic-electron ITG.

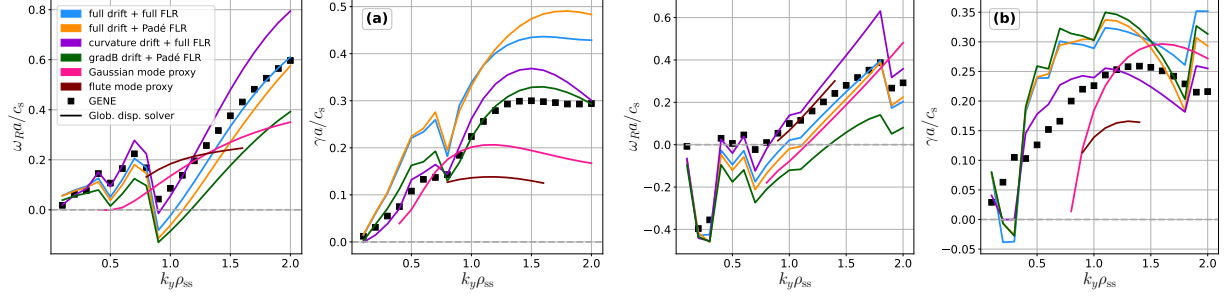


FIG. 7: Influence of the different reduced models for the FLR damping, drift approximation, and eigenfunction proxies on the eigenfrequency solutions obtained by the global dispersion relation model (solid lines) contrasted with GENE simulations (symbols) in the geometry of the high-mirror configuration in W7-X. Shown are (a) an adiabatic-electron ITG case with $a/L_n = 2$, $a/L_{Ti} = 4$, and (b) adensity-gradient-driven TEM case with $a/L_n = 3$. For comparison, the solution of the baseline global dispersion model without any of the aforementioned approximations is added in blue. Note that the GENE eigenfunctions for $\hat{\phi}$ are used for the cases with drift and FLR approximations, while the eigenfunction proxy cases retain the full FLR and drift physics.

The applicability of this model in predicting ITG-TEM eigenfrequencies in both its ad-hoc and variational states is studied by comparing against GENE simulations in both tokamak and stellarator geometries, where the exact GENE eigenfunctions for the electrostatic potential are used as trial functions. The complex eigenfrequencies produced by the model are generally in quantitative agreement with the gyrokinetic simulations, especially at transport-relevant long wavelengths. Significant deviations in that regime are predominantly observed for low-shear stellarator geometries when kinetic electrons are considered, and are attributable to the lack of non-adiabatic passing-electron physics as required to describe the Universal Instability, which is observed at these low wavenumbers in high-fidelity simulations. Additionally, when kinetic electrons are considered, the model significantly overestimates the growth rate at short wavelengths at large ion temperature gradient in DIII-D and the high-mirror configuration of W7-X, though not in HSX. These discrepancies are attributed to higher-excitation state of ITG modes that are found in GENE simulations in the former set of configurations, which are more sensitive to the parallel ion dynamics that have been neglected in the model. Barring these exceptional cases, in general, the agreement between the model and the high-fidelity simulations is worst for the high-mirror configuration of W7-X. This, however, is caused by peculiarities in the geometric features of a maximum- J configuration, as the model yields eigenfrequencies with similar agreement as in DIII-D and HSX for the negative-mirror configuration of W7-X – which is distinctively not maximum- J – as shown in the Supplementary Material. Additionally, we have investigated a set of common approximations for their suitability to enhance the analytical malleability of the ion resonant integral, which may be challenging to numerically resolve as a result of coupling between the FLR damping term and the drift resonances. Such numerical limitations can particularly gain in prominence when the global magnetic shear is high, resulting in $\|\mathbf{k}_\perp \rho_s\| \gg 1$ even at moderate values of the bi-normal wavenumber $k_y \rho_{ss} \sim \mathcal{O}(1)$,

as has been observed in DIII-D. It is found that invoking a Padé approximation $\Gamma_0(\hat{b}_j) \approx (1 + \hat{b}_j)^{-1}$ enables analytical solutions of this integral whilst consistently yielding the smallest deviations in the eigenfrequency with respect to the baseline model.

Several improvements of the global dispersion model are still necessary. First and foremost, the electrostatic-potential eigenfunction needs to be determined self-consistently, rather than provided as input from linear gyrokinetic simulations. Such an approach is, however, beyond the scope of this work, where we emphasize the validation of the relevant geometry-based driving and damping physics of the model. If a self-consistent determination is not feasible, then more suitable eigenfunction proxies than the rudimentary fixed-width Gaussian and flute mode considered in Section V will need to be developed, such that the variational nature of the dispersion relation can be fully exploited. For future work we consider furthermore including the effect of a finite-transit-frequency correction to the ion response, as explicitly done in the non-resonant limit ($\omega_{di}/\omega \ll 1$) by e.g. Refs. 33, 69, and 164, which removes the ad-hoc nature of the model when applied to adiabatic-electron ITG scenario and may reduce the over-prediction of growth rates due to missing Landau damping associated with particle streaming. Furthermore, we shall strive to include kinetic effects for passing electrons to extend the applicability of the model towards UI and, at shorter wavelengths than those considered here, ETG modes. Lastly we note that the analytical approaches we have considered for the global dispersion model are not limited in their applicability to studying microinstabilities, for similar velocity-space integrals over toroidal resonances in the non-adiabatic distribution are found in the evaluation of quasilinear weights for the calculation of ion and electron fluxes^{165–167}. As the calculation of such quasilinear weights also involve a field-line integral over the resonant velocity moments, similar to D_{glob} , they may benefit from the sign generalisations developed in this work to correctly account for the contributions of regions

of opposing curvature drift.

ACKNOWLEDGMENTS

We would like to thank P. Costello, G.G. Plunk, and P. Helander for insightful physics discussions, as well as the GENE Development Team for providing support. Additionally we express our gratitude towards C.D. Stephens, J. Citrin and A.G. Goodman for their advice on the numerical framework used to solve our dispersion relation model, as well as T. Romba and F. Reimold for providing insights into experimentally accessible impurity parameters. Figures in Section IV have been made possible by using the colourmaps available in the open-source CMasher package¹⁶⁸. Simulations were performed on the HPC system Viper at the Max Planck Computing and Data Facility and the HPC system Marconi at the CINECA consortium.

This work has been carried out within the framework of the EUROfusion Consortium, funded by the European Union via the Euratom Research and Training Programme (Grant Agreement No 101052200 – EUROfusion). Views and opinions expressed are however those of the author(s) only and do not necessarily reflect those of the European Union or the European Commission. Neither the European Union nor the European Commission can be held responsible for them.

Appendix A: Derivation of the resonant ion- and electron dispersion integrals

1. Ion dispersion integral

As within the model the ion population is described locally and trapping effects are neglected, one may use v_{\parallel}, v_{\perp} as independent velocity coordinates⁶⁹, making the ion integral most suitable to treat with normalised cylindrical velocity coordinates $\{x_{\parallel}, x_{\perp}\} = \{v_{\parallel}, v_{\perp}\}/v_{Ts}$. In those coordinates, the single-particle Maxwellian takes the convenient parametrised form $\mathcal{F}_{Ms} d^3\mathbf{v}_s = \mathcal{N}_{x_{\parallel}}(0, 1) \mathcal{N}_{x_{\perp}}(0, 1) x_{\perp} dx_{\perp} dx_{\parallel} d\vartheta / \sqrt{2\pi}$ where

$$\mathcal{N}_z(\mu, \sigma) = \frac{1}{\sqrt{2\pi\sigma^2}} \exp\left(-\frac{(z-\mu)^2}{2\sigma^2}\right) \quad (\text{A1})$$

is the parametrised normal distribution, where $\vartheta = [0, 2\pi)$ is the gyrophase angle. In what follows we primarily use the subscript i instead of s , though the result also holds for the other (impurity) species.

The ion resonant integral from Eqn. (9) is most straightforwardly treated by simplifying the frequency fraction as $(\omega - \omega_{*i}^T)/(\omega - \omega_{di}) = 1 + (\omega_{di} - \omega_{*i}^T)/(\omega - \omega_{di})$, yielding

$$\int \frac{\omega - \omega_{*i}^T}{\omega - \omega_{di}} \mathcal{F}_{Mi} J_0(k_{\perp} \rho_i)^2 d^3\mathbf{v}_i = \Gamma_0(b_i) + \underbrace{\sqrt{2\pi} \int_{-\infty}^{\infty} dx_{\parallel} \int_0^{\infty} dx_{\perp} \frac{\omega_{di} - \omega_{*i}^T}{\omega - \omega_{di}} \mathcal{N}_{x_{\parallel}}(0, 1) \mathcal{N}_{x_{\perp}}(0, 1) x_{\perp} J_0(\sqrt{b_i} x_{\perp})^2}_{=I_i^{\text{tor}}} \quad (\text{A2})$$

where we introduced $b_i = (k_{\perp} \rho_{Ti})^2$, the frequency-independent integral was solved in terms of Weber integrals¹⁰¹, and $\Gamma_n(z) = \exp(-z) I_n(z)$ denote the exponentially scaled modified Bessel functions of the first kind. Here we will focus on the integral I_i^{tor} containing the toroidal drift resonance, which, after applying Eqn. (11) and using the explicit velocity dependence of the diamagnetic drift $\omega_{*i}^T = \omega_{\nabla n_i} + \omega_{\nabla T_i} \left((x_{\parallel}^2 + x_{\perp}^2)/2 - 3/2 \right)$ and magnetic drift $\omega_{di} = \omega_{i,\kappa} x_{\parallel}^2 + \omega_{i,\nabla B} x_{\perp}^2/2$, reduces to

$$I_i^{\text{tor}} = -\frac{\omega_{\nabla n_i} - \frac{3}{2} \omega_{\nabla T_i}}{\omega} J_{\parallel,\perp}^{0,0} + \frac{\omega_{i,\nabla B} - \omega_{\nabla T_i}}{2\omega} J_{\parallel,\perp}^{0,2} + \frac{\omega_{i,\kappa} - \frac{1}{2} \omega_{\nabla T_i}}{\omega} J_{\parallel,\perp}^{2,0} \quad (\text{A3})$$

where we introduced the following generic integrals

$$J_{\parallel,\perp}^{n,m} = \frac{\omega}{i\sigma_{\gamma}} \sqrt{2\pi} \int_0^{\infty} d\xi e^{i\sigma_{\gamma} \omega \xi} \int_{-\infty}^{\infty} dx_{\parallel} \mathcal{N}_{x_{\parallel}}(0, 1) x_{\parallel}^n e^{-i\sigma_{\gamma} \omega_{i,\kappa} x_{\parallel}^2 \xi} \times \int_0^{\infty} dx_{\perp} \mathcal{N}_{x_{\perp}}(0, 1) x_{\perp}^{m+1} J_0(\sqrt{b_i} x_{\perp})^2 e^{-i\sigma_{\gamma} \frac{\omega_{i,\nabla B}}{2} x_{\perp}^2 \xi}. \quad (\text{A4})$$

The velocity integrals in Eqn. (A4) may be performed analytically by virtue of coordinate transforms $u_{\parallel} = x_{\parallel} \sqrt{1 + 2i\sigma_{\gamma} \omega_{i,\kappa} \xi}$ and $u_{\perp} = x_{\perp} \sqrt{1 + i\sigma_{\gamma} \omega_{i,\nabla B} \xi}$, such that the exponential terms can be consolidated into a standard normal distribution in the new coordinates, yielding

$$J_{\parallel,\perp}^{n,m} = \frac{\omega\sqrt{2\pi}}{i\sigma_\gamma} \int_0^\infty d\xi \frac{e^{i\sigma_\gamma\omega\xi}}{(1+2i\sigma_\gamma\omega_{i,\kappa}\xi)^{\frac{n+1}{2}} (1+i\sigma_\gamma\omega_{i,\nabla B}\xi)^{\frac{m+2}{2}}} \int_{-\infty\sqrt{1+2i\sigma_\gamma\omega_{i,\kappa}\xi}}^{\infty\sqrt{1+2i\sigma_\gamma\omega_{i,\kappa}\xi}} du_{\parallel} \mathcal{N}_{u_{\parallel}}(0,1)u_{\parallel}^n \int_0^{\infty\sqrt{1+i\sigma_\gamma\omega_{i,\nabla B}\xi}} du_{\perp} \mathcal{N}_{u_{\perp}}(0,1)u_{\perp}^{m+1} J_0\left(\sqrt{\hat{b}_i(\xi)}u_{\perp}\right)^2 \quad (\text{A5})$$

where we abbreviated $\hat{b}_i(\xi) = b_i/\sqrt{1+i\sigma_\gamma\omega_{i,\nabla B}\xi}$. As neither the u_{\parallel} nor the u_{\perp} integral contain poles (provided $n > -1$, $m > -2$) or singularities, Cauchy's theorem (applied to a pizza-slice-shaped contour) may be used to exchange the (semi) infinite line integrals in \mathbb{C} with phase $-\pi/4 \leq \arg[\sqrt{1+i\sigma_\gamma\omega_{i,\nabla B}\xi}] \leq \pi/4$, with (semi) infinite line integrals along \mathbb{R} , with the latter reducing to standard Gaussian and Weber integrals for u_{\parallel} and u_{\perp} respectively, yielding the three integrals of interest as

$$\begin{aligned} J_{\parallel,\perp}^{0,0} &= \frac{\omega}{i\sigma_\gamma} \int_0^\infty d\xi \frac{e^{i\sigma_\gamma\omega\xi} \Gamma_0(\hat{b}_i(\xi))}{\sqrt{1+2i\sigma_\gamma\omega_{i,\kappa}\xi} (1+i\sigma_\gamma\omega_{i,\nabla B}\xi)} \\ J_{\parallel,\perp}^{0,2} &= \frac{2\omega}{i\sigma_\gamma} \int_0^\infty d\xi \frac{e^{i\sigma_\gamma\omega\xi} \frac{d}{d\hat{b}_i(\xi)} (\hat{b}_i(\xi) \Gamma_0(\hat{b}_i(\xi)))}{\sqrt{1+2i\sigma_\gamma\omega_{i,\kappa}\xi} (1+i\sigma_\gamma\omega_{i,\nabla B}\xi)^2} \quad (\text{A6}) \\ J_{\parallel,\perp}^{2,0} &= \frac{\omega}{i\sigma_\gamma} \int_0^\infty d\xi \frac{e^{i\sigma_\gamma\omega\xi} \Gamma_0(\hat{b}_i(\xi))}{(1+2i\sigma_\gamma\omega_{i,\kappa}\xi)^{3/2} (1+i\sigma_\gamma\omega_{i,\nabla B}\xi)} \end{aligned}$$

where the Bessel function expression $\Gamma_0(\hat{b}_i) + \hat{b}_i(\Gamma_1(\hat{b}_i) - \Gamma_0(\hat{b}_i))$ has been abbreviated through $d(\Gamma_0(\hat{b}_i)\hat{b}_i)/d\hat{b}_i$.

Combining Eqns. (A2) and (A3) matches with Eqn. (12) from the main text where we have compressed the notation $\{J_{\parallel,\perp}^{0,0}, J_{\parallel,\perp}^{2,0}, J_{\parallel,\perp}^{0,2}\} \rightarrow \{J_{\parallel}^0, J_{\parallel}^2, J_{\perp}^2\}$, whilst Eqn. (A6) matches with Eqn. (A6) under this notation compression.

2. Electron dispersion integral

With the kinetic contribution to the model being dominated by trapping effects, the variation of v_{\parallel}, v_{\perp} along the unperturbed bounce-orbits need be taken into account, hence it is not adequate to consider the velocity-space coordinates as independent. As the modulation of v_{\parallel}, v_{\perp} by the magnetic geometry occurs to (approximately) conserve the magnetic momentum $\mu = mv_{\perp}^2/(2B)$ as a (lowest-order order) adiabatic invariant and is energy conserving¹⁶⁹, we describe the electron velocity-space using energy and pitch angle coordinates $\varepsilon = E/T_e = \|\mathbf{v}\|^2/(2v_{Te}^2)$, $\lambda = \mu/E = v_{\perp}^2/(v_{Te}^2 B)$ such that

$$\mathcal{F}_{Me} d^3\mathbf{v}_e = \sum_{\sigma_{\parallel}=\pm 1} \frac{\exp(-\varepsilon)}{(2\pi)^{3/2}} \frac{B\sqrt{2\varepsilon}}{2\sqrt{1-\lambda B}} d\varepsilon d\lambda d\vartheta \quad (\text{A7})$$

where the spatial variation of $\|\mathbf{B}\|$ has been suppressed, $\sigma_{\parallel} = \text{sgn } v_{\parallel}$ accounts for the direction of the longitudinal motion and the pitch angle $\lambda \in [0, 1/B]$ accounts for the modulation of v_{\parallel}, v_{\perp} across the bounce-orbits, with the boundaries

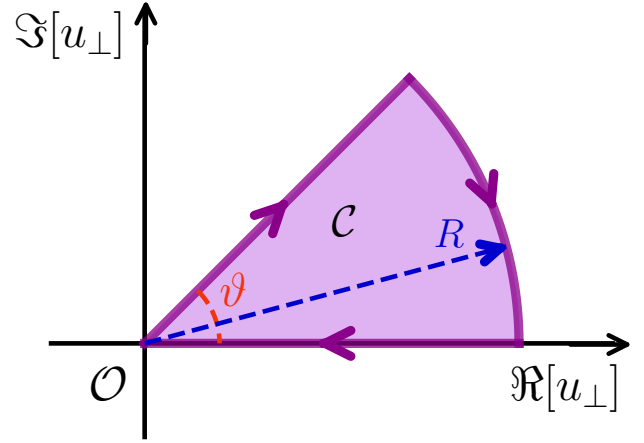


FIG. 8: Sketch of the finite pizza-slice-shaped contour \mathcal{C} , where $\vartheta = \arg[\sqrt{1+i\sigma_\gamma\omega_{i,\nabla B}\xi}]$ shown for a case where $\sigma_\gamma = \text{sgn } \omega_{i,\nabla B} = +1$, arrows indicate direction along which the contour integral $\oint_{\mathcal{C}} du_{\perp}$ is evaluated. Upon taking the limit of $R \rightarrow \infty$, the contribution along the arclength vanishes asymptotically, while the contribution along the inclined segment reduces to the u_{\perp} integral of Eqn. (A6). To perform the u_{\parallel} integral, we consider the contour $\mathcal{C} + \mathcal{C}'$, where \mathcal{C}' is the pizza-slice-shaped contour obtained by reflecting \mathcal{C} through the origin whilst preserving continuity of the integration path.

of pitch angle space corresponding to strongly circulating- and (locally) deflecting trapped-particles, corresponding to the root of $\sqrt{1-\lambda B}$, respectively.

Hence for the electron resonant integral from Eqn. (9) yields

$$\int_{\text{trap}} \frac{\omega - \omega_{*e}^T}{\omega - \omega_{de}} \hat{\phi} \mathcal{F}_{Me} d^3 \mathbf{v}_e = \frac{B}{\sqrt{\pi}} \int_0^{1/B} d\lambda H(\lambda) \frac{\hat{\phi}(\lambda)}{\sqrt{1 - \lambda B}} \left(\Gamma\left(\frac{3}{2}\right) + \underbrace{\int_0^\infty d\varepsilon \sqrt{\varepsilon} e^{-\varepsilon} \frac{\overline{\omega_{de}} - \omega_{*e}^T}{\omega - \overline{\omega_{de}}}}_{I_{\text{tr-el}}} \right) \quad (\text{A8})$$

where $H(\lambda)$ is the Heaviside function to account for the trapped-particle region of velocity space being exclusive to pitch angles $\lambda > 1/B_{\text{max}}$, where B_{max} is the global maximum of the magnetic field strength on the flux surface, the frequency fraction was simplified analogously to the ion case, $\Gamma(z) = \int_0^\infty t^{z-1} e^{-t} dt$ denotes the Euler gamma function, and $\Sigma_{\sigma_{\parallel}=\pm} \rightarrow 2$ as the integrand depends only on $|v_{\parallel}|$. Applying Eqn. (11) to the integral $I_{\text{tr-el}}$ containing the precession drift resonance yields

$$I_{\text{tr-el}} = -\frac{\omega_{\nabla n_e} - \frac{3}{2}\omega_{\nabla T_e}}{\omega} J_{\text{tr-el}}^{(1)} + \frac{\overline{\omega_{de}^T}(\lambda) - \omega_{\nabla T_e}}{\omega} J_{\text{tr-el}}^{(2)} \quad (\text{A9})$$

where the explicit energy dependence of the diamagnetic drift $\omega_{*e}^T = \omega_{\nabla n_e} + \omega_{\nabla T_e}(\varepsilon - 3/2)$ and precession drift $\overline{\omega_{de}} = \varepsilon(2\omega_{e,\kappa}(1 - \lambda B) + \omega_{e,\nabla B}\lambda B) \equiv \varepsilon\overline{\omega_{de}^T}(\lambda)$ where the bounce-averaged quantity conveniently represents the precession drift of a trapped-particle at thermal energy, in terms of the follow-

ing generic integral

$$J_{\text{tr-el}}^m = \frac{\omega}{i\sigma_\gamma} \int_0^\infty d\xi e^{i\sigma_\gamma\omega\xi} \int_0^\infty d\varepsilon \exp(-\varepsilon) \varepsilon^{\frac{2m-1}{2}} e^{-i\sigma_\gamma\varepsilon\overline{\omega_{de}^T}\xi}. \quad (\text{A10})$$

For $m > -1/2$, the energy integral in Eqn. (A10) can be performed analytically, facilitated by the coordinate transform $\varphi = \varepsilon \left(1 + i\sigma_\gamma\overline{\omega_{de}^T}\xi\right)$, which, upon applying Cauchy's theorem to the pizza-slice-shaped contour from Figure 8 to exchange the line integral in \mathbb{C} to a line integral on \mathbb{R} , yields

$$J_{\text{tr-el}}^m = \Gamma\left(\frac{2m+1}{2}\right) \frac{\omega}{i\sigma_\gamma} \int_0^\infty d\xi \frac{e^{i\sigma_\gamma\omega\xi}}{\left(1 + i\sigma_\gamma\overline{\omega_{de}^T}\xi\right)^{\frac{2m+1}{2}}}. \quad (\text{A11})$$

The remaining ξ integral may also be obtained analytically, by applying a coordinate transform to simplify the denominator. This transform, however, needs be carefully considered such that it conserves the absolute convergence properties of Eqns. (A10) and (A11), regardless of parameters for the eigenfrequency or magnetic drift. The appropriate transform with the desired properties of analyticity and absolute convergence may be shown to be $\mu = -i\sigma_\gamma\sigma_{d,e}\sqrt{\omega/\overline{\omega_{de}^T}}\sqrt{1 + i\sigma_\gamma\overline{\omega_{de}^T}\xi}$, where $\sigma_{d,e} = \text{sgn} \overline{\omega_{de}^T}$, reducing the ξ integral from Eqn. (A11) to

$$\frac{J_{\text{tr-el}}^m}{\Gamma\left(\frac{2m+1}{2}\right)} \equiv I^m = (-1)^{m+1} 2i\sigma_\gamma\sigma_{d,e} \left(\frac{\omega}{\overline{\omega_{de}^T}}\right)^{\frac{2m+1}{2}} e^{-\frac{\omega}{\overline{\omega_{de}^T}}} \int_{-i\sigma_\gamma\sigma_{d,e}\sqrt{\frac{\omega}{\overline{\omega_{de}^T}}}}^{\infty \exp\left(i \arg \left[\sqrt{\frac{\omega}{\overline{\omega_{de}^T}}}\right] - i\frac{\pi}{4}\sigma_\gamma\sigma_{d,e}\right)} d\mu \frac{e^{-\mu^2}}{\mu^{2m}}. \quad (\text{A12})$$

Regardless of frequency or precession drift, the phase of the upper bound is constrained to $-\pi/4 \leq \arg \mu \leq \pi/4$, identical to the ion case, such that integrals over the Gaussian are asymptotically vanishing, and by integrating along the shifted and skewed pizza-slice-shaped contour from Figure 9 we may exchange the integral to be performed along the path

$\mu \in \left[-i\sigma_\gamma\sigma_{d,e}\sqrt{\omega/\overline{\omega_{de}^T}}, \infty\right)$. For $m \neq 1/2$, integration by parts leads to the recurrence relation

$$I^m = -\frac{2}{2m-1} \frac{\omega}{\overline{\omega_{de}^T}} (1 - I^{m-1}) \quad (\text{A13})$$

where, for the integrals of interest with $m \in \mathbb{N}$, the generating

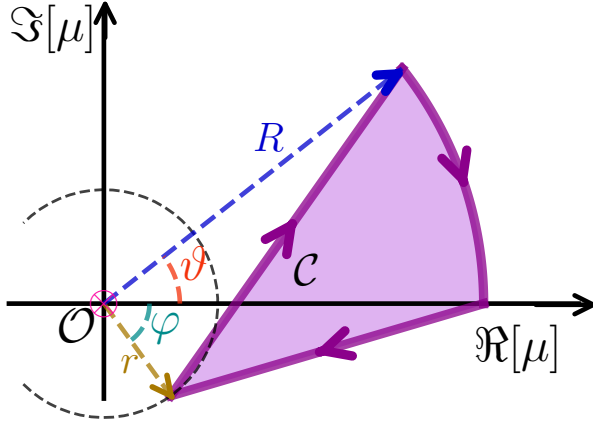


FIG. 9: Sketch of the finite skewed pizza-slice-shaped contour \mathcal{C} , where $\vartheta = \arg \left[\sqrt{\omega/\omega_{de}^T} \right] - \pi\sigma_\gamma\sigma_{d,e}/4$, $\phi = -\arg \left[\sqrt{\omega/\omega_{de}^T} \right] + \pi\sigma_\gamma\sigma_{d,e}/2$ and $r = \left| \sqrt{\omega/\omega_{de}^T} \right|$, shown for a case where $\sigma_\gamma\sigma_{d,e} + 1$. The arrows indicate the direction along which the contour integral $\oint_{\mathcal{C}} d\mu$ is evaluated, and \otimes indicates the (degenerate) pole at the origin from $1/\mu^{2m}$ for $m > 0$. Upon taking the limit of $R \rightarrow \infty$, the contribution along the curved segment vanishes asymptotically, while the straight-line contribution represented by the vector $\mathbf{R} - \mathbf{r}$ reduces to the integral of Eqn. (A12).

integral I^0 of the sequence is found as

$$I^0 = -i\sqrt{\pi}\sigma_\gamma\sigma_{d,e}\sqrt{\frac{\omega}{\omega_{de}^T}}e^{-\frac{\omega}{\omega_{de}^T}}\operatorname{erfc}\left[-i\sigma_\gamma\sigma_{d,e}\sqrt{\frac{\omega}{\omega_{de}^T}}\right] \quad (\text{A14})$$

which can be written succinctly in terms of the Faddeeva function⁸³

$$\mathcal{W}(\zeta) = \exp(-\zeta^2)\operatorname{erfc}[-i\zeta] \quad (\text{A15})$$

as $I^0 = -i\sqrt{\pi}\sigma_\gamma\sigma_{d,e}\sqrt{\omega/\omega_{de}^T}\mathcal{W}\left(\sigma_\gamma\sigma_{d,e}\sqrt{\omega/\omega_{de}^T}\right)$. Using Eqns. (A12) to (A15) then yields the integrals of interest in Eqn. (A9) as

$$\begin{aligned} \frac{J_{\text{tr-el}}^{(1)}}{\Gamma(\frac{3}{2})} &= -2\frac{\omega}{\omega_{de}^T}\left(1 + i\sqrt{\pi}\sigma_\gamma\sigma_{d,e}\sqrt{\frac{\omega}{\omega_{de}^T}}\mathcal{W}\left(\sigma_\gamma\sigma_{d,e}\sqrt{\frac{\omega}{\omega_{de}^T}}\right)\right) \\ \frac{J_{\text{tr-el}}^{(2)}}{\Gamma(\frac{5}{2})} &= -\frac{2}{3}\frac{\omega}{\omega_{de}^T}\left(1 - \frac{J_{\text{tr-el}}^{(1)}}{\Gamma(3/2)}\right). \end{aligned} \quad (\text{A16})$$

Inserting Eqn. (A16) into Eqns. (A8) and (A9) matches with Eqn. (12) in the main text, where the recurrence relation between Gamma functions⁸³ $\Gamma(n+1) = n\Gamma(n)$ and $\Gamma(1/2) = \sqrt{\pi}$ have been used to reduce the prefactors occurring in the pitch-angle integral, the effect of $H(\lambda)$ has been accounted for in the integration boundaries of λ , the integrals I^m have been relabelled as $J_{\text{tr-el}}^m$ for increased consistency in notation with the ion treatment, and the plasma dispersion function $Z(\zeta) = i\sqrt{\pi}\mathcal{W}(\zeta)$ has been favoured over the Faddeeva function for historic reasons.

Appendix B: Derivation of the slab-branch dispersion integral

In the simplified scenario of a uniform and straight magnetic field, the magnetic drift vanishes ($\omega_{ds} \rightarrow 0$). Additionally, since the magnetic geometry does not vary along magnetic field lines, a description of the long-scale parallel mode structure in terms of Fourier modes $\hat{g}_s(l) \sim \exp(ik_{\parallel}l)$ (and analogously for $\hat{\phi}(l)$) is lucid^{33,47}. In this parallel-wavenumber description, a solution to the gyrokinetic Vlasov equation [Eqn. (3)] is readily obtained, and the quasi-neutrality constraint [Eqn. (5)] reduces to

$$\sum_s \frac{q_s^2 n_s}{T_s} \left(1 - \int \frac{\omega - \omega_{*s}^T}{\omega - k_{\parallel}v_{\parallel}} J_0(k_{\perp}\rho_s)^2 \mathcal{F}_{Ms} d^3\mathbf{v}_s\right) = 0. \quad (\text{B1})$$

In order to solve for the kinetic integral appearing in the slab-branch dispersion relation of Eqn. (B1), we proceed analogously to the derivation of the resonant ion integral in the toroidal branch presented in Section A 1. Using normalised cylindrical velocity coordinates the non-adiabatic density fluctuation may be written as

$$\int \frac{\omega - \omega_{*s}^T}{\omega - k_{\parallel}v_{\parallel}} J_0(k_{\perp}\rho_i)^2 \mathcal{F}_{Mi} d^3\mathbf{v}_i = \Gamma_0(b_i) + \underbrace{\sqrt{2\pi} \int_{-\infty}^{\infty} dx_{\parallel} \int_0^{\infty} dx_{\perp} \frac{k_{\parallel}v_{Ts}x_{\parallel} - \omega_{*s}^T}{\omega - k_{\parallel}v_{Ts}x_{\parallel}} \mathcal{N}_{x_{\parallel}}(0,1)\mathcal{N}_{x_{\perp}}(0,1)x_{\perp}J_0(\sqrt{b_i}x_{\perp})^2}_{=I_i^{\text{slab}}}. \quad (\text{B2})$$

As the Landau resonance condition in the integral I_i^{slab} only depends on x_{\parallel} , the perpendicular velocity may be integrated

over analytically making once more use of Weber integrals¹⁰¹, and upon using Eqn. (11) (with $\omega_{ds} \rightarrow k_{\parallel}v_{Ts}$) to write the res-

onant denominators in terms of an auxiliary integral we obtain

$$I_i^{\text{slab}} = - \left[\left(\frac{\omega \nabla n_i - \frac{3}{2} \omega \nabla T_i}{\omega} \right) \Gamma_0(b_i) + \frac{\omega \nabla T_i}{\omega} \frac{d(b_i \Gamma_0(b_i))}{db_i} \right] J_{\parallel}^0 + \frac{k_{\parallel} v_{Ts}}{\omega} \Gamma_0(b_i) J_{\parallel}^1 - \frac{\omega \nabla T_i}{2\omega} \Gamma_0(b_i) J_{\parallel}^2 \quad (\text{B3})$$

having introduced the parametrised integral

$$J_{\parallel}^n = \frac{\omega}{i\sigma_{\gamma}} \int_0^{\infty} d\xi e^{i\sigma_{\gamma}\omega\xi} \int_{-\infty}^{\infty} dx_{\parallel} \mathcal{N}_{x_{\parallel}}(0,1) x_{\parallel}^n e^{-i\sigma_{\gamma}k_{\parallel}v_{Ts}x_{\parallel}\xi}. \quad (\text{B4})$$

hence the velocity integral in Eqn. (B4) can be performed analytically after letting $u_{\parallel} = x_{\parallel} + i\sigma_{\gamma}k_{\parallel}v_{Ts}\xi$, thereby reducing to standard Gaussian moments in u_{\parallel} once integrated along the contour in Figure 8 (extending the shown contour into the fourth quadrant). The three integrals of interest in Eqn. (B3) thus reduce to

$$\begin{aligned} J_{\parallel}^0 &= 2\pi \mathcal{N}_{\omega}(0, k_{\parallel}v_{Ts}) J_{\xi}^0 \\ J_{\parallel}^1 &= -i\sigma_{\gamma}2\pi k_{\parallel}v_{Ts} \mathcal{N}_{\omega}(0, k_{\parallel}v_{Ts}) J_{\xi}^1 \\ J_{\parallel}^2 &= 2\pi \mathcal{N}_{\omega}(0, k_{\parallel}v_{Ts}) \left[J_{\xi}^0 - (k_{\parallel}v_{Ts})^2 J_{\xi}^2 \right] \end{aligned} \quad (\text{B6})$$

where the generic integral

$$J_{\xi}^m = \frac{\omega}{i\sigma_{\gamma}} \int_0^{\infty} d\xi \mathcal{N}_{\xi} \left(\frac{i\sigma_{\gamma}\omega}{k_{\parallel}^2 v_{Ts}^2}, \frac{1}{k_{\parallel}v_{Ts}} \right) \xi^m \quad (\text{B7})$$

has been introduced. Analytical solutions to Eqn. (B7) may be obtained by properly rescaling the normal distribution, however, extra care need be taken that this rescaling does not violate the convergence properties of both Eqns. (B4) and (B7) on the semi-infinite interval. The appropriate transform may be found to be $\eta_{\parallel} = \sigma_{k_{\parallel}} k_{\parallel} v_{Ts} (\xi - i\sigma_{\gamma}\omega/(k_{\parallel}v_{Ts})^2)$, such that Eqn. (B7) maps to

$$J_{\xi}^m = \frac{\omega}{i\sigma_{\gamma}\sigma_{k_{\parallel}}k_{\parallel}v_{Ts}} \int_{-i\sigma_{\gamma}\sigma_{k_{\parallel}}\frac{\omega}{k_{\parallel}v_{Ts}}}^{\infty} d\eta_{\parallel} \mathcal{N}_{\eta_{\parallel}}(0,1) \times \left[\frac{\eta_{\parallel}}{\sigma_{k_{\parallel}}k_{\parallel}v_{Ts}} + i\sigma_{\gamma}\frac{\omega}{(k_{\parallel}v_{Ts})^2} \right]^m.$$

Consequently the problem is reduced to finding the integrals

$$I^m = \int_{-i\sigma_{\gamma}\sigma_{k_{\parallel}}\frac{\omega}{k_{\parallel}v_{Ts}}}^{\infty} d\eta_{\parallel} \mathcal{N}_{\eta_{\parallel}}(0,1) \eta_{\parallel}^m$$

We note that in case of $\gamma/k_{\parallel} > 0$, Eqn. (B4) may straightforwardly be expressed in terms of plasma dispersion functions through Eqn. (16) if the resonant denominator is reintroduced by exchanging the order of integration between ξ and x_{\parallel} , i.e. by reverting Eqn. (11). However, in order to obtain generally valid results (lest $\gamma = 0 \vee k_{\parallel} = 0$), we proceed with Eqn. (B4) in its current form. Unlike the toroidal-resonance scenario, where the Landau resonance for curvature drive depends on x_{\parallel}^2 , the slab branch resonance depends linearly on x_{\parallel} , hence the exponential factor $e^{-i\sigma_{\gamma}k_{\parallel}v_{Ts}x_{\parallel}\xi}$ cannot be consolidated into a re-scaled normal distribution for just x_{\parallel} . Instead using Eqn. (A1), it can be shown that

$$e^{i\sigma_{\gamma}\omega\xi} \mathcal{N}_{x_{\parallel}}(0,1) e^{-i\sigma_{\gamma}k_{\parallel}v_{Ts}x_{\parallel}\xi} = 2\pi \mathcal{N}_{x_{\parallel}}(-i\sigma_{\gamma}k_{\parallel}v_{Ts}\xi, 1) \mathcal{N}_{\xi} \left(\frac{i\sigma_{\gamma}\omega}{k_{\parallel}^2 v_{Ts}^2}, \frac{1}{k_{\parallel}v_{Ts}} \right) \mathcal{N}_{\omega}(0, k_{\parallel}v_{Ts}) \quad (\text{B5})$$

which through integration by parts for $m > 0$ may be shown that satisfy the recurrence relation

$$I^m = \frac{e^{\frac{\omega^2}{2(k_{\parallel}v_{Ts})^2}}}{\sqrt{2\pi}} \left(-i\sigma_{\gamma}\sigma_{k_{\parallel}} \frac{\omega}{k_{\parallel}v_{Ts}} \right)^{m-1} + (m-1)I^{m-2} \quad (\text{B8})$$

while $I^0 = \text{erfc} \left[-i\sigma_{\gamma}\sigma_{k_{\parallel}} \frac{\omega}{\sqrt{2}k_{\parallel}v_{Ts}} \right] / 2$ is directly yielded in terms of the complementary error function. Combining Eqns. (B6) to (B8) then yields after a little bookkeeping the resonant slab integrals as

$$\begin{aligned} J_{\parallel}^0 &= -i\sqrt{\pi}\sigma_{\gamma}\sigma_{k_{\parallel}} \frac{\omega}{k_{\parallel}v_{Ts}\sqrt{2}} \mathcal{W} \left(\sigma_{\gamma}\sigma_{k_{\parallel}} \frac{\omega}{k_{\parallel}v_{Ts}\sqrt{2}} \right) \\ J_{\parallel}^1 &= \frac{\omega}{k_{\parallel}v_{Ts}} (J_{\parallel}^0 - 1) \\ J_{\parallel}^2 &= \frac{\omega^2}{(k_{\parallel}v_{Ts})^2} (J_{\parallel}^0 - 1) \end{aligned} \quad (\text{B9})$$

where akin to the trapped-electron treatment from Section A 2, the Faddeeva function Eqn. (A15) has been introduced. Substituting Eqn. (B9) into Eqns. (B1) to (B3) then yields the dispersion relation for slab-ITG modes which is generally valid unless $\gamma = 0 \vee k_{\parallel} = 0$.

$$\begin{aligned} 1 + \sum_j Z_j^2 \frac{n_j T_e}{n_e T_j} \left[1 - \Gamma_0(b_j) \left(\left[\frac{\omega \nabla n_j}{\omega} - 1 \right] \xi_{j,\parallel} Z(\xi_{j,\parallel}) \right. \right. \\ \left. \left. + \frac{\omega \nabla T_j}{\omega} \left[\xi_{j,\parallel} Z(\xi_{j,\parallel}) \left(\xi_{j,\parallel}^2 - \frac{1}{2} \right) + \xi_{j,\parallel}^2 \right] \right) \right. \\ \left. - \frac{\omega \nabla T_j}{\omega} \xi_{j,\parallel} Z(\xi_{j,\parallel}) b_j (\Gamma_1(b_j) - \Gamma_0(b_j)) \right] = 0 \end{aligned} \quad (\text{B10})$$

where the plasma dispersion function $Z(\xi) = i\sqrt{\pi}\mathcal{W}(\xi)$ has been introduced in favour of the Faddeeva function to match

with typical conventions, the contribution from the kinetic electrons has been neglected since it is smaller by a factor of $\sqrt{m_e/m_i}$ than that from the ions (see below), and $\xi_{j,\parallel} = \sigma_\gamma \sigma_{k_\parallel} \omega / (k_\parallel v_{Tj} \sqrt{2})$ with $\sigma_{k_\parallel} = \text{sgn } k_\parallel$. The fact that the sign of the parallel wavenumber k_\parallel , which effectively determines the mode structure along the field line, should be considered to determine the proper validity regime beyond which analytical continuation is required for the plasma dispersion function as expressed through Eqn. (16) has also been considered in e.g. Ref. 170. In the usual limit of a pure hydrogen plasma, Eqn. (B10) reduces to the well-known result by Kadomtsev & Pogutse⁵¹ for $\sigma_{k_\parallel} = \sigma_\gamma = +1$.

Asymptotic forms

The slab-branch dispersion derivation made no assumptions with regard to parameter values, and is thus valid for all species, including electrons. Although trapping effects vanish in the homogeneous plasma slab limit, the non-adiabatic electron response does not, and from Eqn. (3) with an eigenmode ansatz of $\hat{g}_s(l) \sim \exp(ik_\parallel l)$, it follows the electron- and ion non-adiabatic distribution function are identical under exchange of subscripts $i \rightarrow e$. What remains identical to the toroidal branch, however, is the timescale separation between ion- and electron motion along the field line since $v_{Ti}/v_{Te} \ll 1$. Hence, depending on the assumption of the eigenfrequency ω we could be in different regimes.

If we assume $\omega/(k_\parallel v_{Ti}) \sim \mathcal{O}(1)$, the ions will be strongly in resonance and we have the slab-ITG branch. In this case the argument of the Faddeeva function in Eqn. (B9) is ostensibly small and an expansion of Eqn. (A15) for $\zeta \ll 1$ is warranted, resulting in⁸³

$$J_\parallel^0 = -i\sqrt{\pi} \sigma_\gamma \sigma_{k_\parallel} \frac{\omega}{k_\parallel v_{Te} \sqrt{2}} \sum_{n=0}^{\infty} \frac{\left(i\sigma_\gamma \sigma_{k_\parallel} \frac{\omega}{k_\parallel v_{Te} \sqrt{2}} \right)^n}{\Gamma\left(\frac{n}{2} + 1\right)}. \quad (\text{B11})$$

If additionally we assume that the spatial extent of the mode to be $b_i \sim \mathcal{O}(1)$, then the Bessel function argument $b_e = b_i Z_i T_e m_e / (T_i m_i) \ll 1$, and the effect of FLR damping on the electrons can be neglected. Inserting Eqn. (B11) into Eqns. (B2), (B3) and (B8), then yields to lowest order in v_{Ti}/v_{Te} to a kinetic-electron density fluctuation of

$$\int \frac{\omega - \omega_{*e}^T}{\omega - k_\parallel v_\parallel} \mathcal{F}_{Me} d^3 \mathbf{v}_e \approx -i\sqrt{\pi} \sqrt{\frac{T_i m_e}{T_e m_i}} \frac{\omega}{k_\parallel v_{Ti} \sqrt{2}} \times \left(1 - \frac{\omega \nabla n_e}{\omega} + \frac{\omega \nabla T_e}{2\omega} \right) \quad (\text{B12})$$

which is $\mathcal{O}(\sqrt{m_e/m_i})$ smaller than the kinetic-ion density fluctuation and the adiabatic electron response, and has therefore been neglected in Eqn. (B10).

If by contrast we assume $\omega/(k_\parallel v_{Te}) \sim \mathcal{O}(1)$, the electrons will strongly resonate with the mode and we have the slab-ETG branch. For the ions, the argument of the Faddeeva function will be large and instead an asymptotic expansion

of Eqn. (A15) for $\zeta \gg 1$ can be made, resulting in⁸³

$$J_\parallel^0 \sim \sum_{m=0}^{\infty} \frac{(2m)!}{m! 2^m} \left(\frac{k_\parallel v_{Ti}}{\omega} \right)^{2m}, \quad (\text{B13})$$

which inserted into Eqns. (B2), (B3) and (B8) gives the kinetic-ion density fluctuation to lowest order in v_{Ti}/v_{Te} as

$$\int \frac{\omega - \omega_{*i}^T}{\omega - k_\parallel v_\parallel} J_0(k_\perp \rho_i)^2 \mathcal{F}_{Mi} d^3 \mathbf{v}_i \approx \Gamma_0(b_i) \left(1 - \frac{\omega \nabla n_i}{\omega} \right) - \frac{\omega \nabla T_i}{\omega} b_i \frac{d\Gamma_0(b_i)}{db_i}. \quad (\text{B14})$$

In obtaining Eqn. (B13) we made use of the asymptotic expansion for the complementary error function $\text{erfc}(z)$, whose validity is restricted to $|\arg z| < 3\pi/4$. In our case as $z = -i\sigma_\gamma \sigma_{k_\parallel} \frac{\omega}{k_\parallel v_{Ti}}$, by virtue of the sign generalisation, $|\arg z| < \pi/2$, such that this expansion is always lucid except for $k_\parallel = 0 \vee \gamma = 0$.

Appendix C: Derivation of reduced-fidelity models

1. Padé approximation to FLR effects

Applying the Padé approximation of $\Gamma_0(\hat{b}_j) \approx 1/(1 + \hat{b}_j)$ to the integrals of Eqn. (14) yields

$$\begin{aligned} J_j^{\text{Padé},0} &= \frac{\omega}{i\sigma_\gamma} \int_0^\infty d\xi \frac{\exp(i\sigma_\gamma \omega \xi)}{\sqrt{1 + 2i\sigma_\gamma \omega_j \kappa \xi} (1 + b_j + i\sigma_\gamma \omega_j \nabla_B \xi)} \\ J_{j,\perp}^{\text{Padé},2} &= \frac{2\omega}{i\sigma_\gamma} \int_0^\infty d\xi \frac{\exp(i\sigma_\gamma \omega \xi)}{\sqrt{1 + 2i\sigma_\gamma \omega_j \kappa \xi} (1 + b_j + i\sigma_\gamma \omega_j \nabla_B \xi)^2} \\ J_{j,\parallel}^{\text{Padé},2} &= \frac{\omega}{i\sigma_\gamma} \int_0^\infty d\xi \frac{\exp(i\sigma_\gamma \omega \xi)}{(1 + 2i\sigma_\gamma \omega_j \kappa \xi)^{3/2} (1 + b_j + i\sigma_\gamma \omega_j \nabla_B \xi)} \end{aligned} \quad (\text{C1})$$

where in $J_{j,\perp}^{(2)}$ we applied the Padé approximation for Γ_0 before evaluating its derivative. Akin to the treatment from Ref. 43, we consider generalised parametrised versions of these integrals

$$\begin{aligned} J_j^{0,v,\lambda} &= \frac{\omega}{i\sigma_\gamma} \int_0^\infty d\xi \frac{\exp(i\sigma_\gamma \omega \xi)}{\sqrt{v + 2i\sigma_\gamma \omega_j \kappa \xi} (\lambda + i\sigma_\gamma \omega_j \nabla_B \xi)} \\ J_{j,\perp}^{2,v,\lambda} &= \frac{2\omega}{i\sigma_\gamma} \int_0^\infty d\xi \frac{\exp(i\sigma_\gamma \omega \xi)}{\sqrt{v + 2i\sigma_\gamma \omega_j \kappa \xi} (\lambda + i\sigma_\gamma \omega_j \nabla_B \xi)^2} \\ &= -2 \frac{d}{d\lambda} J_j^{0,v,\lambda} \\ J_{j,\parallel}^{2,v,\lambda} &= \frac{\omega}{i\sigma_\gamma} \int_0^\infty d\xi \frac{\exp(i\sigma_\gamma \omega \xi)}{(v + 2i\sigma_\gamma \omega_j \kappa \xi)^{3/2} (\lambda + i\sigma_\gamma \omega_j \nabla_B \xi)} \\ &= -2 \frac{d}{dv} J_j^{0,v,\lambda} \end{aligned} \quad (\text{C2})$$

such that Eqn. (C1) is recovered in the limits $v \rightarrow 1, \lambda \rightarrow 1 + b_j$, and the problem is in principle reduced to finding a solution of $J_j^{0,v,\lambda}$, with the remaining integrals being obtained as derivatives, much like the BDR treatment of the drift-kinetic case⁴⁴.

As the curvature-related term is similar to the precession-resonance appearing in the TEM approach Eqn. (A10), we make a similar coordinate transform $\eta_\kappa = -i\sigma_\gamma\sigma_\kappa\sqrt{\omega/(2\omega_{j,\kappa})}\sqrt{v+2i\sigma_\gamma\omega_{j,\kappa}\xi}$, with $\sigma_\kappa = \text{sgn } \omega_{j,\kappa}$, yielding

$$J_j^{0,v,\lambda} = -2i\sigma_\gamma\sigma_\kappa \frac{\omega}{\omega_{j,\nabla B}} \sqrt{\frac{\omega}{2\omega_{j,\kappa}}} e^{-\frac{v\omega}{2\omega_{j,\kappa}}} \int_{-i\sigma_\gamma\sigma_\kappa\sqrt{\frac{v\omega}{2\omega_{j,\kappa}}}}^{\infty \exp\left(i\left(\arg\left[\sqrt{\frac{v\omega}{2\omega_{j,\kappa}}}\right] - \frac{\pi}{4}\sigma_\gamma\sigma_\kappa\right)\right)} \frac{e^{-\eta_\kappa^2}}{\left(\lambda \frac{\omega_{j,\kappa}}{\omega_{j,\nabla B}} - \frac{v}{2}\right) \frac{\omega}{\omega_{j,\kappa}} - \eta_\kappa^2}. \quad (\text{C2})$$

By taking the v and λ derivatives of Eqn. (C3), we arrive at the following interrelation between the three integrals from Eqn. (C2)

$$J_{j,\parallel}^{2,v,\lambda} = \frac{\omega}{\omega_{j,\kappa}} \left(J_j^{0,v,\lambda} - \frac{1}{\lambda\sqrt{v}} \right) - \frac{\omega_{j,\nabla B}}{2\omega_{j,\kappa}} J_{j,\perp}^{2,v,\lambda}, \quad (\text{C4})$$

thus making one of the integrals redundant. For our purpose, we choose this redundant integral to be $J_{j,\perp}^{2,v,\lambda}$, and proceed to find an alternative expression for $J_{j,\parallel}^{2,v,\lambda}$. Returning to the original expressions from Eqn. (C2), and performing partial fraction decomposition on the denominators of $J_j^{0,v,\lambda}$, $J_{j,\perp}^{2,v,\lambda}$, we find that

$$J_{j,\parallel}^{2,v,\lambda} = B(v,\lambda)J_j^{0,v,\lambda} + A(v,\lambda) \frac{\omega}{i\sigma_\gamma} \int_0^\infty d\xi \frac{e^{i\sigma_\gamma\omega\xi}}{(v+2i\sigma_\gamma\omega_{j,\kappa}\xi)^{3/2}} \quad (\text{C5})$$

where $A(v,\lambda) = (\omega_{j,\kappa}/\omega_{j,\nabla B})/(\lambda\omega_{j,\kappa}/\omega_{j,\nabla B} - v/2)$ and $B(v,\lambda) = -(\lambda\omega_{j,\kappa}/\omega_{j,\nabla B} - v/2)^{-1}/2$ are the expansion coefficients occurring in partial fraction decomposition of $J_j^{0,v,\lambda}$. The remaining integral over the curvature resonance in Eqn. (C5) is equivalent to the precession resonance integral Eqn. (A10) (for $m=1$) under the substitutions $\omega_{j,\kappa} \rightarrow \overline{\omega_{de}^T}/2$ and $v \rightarrow 1$, and thus by employing the coordinate transform $\eta_\kappa = -i\sigma_\gamma\sigma_\kappa\sqrt{\omega/(2\omega_{j,\kappa})}\sqrt{v+2i\sigma_\gamma\omega_{j,\kappa}\xi}$, may be similarly simplified into Eqn. (A12) with the substitutions of $\mu \rightarrow \eta_\kappa$ and $\omega/\overline{\omega_{de}^T} \rightarrow \omega v/2\omega_{j,\kappa}$ in the integral bounds and exponential. It is readily verified, using the same methods as outlined in Section A 2, that these changes slightly modify the

recurrence relation (Eqn. (A13)) and generating function I^0 (Eqn. (A14)) to $I^m = -\omega/((2m-1)\omega_{j,\kappa})(1/v^{m-1/2} - I^{m-1})$ and $I^0 = -i\sqrt{\pi}\sigma_\gamma\sigma_\kappa\sqrt{\omega/(2\omega_{j,\kappa})}\mathcal{W}(\sigma_\gamma\sigma_\kappa\sqrt{\omega v/(2\omega_{j,\kappa})})$ respectively. Applying to the case $m=1$ then gives

$$J_{j,\parallel}^{2,v,\lambda} = -\frac{1}{2\lambda \frac{\omega_{j,\kappa}}{\omega_{j,\nabla B}} - v} J_j^{0,v,\lambda} - \frac{1}{\lambda \frac{\omega_{j,\kappa}}{\omega_{j,\nabla B}} - \frac{v}{2}} \frac{\omega}{\omega_{j,\nabla B}} \times \left[\frac{1}{\sqrt{v}} + i\sqrt{\pi}\sigma_\gamma\sigma_\kappa\sqrt{\frac{\omega}{2\omega_{j,\kappa}}}\mathcal{W}\left(\sigma_\gamma\sigma_\kappa\sqrt{\frac{v\omega}{2\omega_{j,\kappa}}}\right) \right], \quad (\text{C6})$$

thereby rendering $J_j^{0,v,\lambda}$ the last remaining unknown integral.

Returning to Eqn. (C3), the upper-bound of the integral may be reduced from complex infinity to $+\infty$ by realising that for all cases of interest $v > 0$, and the upper-bound is constraint to lie in the region $|\arg \eta_\kappa| < \pi/4$ in which the Gaussian asymptotically vanishes as $|\eta_\kappa| \rightarrow \infty$, and we integrate Eqn. (C3) along the shifted and skewed pizza-slice-shaped-contour from Figure 9, under the mappings of $(\mu, \omega/\overline{\omega_{de}^T}, \sigma_{d,e}) \rightarrow (\eta_\kappa, \omega v/(2\omega_{j,\kappa}), \sigma_\kappa)$. The poles at $\eta_\kappa = \pm \sqrt{\left(\lambda \frac{\omega_{j,\kappa}}{\omega_{j,\nabla B}} - \frac{v}{2}\right) \frac{\omega}{\omega_{j,\kappa}}}$ (not shown in Figure 9) can be shown to lie outside of the contour whenever $\lambda\omega_{j,\kappa}/v\omega_{j,\nabla B} > 0$ is satisfied, or as both $v, \lambda \in \mathbb{R}^+$ for the application of interest to Eqn. (C1), this requires only that $\omega_{j,\kappa}/\omega_{j,\nabla B} > 0$, which is the typical case for low β plasmas¹⁷¹. Under the assumption that $\lambda\omega_{j,\kappa}/v\omega_{j,\nabla B} > 0$, it follows that along the full integration of $\eta \in [-i\sigma_\gamma\sigma_\kappa\sqrt{v\omega/2\omega_{j,\kappa}}, \infty)$ we have that the $\text{sgn Im}[(\lambda\omega_{j,\kappa}/\omega_{j,\nabla B} - v/2)\omega/\omega_{j,\kappa} - \eta_\kappa^2] = \sigma_\gamma\sigma_\kappa$, and hence by writing $1/z = (1/i\text{sgn}\{\text{Im}[z]\}) \int_0^\infty d\xi e^{i\text{sgn}\{\text{Im}[z]\}z\xi}$, similar to how Eqn. (11) has been applied to the resonant denominator in the dispersion relation, we obtain

$$J_j^{0,v,\lambda} = -2\sqrt{\frac{\omega}{2\omega_{j,\kappa}}} e^{-\frac{v\omega}{2\omega_{j,\kappa}}} \frac{\omega}{\omega_{j,\nabla B}} \int_0^\infty d\xi e^{i\sigma_\gamma\sigma_\kappa\left(\lambda \frac{\omega_{j,\kappa}}{\omega_{j,\nabla B}} - \frac{v}{2}\right) \frac{\omega}{\omega_{j,\kappa}} \xi} \int_{-i\sigma_\gamma\sigma_\kappa\sqrt{\frac{v\omega}{2\omega_{j,\kappa}}}}^\infty d\eta_\kappa e^{-\eta_\kappa^2(1+i\sigma_\gamma\sigma_\kappa\xi)}. \quad (\text{C7})$$

We proceed by performing two consecutive co-

ordinate substitutions; $u = \eta_\kappa\sqrt{1+i\sigma_\gamma\sigma_\kappa\xi}$ and

$p = -i\sigma_\gamma\sigma_\kappa\sqrt{1+i\sigma_\gamma\sigma_\kappa\xi}\sqrt{\omega/2\omega_{j,\kappa}}\sqrt{2\lambda\omega_{j,\kappa}/\omega_{j,\nabla B}-v}$, similar to how Eqns. (A4) and (A10) were simplified into

Gaussian integrals for the toroidal ion- and trapped-electron resonances respectively, yielding

$$J_j^{0,v,\lambda} = -2\sqrt{\pi}e^{-\lambda\frac{\omega}{\omega_{j,\nabla B}}} \frac{\omega}{\omega_{j,\nabla B}\sqrt{2\lambda\frac{\omega_{j,\kappa}}{\omega_{j,\nabla B}}-v}} \int_{-i\sigma_\gamma\sigma_\kappa\sqrt{\frac{\omega}{2\omega_{j,\kappa}}}\sqrt{2\lambda\frac{\omega_{j,\kappa}}{\omega_{j,\nabla B}}-v}}^{\infty} dp e^{-p^2} \operatorname{erfc} \left[\frac{p}{\sqrt{2\frac{\lambda\omega_{j,\kappa}}{v\omega_{j,\nabla B}}-1}} \right] \quad (C8)$$

where after each coordinate transform, we performed integration along the shifted and skewed pizza-slice-shaped contour Figure 9 effectively allowing an exchange of the integral upper-bound from complex infinity (as by virtue of the sign inclusions in the transformations, the upper-bounds for

both variables are constraint to $|\arg\{u, p\}| < \pi/4$ to $+\infty$, and the u integral has been succinctly written as an error function. The integral appearing Eqn. (C8) may then finally be solved in terms of elementary integrals, by writing $\operatorname{erfc} z = 1 - \operatorname{erf} z$, we obtain

$$\int_{p_0}^{\infty} dp e^{-p^2} \operatorname{erfc} \left[\frac{p}{\sqrt{2\frac{\lambda\omega_{j,\kappa}}{v\omega_{j,\nabla B}}-1}} \right] = \frac{\sqrt{\pi}}{2} \operatorname{erfc}[p_0] + 2\sqrt{\pi} \int_{p_0\sqrt{2}}^{\infty} d\chi \frac{\partial}{\partial\chi} T \left[\chi, \frac{1}{\sqrt{2\frac{\lambda\omega_{j,\kappa}}{v\omega_{j,\nabla B}}-1}} \right] \quad (C9)$$

where we introduced the short-hand notation $p_0 = -i\sigma_\gamma\sigma_\kappa\sqrt{\frac{\omega}{2\omega_{j,\kappa}}}\sqrt{2\lambda\frac{\omega_{j,\kappa}}{\omega_{j,\nabla B}}-v}$, rescaled the second integration variable $\chi = p\sqrt{2}$, and introduced the Owen's T-function¹⁵⁵

$$T[z, a] = \frac{1}{2\pi} \int_0^a dt \frac{e^{-z^2(1+t^2)}}{1+t^2}. \quad (C10)$$

Evaluating the χ integral using the Fundamental Theorem of Calculus, then, at last, yields the admittedly wielding expression

$$J_j^{0,v,\lambda} = - \frac{\pi\omega}{\omega_{j,\nabla B}\sqrt{2\lambda\frac{\omega_{j,\kappa}}{\omega_{j,\nabla B}}-v}} \left(e^{-\frac{v\omega}{2\omega_{j,\kappa}}} \times \mathcal{W} \left[\sigma_\gamma\sigma_\kappa\sqrt{\frac{\omega}{2\omega_{j,\kappa}}}\sqrt{2\lambda\frac{\omega_{j,\kappa}}{\omega_{j,\nabla B}}-v} \right] - 4e^{-\frac{\lambda\omega}{\omega_{j,\nabla B}}} \times T \left[-i\sigma_\gamma\sigma_\kappa\sqrt{\frac{\omega}{\omega_{j,\kappa}}}\sqrt{2\lambda\frac{\omega_{j,\kappa}}{\omega_{j,\nabla B}}-v}, \frac{1}{\sqrt{2\frac{\lambda\omega_{j,\kappa}}{v\omega_{j,\nabla B}}-1}} \right] \right) \quad (C11)$$

where we have used that $\lim_{z \rightarrow \infty} T[z, a] \rightarrow 0$ provided that $a \in \mathbb{R}$, as is the case under our assumption of $\lambda\omega_{j,\kappa}/v\omega_{j,\nabla B} > 0$, and favoured the introduction of the Faddeeva function Eqn. (A15) over the error function. Upon setting $v = 1$ and $\lambda = 1 + b_j$ such that we recover Eqn. (C1) from Eqn. (C2), we

note that Eqns. (C4), (C5) and (C11) reduce to Eqn. (28) from the main text where the plasma dispersion function $Z(\zeta) = i\sqrt{\pi}\mathcal{W}(\zeta)$ was written in favour of the Faddeeva function.

2. Zero- β drift-kinetic limit

The drift-kinetic limit is straightforwardly obtained from Eqn. (28) by letting $b_j \rightarrow 0$. Alas, aside from simplifying $g_{\kappa,\nabla B,b}$ and the exponential multiplying the Owen's T-function, this does not yield further analytical reduction in simpler functions. However, upon further letting $\omega_{j,\kappa} \approx \omega_{j,\nabla B}$, equivalent to $\beta \approx 0$, a significant simplification for J^0 can be achieved as $g_{\kappa,\nabla B,b}$ further reduces to unity in that limit, yielding

$$\lim_{b_j \rightarrow 0} \lim_{\beta \rightarrow 0} J_j^{\text{Padé},0} = \frac{\omega}{\omega_{j,\kappa}} \left(i\sqrt{\pi}e^{-\frac{\omega}{2\omega_{j,\kappa}}} Z \left[\sigma_\gamma\sigma_\kappa\sqrt{\frac{\omega}{2\omega_{j,\kappa}}} \right] + 4\pi e^{-\frac{\omega}{\omega_{j,\kappa}}} T \left[-i\sigma_\gamma\sigma_\kappa\sqrt{\frac{\omega}{\omega_{j,\kappa}}}, 1 \right] \right). \quad (C12)$$

To obtain the Owen's-T function with unit upper bound, we rewrite Eqn. (C10) as

$$T[z, a] = \frac{e^{-z^2}}{2\pi} \int_0^\infty d\xi e^{-\xi} \int_0^a dt e^{-(\xi + \frac{z^2}{2})t^2} \quad (C13)$$

where the denominator has been written as an exponential integral $1/\alpha = \int_0^\infty dx e^{-\alpha x}$, ($\text{Re}\{\alpha\} > 0$), where for $a \in \mathbb{R}$ we have that $1 + t^2 \in \mathbb{R}^+$ along the full integration domain. To further simplify Eqn. (C13) we perform the successive change of variables $u = t\sqrt{\xi + z^2/2}$ and $\mu = \sqrt{\xi + z^2/2}$ such that $T[z, a] = \frac{1}{2\sqrt{\pi}} \int_{\sqrt{z^2/2}}^\infty d\mu e^{-\mu^2} \text{erfc}(a\mu)$. As a special case, $T[z, 1]$ is then straightforwardly obtained from integration by parts as $T[z, 1] = (1 - \text{erfc}[\sqrt{z^2/2}])/8 = \text{erfc}[\sqrt{z^2/2}](2 - \text{erfc}[\sqrt{z^2/2}])/8$, which when substituted back into Eqn. (C12) yields

$$\begin{aligned} \lim_{b_j \rightarrow 0} \lim_{\beta \rightarrow 0} J_j^{\text{Padé},0} &= -\frac{\pi}{2} \frac{\omega}{\omega_{j,\kappa}} e^{-\frac{\omega}{\omega_{j,\kappa}}} \text{erfc} \left[-i\sigma_\gamma \sigma_\kappa \sqrt{\frac{\omega}{2\omega_{j,\kappa}}} \right]^2 \\ &= -\frac{\pi}{2} \frac{\omega}{\omega_{j,\kappa}} \mathcal{W} \left[\sigma_\gamma \sigma_\kappa \sqrt{\frac{\omega}{2\omega_{j,\kappa}}} \right]^2 \end{aligned} \quad (\text{C14})$$

where we used that $\sqrt{z^2/2} \rightarrow z/\sqrt{2}$ when $|\arg z| \leq \pi/2$, which is always the case for $z = -i\sigma_\gamma \sigma_\kappa \sqrt{\omega/\omega_{j,\kappa}}$ unless the growth rate or curvature vanishes. Iterating Eqn. (C14) through Eqns. (C4) and (C6) and setting $v = 1, \lambda = 1, \omega_{j,\kappa} = \omega_{j,\nabla B}$ to obtain the $\beta \approx 0$ drift-kinetic limits for $J_{j,\parallel}^{(2)}, J_{j,\perp}^{(2)}$, and substituting the result into Eqn. (18) then yields after some rearranging

$$\begin{aligned} \lim_{\beta \rightarrow 0} \lim_{b \rightarrow 0} h_{\text{ion},j} &\rightarrow \frac{\omega}{2\omega_{j,\kappa}} \left(1 - \frac{\omega_{\nabla n_j}}{\omega} \right) Z^2 \left(\sigma_\gamma \sigma_\kappa \sqrt{\frac{\omega}{2\omega_{j,\kappa}}} \right) \\ &+ \frac{\omega_{\nabla T_j}}{\omega} \left(Z^2 \left(\sigma_\gamma \sigma_\kappa \sqrt{\frac{\omega}{2\omega_{j,\kappa}}} \right) \frac{\omega}{2\omega_{j,\kappa}} \left(1 - \frac{\omega}{\omega_{j,\kappa}} \right) \right. \\ &\left. - \sigma_\gamma \sigma_\kappa \sqrt{\frac{\omega}{2\omega_{j,\kappa}}} \frac{\omega}{\omega_{j,\kappa}} Z \left(\sigma_\gamma \sigma_\kappa \sqrt{\frac{\omega}{2\omega_{j,\kappa}}} \right) \right) \end{aligned} \quad (\text{C15})$$

which agrees with Eqn (3) of Ref. 44 and Eqn (2.5) of Ref. 43 when considering $\sigma_\gamma = \sigma_\kappa = +1$.

3. Curvature model

We straightforwardly obtain the curvature-model from Eqn. (14) by the substitutions of $\omega_{j,\nabla B} \rightarrow 0$ and $\omega_{j,\kappa} \rightarrow \omega_{j,\nabla B} + \omega_{j,\kappa}$, yielding

$$\begin{aligned} J_j^{\text{curv},0} &= \Gamma_0(b_j) \frac{\omega}{i\sigma_\gamma} \int_0^\infty \frac{e^{i\sigma_\gamma \omega \xi}}{\sqrt{1 + 2i\sigma_\gamma \omega_{j,\kappa}^{\text{eff}} \xi}} \\ J_{j,\perp}^{\text{curv},2} &= 2 \frac{d(b_j \Gamma_0(b_j))}{db_j} \frac{\omega}{i\sigma_\gamma} \int_0^\infty \frac{e^{i\sigma_\gamma \omega \xi}}{\sqrt{1 + 2i\sigma_\gamma \omega_{j,\kappa}^{\text{eff}} \xi}} \\ J_{j,\parallel}^{\text{curv},2} &= \Gamma_0(b_j) \frac{\omega}{i\sigma_\gamma} \int_0^\infty \frac{e^{i\sigma_\gamma \omega \xi}}{(1 + 2i\sigma_\gamma \omega_{j,\kappa}^{\text{eff}} \xi)^{3/2}} \end{aligned} \quad (\text{C16})$$

where we have $\hat{b}_j(\xi) = b_j/(1 + i\sigma_\gamma \omega_{j,\nabla B} \xi) \rightarrow b_j$ under these substitutions and introduced $\omega_{j,\kappa}^{\text{eff}} = \omega_{j,\kappa} + \omega_{j,\nabla B}$ as a shorthand notation. Note that within the curvature model there are

only two unique resonant integrals to compute, as $J_{j,\perp}^{\text{curv},2}$ can be obtained from $J_j^{\text{curv},0}$ through simple rescaling by the appropriate Bessel functions. The remaining integrals over ξ for $J_j^{\text{curv},0}, J_{j,2}^{\text{curv},\parallel}$ are identical to those encountered in the derivation of the TEM resonance Eqn. (A10) (for $m = 0, 1$) under the mapping $\bar{\omega}_{de}^T \rightarrow 2\omega_{j,\kappa}^{\text{eff}}$, such that applying this mapping to the generating function Eqn. (A14) and the recurrence relation Eqn. (A13) yields

$$\begin{aligned} J_j^{\text{curv},0} &= -\Gamma_0(b_j) i\sqrt{\pi} \sigma_\gamma \sigma_\kappa^{\text{eff}} \sqrt{\frac{\omega}{2\omega_{j,\kappa}^{\text{eff}}}} \mathcal{W} \left(\sigma_\gamma \sigma_\kappa^{\text{eff}} \sqrt{\frac{\omega}{2\omega_{j,\kappa}^{\text{eff}}}} \right) \\ J_{j,\perp}^{\text{curv},2} &= 2 \left(1 + b_j \left(\frac{I_1(b_j)}{I_0(b_j)} - 1 \right) \right) J_j^{\text{curv},0} \\ J_{j,\parallel}^{\text{curv},2} &= -\frac{\omega}{\omega_{j,\kappa}^{\text{eff}}} \left(\Gamma_0(b_j) - J_j^{\text{curv},0} \right) \end{aligned} \quad (\text{C17})$$

where the derivative of the Bessel function in $J_{j,\perp}^{\text{curv},2}$ has been expanded, and we introduced $\sigma_\kappa^{\text{eff}} = \text{sgn} \omega_{j,\kappa}^{\text{eff}}$. Substituting Eqn. (C17) into Eqn. (18) and applying $\omega_{j,\nabla B} \rightarrow 0, \omega_{j,\kappa} \rightarrow \omega_{j,\nabla B} + \omega_{j,\kappa}$ mapping then gives the ion-density kernel in the curvature model as given by Eqn. (32) in the main text where the plasma dispersion function $Z(\zeta) = i\sqrt{\pi} \mathcal{W}(\zeta)$ was favoured over the Faddeeva function.

As the FLR damping terms appear explicitly in Eqn. (32), it is straightforward to apply the reduced FLR models in Section V, for the purpose of creating hybrid reduced models. Using the Padé approximation $\Gamma_0(b_j) \approx 1/(1 + b_j)$ yields

$$\begin{aligned} h_{\text{ion},j}^{\text{curv}} &= \frac{1}{1 + b_j} \left[-i\sqrt{\pi} \sigma_\gamma \sigma_\kappa \sqrt{\frac{\omega}{2\omega_{j,\kappa}^{\text{eff}}}} \mathcal{W} \left(\sigma_\gamma \sigma_\kappa \sqrt{\frac{\omega}{2\omega_{j,\kappa}^{\text{eff}}}} \right) \right. \\ &\left(\left[1 - \frac{\omega_{\nabla n_j}}{\omega} + \frac{\omega_{\nabla T_j}}{2\omega} \right] + \frac{\omega_{\nabla T_j}}{\omega} \frac{b_j}{1 + b_j} \right) + \frac{\omega_{\nabla T_j}}{2\omega_{j,\kappa}^{\text{eff}}} \times \\ &\left. \left(1 + i\sqrt{\pi} \sigma_\gamma \sigma_\kappa \sqrt{\frac{\omega}{2\omega_{j,\kappa}^{\text{eff}}}} \mathcal{W} \left(\sigma_\gamma \sigma_\kappa \sqrt{\frac{\omega}{2\omega_{j,\kappa}^{\text{eff}}}} \right) \right) \right] \end{aligned} \quad (\text{C18})$$

where we used $\Gamma_1(b_j) - \Gamma_0(b_j) = d\Gamma_0(b_j)/db_j$, with the drift-kinetic limit being straightforwardly obtainable from Eqn. (C18) by letting $b_j \rightarrow 0$.

4. ∇B + Padé model

The ∇B model can be mapped onto Eqn. (14) through $\omega_{j,\kappa} \rightarrow 0$ and $\omega_{j,\nabla B} \rightarrow \omega_{j,\nabla B} + \omega_{j,\kappa}$, yielding

$$\begin{aligned} J_j^{\nabla B,0} &= \frac{\omega}{i\sigma_\gamma} \int_0^\infty \frac{e^{i\sigma_\gamma \omega \xi} \Gamma_0\left(\frac{b_j}{1+i\sigma_\gamma \omega_{j,\nabla B}^{\text{eff}} \xi}\right)}{1+i\sigma_\gamma \omega_{j,\nabla B}^{\text{eff}} \xi} \\ J_{j,\perp}^{\nabla B,2} &= \frac{2\omega}{i\sigma_\gamma} \int_0^\infty \frac{e^{i\sigma_\gamma \omega \xi} \left(\frac{dz\Gamma_0(z)}{dz}\right)\bigg|_{z=\frac{b_j}{1+i\sigma_\gamma \omega_{j,\nabla B}^{\text{eff}} \xi}}}{\left(1+i\sigma_\gamma \omega_{j,\nabla B}^{\text{eff}} \xi\right)^2} \\ J_{j,\parallel}^{\nabla B,2} &= \frac{\omega}{i\sigma_\gamma} \int_0^\infty \frac{e^{i\sigma_\gamma \omega \xi} \Gamma_0\left(\frac{b_j}{1+i\sigma_\gamma \omega_{j,\nabla B}^{\text{eff}} \xi}\right)}{1+i\sigma_\gamma \omega_{j,\nabla B}^{\text{eff}} \xi} \end{aligned} \quad (\text{C19})$$

where the explicit representation of $\hat{b}_j(\xi)$ was used to highlight its modification under the ∇B model, and $\omega_{j,\nabla B}^{\text{eff}} = \omega_{j,\kappa} + \omega_{j,\nabla B}$ is introduced as short-hand notation. We immediately note from Eqn. (C19) that $J_j^{\nabla B,0} = J_{j,\parallel}^{\nabla B,2}$, thus rendering one of the integrals redundant, and reducing the ion-density kernel Eqn. (18) in the ∇B model to

$$h_{\text{ion},j}^{\nabla B} = \Gamma_0(b_j) - \frac{\omega_{\nabla n_j} - \omega_{\nabla T_j}}{\omega} J_j^{\nabla B,0} + \frac{\omega_{j,\nabla B}^{\text{eff}} - \omega_{\nabla T_j}}{2\omega} J_{j,\perp}^{\nabla B,2}. \quad (\text{C20})$$

Alas, further analytical is not possible as the (default) ∇B model does not alleviate the coupling between the FLR and drift physics, but rather modifies $\hat{b}_j(\xi)$ by the augmented ∇B -drift.

This difficulty can be alleviated by invoking the Padé approximation $\Gamma_0(\hat{b}_j) \approx 1/(1+\hat{b}_j)$ for the Bessel function, where in case of $J_{j,\perp}^{\nabla B,2}$ we apply the approximation prior to evaluating the derivative, yielding the mapping $\{J_j^{\nabla B,0}, J_{j,\perp}^{\nabla B,2}\} \rightarrow \{J_j^{\nabla B+\text{Padé},0}, J_{j,\perp}^{\nabla B+\text{Padé},1}\}$ in terms of the following generic integral

$$J_j^{\nabla B+\text{Padé},m} = (1+m) \frac{\omega}{i\sigma_\gamma} \int_0^\infty \frac{e^{i\sigma_\gamma \omega \xi}}{\left(1+b_j+i\sigma_\gamma \omega_{j,\nabla B}^{\text{eff}} \xi\right)^{m+1}}. \quad (\text{C21})$$

Using the coordinate transform $\eta_{\nabla B} = -(\omega/\omega_{j,\nabla B}^{\text{eff}})(1+b_j+i\sigma_\gamma \omega_{j,\nabla B}^{\text{eff}} \xi)$, Eqn. (C21) can be solved analytically in terms of

$$\begin{aligned} J_j^{\nabla B+\text{Padé},m} &= (1+m) \left(-\frac{\omega}{\omega_{j,\nabla B}^{\text{eff}}}\right)^{m+1} e^{-\frac{\omega(1+b_j)}{\omega_{j,\nabla B}^{\text{eff}}}} \times \\ &\quad \int_{\infty e^{i\arg[-i\sigma_\gamma \omega]}}^0 \frac{e^{-\eta_{\nabla B}}}{\eta_{\nabla B}^{m+1}} \cdot \\ &\quad - \frac{\omega(1+b_j)}{\omega_{j,\nabla B}^{\text{eff}}} \end{aligned} \quad (\text{C22})$$

By virtue of the transform, the phase of the upper-bound is constrained to within $-\pi/2 \leq \arg \eta_{\nabla B} \leq \pi/2$ regardless whether the mode is unstable or damped, such that integrals over the exponential are asymptotically vanishing, hence (for $m > -2$) by integrating Eqn. (C22) along the shifted and skewed pizza-slice-shaped contour from Figure 9, we may perform the integral along the path $\eta_{\nabla B} \in [-\omega(1+b_j)/\omega_{j,\nabla B}^{\text{eff}}, \infty)$ instead. For $m \neq 0$ integration by parts yields the recurrence relation

$$J_j^{\nabla B+\text{Padé},m} = -\frac{\omega}{\omega_{j,\nabla B}^{\text{eff}}} \frac{1+m}{m} \left(\frac{1}{(1+b_j)^m} - \frac{J_j^{\nabla B+\text{Padé},m-1}}{m} \right) \quad (\text{C23})$$

with generating integral of the sequence being $m = 0$

$$J_j^{\nabla B+\text{Padé},0} = -\frac{\omega}{\omega_{j,\nabla B}^{\text{eff}}} e^{-\frac{\omega(1+b_j)}{\omega_{j,\nabla B}^{\text{eff}}}} E_1\left(-\frac{\omega(1+b_j)}{\omega_{j,\nabla B}^{\text{eff}}}\right) \quad (\text{C24})$$

where $E_1(z) = \int_z^\infty dt e^{-t}/t$ is the exponential integral. Note that alternative to using Eqn. (C23), one could also find $J_j^{\nabla B+\text{Padé},1} = -2 dJ_j^{\nabla B+\text{Padé},0}/db_j$, which using the properties of the generalised exponential integral⁸³ $E_n(z) = \int_1^\infty dt e^{-zt}/t^n$, can be shown to match with Eqn. (C23) for $m = 1$, in case of $\omega_R/\omega_{j,\nabla B}^{\text{eff}} < 0$. It should be noted that the recurrence relation Eqn. (C23), however, is only limited in validity to $(\omega_{j,\nabla B}^{\text{eff}}, \gamma) \neq (0, 0)$, and is otherwise an exact result. Combining Eqns. (C23) and (C24) to obtain Eqn. (C21) and inserting into Eqn. (C20) along with setting $\Gamma_0(b_j) \rightarrow 1/(1+b_j)$ to consistently apply the Padé approximation then yields Eqn. (33) from the main text. The DK limit is then straightforwardly obtained by setting $b_j \rightarrow 0$ in Eqn. (33).

Appendix D: Strongly-driven limit of charge-density kernels

In typical drift-wave ordering, the mode frequency scales as^{8,48,51,172} $\omega \sim \omega_{\nabla n_e}$, hence as the gradients are increased, the mode frequency will satisfy $\omega_{ds}/\omega \ll 1$ in the thermal bulk, and consequently resonances with the toroidal drift are weak as they are driven by particles in the tails of the distribution function.

In such scenarios, it is lucid to expand the integrands in the ion-resonance integrals Eqn. (14) for $\omega_{j,\kappa}/\omega \sim \omega_{j,\nabla B}/\omega \ll 1$. Such frequency ratios can explicitly be enforced, to provide a formal basis for these expansions, by the coordinate

transform $\zeta = -i\sigma_\gamma\omega$, yielding

$$\begin{aligned}
 J_j^{(0)} &= \int_0^{\infty e^{i\arg[-i\sigma_\gamma\omega]}} d\zeta \frac{e^{-\zeta} \Gamma_0\left(\frac{b_j}{1 - \frac{\omega_{j,\nabla B}}{\omega} \zeta}\right)}{\sqrt{1 - 2\frac{\omega_{j,\kappa}}{\omega} \zeta} \left(1 - \frac{\omega_{j,\nabla B}}{\omega} \zeta\right)} \\
 J_{j,\perp}^{(2)} &= 2 \int_0^{\infty e^{i\arg[-i\sigma_\gamma\omega]}} d\zeta \frac{e^{-\zeta} \left.\frac{d\Gamma_0(z)}{dz}\right|_{z=\frac{b_j}{1 - \frac{\omega_{j,\nabla B}}{\omega} \zeta}}}{\sqrt{1 - 2\frac{\omega_{j,\kappa}}{\omega} \zeta} \left(1 - \frac{\omega_{j,\nabla B}}{\omega} \zeta\right)^2} \quad (D1) \\
 J_{j,\parallel}^{(2)} &= \int_0^{\infty e^{i\arg[-i\sigma_\gamma\omega]}} d\zeta \frac{e^{-\zeta} \Gamma_0\left(\frac{b_j}{1 - \frac{\omega_{j,\nabla B}}{\omega} \zeta}\right)}{\left(1 - 2\frac{\omega_{j,\kappa}}{\omega} \zeta\right)^{3/2} \left(1 - \frac{\omega_{j,\nabla B}}{\omega} \zeta\right)}.
 \end{aligned}$$

In Eqn. (D1) the singularities at $\zeta_{\nabla B}^* = \omega/\omega_{j,\nabla B}$ and $\zeta_\kappa^* = \omega/(2\omega_{j,\kappa})$ have a fixed phase of $\arg \zeta_{\{\kappa,\nabla B\}}^* = \arg \omega + \pi(1 - \sigma_{\{\kappa,\nabla B\}})/2$ where $\sigma_{\{\kappa,\nabla B\}} = \text{sgn } \omega_{j,\{\kappa,\nabla B\}}$ is the sign of drift associated with the singularity, which do not intersect with the straight-integration path $\zeta \in [0, \infty e^{i\arg[-i\sigma_\gamma\omega]}]$, at constant phase of $\arg \zeta = \omega - \pi\sigma_\gamma/2$. Consequently, as this path is further constrained to lie within the region $|\arg \zeta| < \pi/2$ where the exponential function is asymptotically vanishing, an evaluation of Eqn. (D1) along the pizza-slice-shaped contour of Figure 8 allows to perform the integrals along the path $\zeta \in [0, \infty)$ instead by virtue of Cauchy's theorem. By additionally replacing each term in Eqn. (D1) containing the small parameters $\omega_{j,\nabla B}/\omega \ll 1$ and $\omega_{j,\kappa}/\omega \ll 1$ by its first-order Taylor expansion we obtain

$$\begin{aligned}
 J_j^0 &\approx \int_0^\infty d\zeta e^{-\zeta} \left(1 + \frac{\omega_{j,\nabla B}}{\omega} \zeta\right) \left(1 + \frac{\omega_{j,\kappa}}{\omega} \zeta\right) \left(\Gamma_0(b_j) + b_j \frac{d\Gamma_0(b_j)}{db_j} \frac{\omega_{j,\nabla B}}{\omega} \zeta\right) + \mathcal{O}\left(\left(\frac{\omega_{j,\nabla B}}{\omega}\right)^2, \left(\frac{\omega_{j,\kappa}}{\omega}\right)^2\right) \\
 &\approx \Gamma_0(b_j) \left(1 + \frac{\omega_{j,\nabla B} + \omega_{j,\kappa}}{\omega}\right) + b_j [\Gamma_1(b_j) - \Gamma_0(b_j)] \frac{\omega_{j,\nabla B}}{\omega} + \mathcal{O}\left(\left(\frac{\omega_{j,\nabla B}}{\omega}\right)^2, \frac{\omega_{j,\nabla B}\omega_{j,\kappa}}{\omega^2}, \left(\frac{\omega_{j,\kappa}}{\omega}\right)^2\right) \\
 J_{j,\perp}^{(2)} &\approx 2 \int_0^\infty d\zeta e^{-\zeta} \left(1 + 2\frac{\omega_{j,\nabla B}}{\omega} \zeta\right) \left(1 + \frac{\omega_{j,\kappa}}{\omega} \zeta\right) \left(\frac{d(b_j\Gamma_0(b_j))}{db_j} + b_j \frac{d^2(b_j\Gamma_0(b_j))}{db_j^2} \frac{\omega_{j,\nabla B}}{\omega} \zeta\right) + \mathcal{O}\left(\left(\frac{\omega_{j,\nabla B}}{\omega}\right)^2, \left(\frac{\omega_{j,\kappa}}{\omega}\right)^2\right) \\
 &\approx 2 \left((\Gamma_0(b_j) + b_j [\Gamma_1(b_j) - \Gamma_0(b_j)]) \left(1 + \frac{\omega_{j,\kappa}}{\omega}\right) + \frac{\omega_{j,\nabla B}}{\omega} (b_j [\Gamma_1(b_j) - \Gamma_0(b_j)] (3 - 2b_j) + \Gamma_0(b_j) (2 - b_j))\right) + \\
 &\quad \mathcal{O}\left(\left(\frac{\omega_{j,\nabla B}}{\omega}\right)^2, \frac{\omega_{j,\nabla B}\omega_{j,\kappa}}{\omega^2}, \left(\frac{\omega_{j,\kappa}}{\omega}\right)^2\right) \\
 J_{j,\parallel}^{(2)} &\approx \int_0^\infty d\zeta e^{-\zeta} \left(1 + \frac{\omega_{j,\nabla B}}{\omega} \zeta\right) \left(1 + 3\frac{\omega_{j,\kappa}}{\omega} \zeta\right) \left(\Gamma_0(b_j) + b_j \frac{d\Gamma_0(b_j)}{db_j} \frac{\omega_{j,\nabla B}}{\omega} \zeta\right) + \mathcal{O}\left(\left(\frac{\omega_{j,\nabla B}}{\omega}\right)^2, \left(\frac{\omega_{j,\kappa}}{\omega}\right)^2\right) \\
 &\approx \Gamma_0(b_j) \left(1 + \frac{\omega_{j,\nabla B} + 3\omega_{j,\kappa}}{\omega}\right) + b_j [\Gamma_1(b_j) - \Gamma_0(b_j)] \frac{\omega_{j,\nabla B}}{\omega} + \mathcal{O}\left(\left(\frac{\omega_{j,\nabla B}}{\omega}\right)^2, \frac{\omega_{j,\nabla B}\omega_{j,\kappa}}{\omega^2}, \left(\frac{\omega_{j,\kappa}}{\omega}\right)^2\right) \quad (D2)
 \end{aligned}$$

where all ζ integrals are evaluated using the Euler gamma function $\Gamma(n+1) = n!$, and the recurrence relation between the modified Bessel functions of first-kind I_n ⁸³ were used to evaluate the derivatives of $\Gamma_0(b_j)$. In Eqn. (D2) only first-order effects in $\omega_{j,\kappa}/\omega$ and $\omega_{j,\nabla B}/\omega$ were retained, since the quadratic and higher-order terms caused by the products

of the expansions are spurious, resulting in erroneous coefficients as they lack the proper contributions from the second- and higher-order Taylor expansions of the integrand terms.

Substituting Eqn. (D2) into Eqn. (18) then gives the strongly-driven limit for the ion-density kernel after some rearrangement as

$$\begin{aligned}
 h_{\text{ion},j}^{\text{str.drive}} &\approx \Gamma_0(b_j) \left[1 - \frac{\omega_{\nabla n_j}}{\omega} + \frac{\omega_{j,\kappa} + \omega_{j,\nabla B}}{\omega} - \frac{(\omega_{\nabla n_j} + \omega_{\nabla T_j})(\omega_{j,\nabla B} + \omega_{j,\kappa})}{\omega^2} + b_j \frac{\omega_{\nabla T_j} \omega_{j,\nabla B}}{\omega^2}\right] \\
 &\quad + b_j (\Gamma_1(b_j) - \Gamma_0(b_j)) \left[\frac{\omega_{j,\nabla B}}{\omega} - \frac{\omega_{\nabla T_j}}{\omega} - \frac{\omega_{j,\nabla B}(\omega_{\nabla n_j} + \omega_{\nabla T_j})}{\omega^2} - \frac{\omega_{\nabla T_j}(\omega_{j,\kappa} + \omega_{j,\nabla B})}{\omega^2} + 2b_j \frac{\omega_{\nabla T_j} \omega_{j,\nabla B}}{\omega^2}\right] \quad (D3)
 \end{aligned}$$

where quadratic terms in $\omega_{j,\nabla B}/\omega \sim \omega_{j,\kappa}/\omega \ll 1$ arising

from multiplication with frequency prefactors have been ne-

glected, as such higher-order terms would be spurious for the aforementioned reason.

With regards to the trapped-electrons, the strongly driven-limit of $\omega_{e,\kappa}/\omega \sim \omega_{e,\nabla B}/\omega \ll 1$ is equivalent to $\overline{\omega_{de}^T}/\omega \ll 1$, hence one could take the proper asymptotic limit for the plasma dispersion function in the trapped-electron resonant integrals Eqn. (15). However, extra care must be taken when the bounce-averaged drift is marginally close to vanishing rather than finite. In the limit that $\overline{\omega_{de}^T}/\omega \rightarrow 0$, whilst $\sqrt{\omega/\overline{\omega_{de}^T}}$ will approach complex infinity, simultaneously $\mathcal{W}(\sigma_\gamma \sigma_d \sqrt{\omega/\overline{\omega_{de}^T}})$ vanishes asymptotically. When the bounce-averaged drift becomes vanishingly small, (which shall always be achieved by some populations of trapped-particles for the drift-wells must have roots in order for the passing particle drift to vanish on a transit-average), the trapped-electron energy integral $I_{\text{tr-el}}$ Eqn. (A9) has an almost trivially well defined limit. The intricacy of complex infinities in the analytical solution Eqn. (15) is an unphysical aftermath from the coordinate transform $\mu =$

$-i\sigma_\gamma \sigma_d \sqrt{\omega/\overline{\omega_{de}^T}} \sqrt{1 + i\sigma_\gamma \overline{\omega_{de}^T} \xi}$, considered in Section A 2 to simplify the emergent integrals of Eqn. (A10), breaking down when the bounce-averaged drift vanishes.

If instead we invoke the same $\zeta = -i\sigma_\gamma \omega \xi$ coordinate transform considered for the ions, these integrals are rendered as

$$J_{\text{tr-el}}^m = \Gamma\left(\frac{2m+1}{2}\right) \int_0^\infty d\zeta \frac{e^{-\zeta}}{\left(1 - \frac{\overline{\omega_{de}^T}}{\omega} \zeta\right)^{\frac{2m+1}{2}}} \quad (\text{D4})$$

where we have performed integration along the pizza-slice-shaped contour from Figure 8 to reroute the integration path along the real-line, valid for similar arguments as in the ion case. As Eqn. (D4) is continuous in $\overline{\omega_{de}^T}$, the strongly-driven limit may be used to smoothly connect the solutions to Eqn. (A10) between asymptotically small and completely vanishing drifts, where upon applying the binomial expansion to the denominator we have

$$\begin{aligned} \frac{J_{\text{tr-el}}^m}{\Gamma\left(\frac{2m+1}{2}\right)} = I^m &\approx \int_0^\infty e^{-\zeta} \left(1 + \frac{2m+1}{2} \frac{\overline{\omega_{de}^T}}{\omega} \zeta + \frac{(2m+1)(2m-1)}{8} \zeta^2\right) + \mathcal{O}\left(\left(\frac{\overline{\omega_{de}^T}}{\omega}\right)^3\right) \\ &\approx 1 + \frac{2m+1}{2} \frac{\overline{\omega_{de}^T}}{\omega} + \frac{(2m+1)(2m+3)}{4} \left(\frac{\overline{\omega_{de}^T}}{\omega}\right)^2 + \mathcal{O}\left(\left(\frac{\overline{\omega_{de}^T}}{\omega}\right)^3\right) \end{aligned} \quad (\text{D5})$$

where we have defined I^m analogous to Eqn. (A12), and maintained the expansion up to second order, as it insightfully reveals that the recursive relation Eqn. (A13) remains maintained up to first order in $\overline{\omega_{de}^T}/\omega$ for all $m \neq 1/2$ if one delays truncation. In fact, it is straightforward to show that Eqn. (A13) remains valid up to order $\mathcal{O}\left(\left(\frac{\overline{\omega_{de}^T}}{\omega}\right)^N\right)$ if one truncates the binomial expansion at $(N+1)^{\text{th}}$ order. Note that Eqn. (D5) is always well-defined, including when $\overline{\omega_{de}^T} \rightarrow 0$. When the bounce-averaged drift is finite, but still sufficiently small for the strongly-driven limit $\overline{\omega_{de}^T}/\omega \ll 1$ to be applicable, an asymptotic expansion of the Faddeeva function Eqn. (A15) for $\zeta \gg 1$ in the analytical solutions Eqn. (15) yields⁸³

$$\begin{aligned} I^1 &\sim \sum_{m=0}^\infty \frac{(2(m+1))!}{(m+1)!2^{2m+1}} \left(\frac{\overline{\omega_{de}^T}}{\omega}\right)^m \\ I^2 &\sim \frac{1}{3} \sum_{m=0}^\infty \frac{(2(m+2))!}{(m+2)!2^{2m+2}} \left(\frac{\overline{\omega_{de}^T}}{\omega}\right)^m \end{aligned} \quad (\text{D6})$$

where we accounted for the notational difference that the $J_{\text{tr-el}}^m$ as appear in the main text are actually the integrals I^m as mentioned in Section A 2 for consistency, and note that the

first three terms of Eqn. (D6) agree with Eqn. (D5) for both $m = 1, 2$, showing consistency between the analytical solution and the strongly-driven limit for trapped-particles not subject to a marginally vanishing bounce-averaged drift. In obtaining Eqn. (D6), the large-argument asymptotic expansion of the $\text{erfc}(z)$ was used, which is valid only when $|\arg z| < 3\pi/4$. For the resonant TEM integrals $z = -i\sigma_\gamma \sigma_{de} \sqrt{\omega/\overline{\omega_{de}^T}}$, whose argument is always constrained within $|\arg z| \in (0, \pi)$ and hence always lies in applicable range by virtue of the sign generalisation gained from the chain of integral transforms used to obtain the plasma dispersion function.

Inserting Eqn. (D5) into Eqn. (18), and taking into account that the $J_{\text{tr-el}}^m$ as appear in the main text are actually the integrals I^m as mentioned in Section A 2, we obtain the strongly-driven limit for the trapped-electron pitch-angle density kernel as

$$K_{\text{tr-el}}^{\text{str,drive}} \approx \frac{1}{2} \left(1 - \frac{\omega_{\nabla n_e}}{\omega}\right) + \frac{3}{4} \frac{\overline{\omega_{de}^T}}{\omega} \left(1 - \frac{\omega_{\nabla n_e} + \omega_{\nabla T_e}}{\omega}\right) \quad (\text{D7})$$

where quadratic and higher-order terms in $\overline{\omega_{de}^T}/\omega$ have been neglected to keep the expansion consistent with Eqn. (D3) for the ions.

Application to reduced models

Here we will only focus on the effect of reduced models on the ion-density kernel, since the trapped-electron pitch-angle density kernel Eqn. (D7) is only moderately affected by the choice of the drift model through modification of the bounce-averaged drift Eqn. (34), with the trapped-electrons response already assumed to be drift-kinetic.

As the curvature- and ∇B models of the magnetic drift can be mapped onto the “full drift” scenario by setting the name-sake drift-component equal to the full drift $\omega_{j,\alpha} \rightarrow \omega_{j,\kappa} + \omega_{j,\nabla B}$ whilst making the other component vanish $\omega_{j,\neq\alpha} \rightarrow 0$, where $\alpha = \{\kappa, \nabla B\}$, the appropriate strongly-driven limit for the reduced drift models whilst retaining the full FLR effects are readily obtained by making the suitable substitutions to Eqn. (D3). This substitution ensures that the relative qualitative aspect of the toroidal drift-driven instability mechanism with respect to the full resonant integrals remains conserved across the reduced models. Perhaps enlightening, the explicit form of Eqn. (D3) reveals that much of the physics in the

strongly-driven limit does not depend on a particular component, but rather the combined magnetic drift $\omega_{j,\kappa} + \omega_{j,\nabla B}$, hence leaving those terms unaffected. Rather, as the few symmetry breaking terms between the drift components are all proportional to $\omega_{j,\nabla B}$, these terms are either completely suppressed or enhanced, by adopting the reduced drift model.

For the suitable strongly-driven limit of the reduced FLR models, we reconsider Eqn. (C2) considered for the Padé approximation of the Bessel functions, as for the reduced FLR models the resonant integrands are directly modified and thus cannot be straightforwardly mapped onto the original “full FLR” model by making an appropriate substitution to Eqn. (D3). For the the integrals of Eqn. (C2) we proceed analogous to the TEM resonant integral by applying the change of coordinates $\zeta = -i\sigma_\gamma\omega\xi$, integrating along the pizza-slice-shaped contour from Figure 8 to reroute the integration path along the real-line as the emerging singularities $\zeta_\kappa^{*,\text{Padé}} = v\omega/(2\omega_{j,\kappa})$ and $\zeta_{\nabla B}^{*,\text{Padé}} = \lambda\omega/(\omega_{j,\nabla B})$ lie outside of the contour given $\lambda, v > 0$, resulting in

$$\begin{aligned}
 J_j^{0,v,\lambda} &= \int_0^\infty d\zeta \frac{e^{-\zeta}}{\sqrt{v - 2\frac{\omega_{j,\kappa}}{\omega}\zeta} \left(\lambda - \frac{\omega_{j,\nabla B}}{\omega}\zeta \right)} \\
 &\approx \frac{1}{\lambda\sqrt{v}} \left(1 + \frac{v\omega_{j,\nabla B} + \lambda\omega_{j,\kappa}}{\lambda v\omega} + \frac{2(v\omega_{j,\nabla B})^2 + 2\lambda v\omega_{j,\nabla B}\omega_{j,\kappa} + 3(\lambda\omega_{j,\kappa})^2}{(\lambda v\omega)^2} \right) + \mathcal{O}(\delta^3) \\
 J_{j,\perp}^{2,v,\lambda} &= 2 \int_0^\infty d\zeta \frac{e^{-\zeta}}{\sqrt{v - 2\frac{\omega_{j,\kappa}}{\omega}\zeta} \left(\lambda - \frac{\omega_{j,\nabla B}}{\omega}\zeta \right)^2} \\
 &\approx \frac{2}{\lambda^2\sqrt{v}} \left(1 + \frac{2v\omega_{j,\nabla B} + \lambda\omega_{j,\kappa}}{\lambda v\omega} + \frac{6(v\omega_{j,\nabla B})^2 + 4\lambda v\omega_{j,\nabla B}\omega_{j,\kappa} + 3(\lambda\omega_{j,\kappa})^2}{(\lambda v\omega)^2} \right) + \mathcal{O}(\delta^3) \\
 J_{j,\parallel}^{2,v,\lambda} &= \int_0^\infty d\zeta \frac{e^{-\zeta}}{\left(v - 2\frac{\omega_{j,\kappa}}{\omega}\zeta \right)^{3/2} \left(\lambda - \frac{\omega_{j,\nabla B}}{\omega}\zeta \right)} \\
 &\approx \frac{1}{\lambda v^{3/2}} \left(1 + \frac{v\omega_{j,\nabla B} + 3\lambda\omega_{j,\kappa}}{\lambda v\omega} + \frac{2(v\omega_{j,\nabla B})^2 + 6\lambda v\omega_{j,\nabla B}\omega_{j,\kappa} + 15(\lambda\omega_{j,\kappa})^2}{(\lambda v\omega)^2} \right) + \mathcal{O}(\delta^3)
 \end{aligned} \tag{D8}$$

where for each integral in the subsequent step we performed a binomial expansion of the terms in the denominator, retaining all terms up to second order in $\omega_{j,\nabla B}/\omega \sim \omega_{j,\kappa}/\omega \sim \delta \ll 1$ and $\mathcal{O}(\delta^3)$ is a shorthand notation for $\mathcal{O}\left(\left(\frac{\omega_{j,\nabla B}}{\omega}\right)^3, \left(\frac{\omega_{j,\kappa}}{\omega}\right)^3, \frac{\omega_{j,\nabla B}\omega_{j,\kappa}^2}{\omega^3}, \frac{\omega_{j,\nabla B}^2\omega_{j,\kappa}}{\omega^3}\right)$ accounting for all combinations of cubic order terms. In particular by retaining second order effects in $J_j^{0,v,\lambda}$ but truncating both $J_{j,\perp}^{2,v,\lambda}, J_{j,\parallel}^{2,v,\lambda}$ at first order, the interrelation Eqn. (C4) between these integrals holds up to first order in $\omega_{j,\kappa}/\omega \sim \omega_{j,\nabla B}/\omega \sim \delta$ as well, and like the TEM case, one may show that this interrelation continues being valid up to $\mathcal{O}(\delta^N)$ if the bi-

nomial expansions for $J_j^{0,v,\lambda}, J_{j,\perp}^{2,v,\lambda}, J_{j,\parallel}^{2,v,\lambda}$ are truncated at $(N+1)^{\text{th}}, N^{\text{th}}, N^{\text{th}}$ order respectively.

Upon setting $v \rightarrow 1, \lambda \rightarrow 1 + b_j$ we note that the expressions for $J_j^{0,v,\lambda}$ and $J_{j,\parallel}^{2,v,\lambda}$ from Eqn. (D8) match with the equivalent expressions of J_j^0 and $J_{j,\parallel}^{(2)}$ from Eqn. (D2) if the Bessel functions are Padé expanded (recalling that $\Gamma_1(b_j) - \Gamma_0(b_j) = d\Gamma_0(b_j)/db_j \approx -b_j/(1+b_j)$). The expression for $J_{j,\perp}^{2,v,\lambda}$, however, slightly deviates from the equivalent Padé ex-

pansion of $J_{j,\perp}^{(2)}$ from Eqn. (D2) by

$$\Delta^{\text{Padé, str. drive}} \equiv J_{j,\perp}^{(2)} - J_{j,\perp}^{2,1,1+b_j} = -\frac{2b_j^2(1-b_j)}{(1+b_j)^3} \frac{\omega_{j,\nabla B}}{\omega} \quad (\text{D9})$$

where the expression is to be understood to be only valid in the

strongly-driven limit and when considering the Padé approximation to be applied to the Bessel function in $J_{j,\perp}^{(2)}$. Using Eqn. (D9), the strongly-driven limit for the ion-density kernel under Padé approximation is then straightforwardly obtained as

$$\begin{aligned} h_{\text{ion},j}^{\text{Padé, str. drive}} &\approx \frac{1}{1+b_j} \left[1 - \frac{\omega_{\nabla n_j}}{\omega} + \frac{\omega_{j,\kappa} + \omega_{j,\nabla B}}{\omega} - \frac{(\omega_{\nabla n_j} + \omega_{\nabla T_j})(\omega_{j,\nabla B} + \omega_{j,\kappa})}{\omega^2} + b_j \frac{\omega_{\nabla T_j} \omega_{j,\nabla B}}{\omega^2} \right] \\ &\quad - \frac{b_j}{(1+b_j)^2} \left[\frac{\omega_{j,\nabla B}}{\omega} - \frac{\omega_{\nabla T_j}}{\omega} - \frac{\omega_{j,\nabla B}(\omega_{\nabla n_j} + \omega_{\nabla T_j})}{\omega^2} - \frac{\omega_{\nabla T_j}(\omega_{j,\kappa} + \omega_{j,\nabla B})}{\omega^2} + 2b_j \frac{\omega_{\nabla T_j} \omega_{j,\nabla B}}{\omega^2} \right] + \Delta^{\text{Padé, str. drive}} \frac{\omega_{\nabla T_j}}{2\omega} \\ &= \frac{1}{1+b_j} \left[1 - \frac{\omega_{\nabla n_j}}{\omega} + \frac{\omega_{j,\kappa} + \omega_{j,\nabla B}}{\omega} - \frac{\omega_{\nabla n_j}(\omega_{j,\nabla B} + \omega_{j,\kappa})}{\omega^2} - \frac{\omega_{\nabla T_j}(\omega_{j,\kappa} - \omega_{j,\nabla B})}{\omega^2} \right] \\ &\quad - \frac{b_j}{(1+b_j)^2} \left[\frac{\omega_{j,\nabla B}}{\omega} - \frac{\omega_{\nabla T_j}}{\omega} - \frac{\omega_{j,\nabla B}(\omega_{\nabla n_j} - \omega_{\nabla T_j})}{\omega^2} - \frac{\omega_{\nabla T_j} \omega_{j,\kappa}}{\omega^2} \right] - \frac{2}{(1+b_j)^3} \frac{\omega_{j,\nabla B} \omega_{\nabla T_j}}{\omega^2} \quad (\text{D10}) \end{aligned}$$

where only terms up to first order in δ were retained for consistency across the various strongly-driven models.

The fact that the discrepancy Eqn. (D9) applies only to $J_{j,\perp}^{(2)}$ can be traced back to the fact that within the strongly-driven limit J_j^0 and $J_{j,\parallel}^{(2)}$ are fully characterised by just Γ_0 and its first derivative, which are closely approximated by the Padé approximation since $\Gamma_0(b_j) \approx 1/(1+b_j)$ has an identical first-order Maclaurin series as $\Gamma_0(b_j)^{173}$, whilst information about the second derivative is embedded into $J_{j,\perp}^{(2)}$, whose behaviour is thus not closely followed by the Padé approximation. As this second-derivative term is multiplied by $\omega_{j,\nabla B}/\omega$, explaining the proportionality from Eqn. (D9), any discrepancy between the Padé approximation of the strongly-driven limit and the strongly-driven limit of the Padé approximation vanishes for the curvature model. This agrees with the above observation, since the underlying equations of the curvature model Eqn. (C16) only involve $\Gamma_0(b_j)$ and its first derivative.

Lastly, in the drift-kinetic limit of $b_j \rightarrow 0$ we obtain from both Eqns. (D3) and (D10)

$$\begin{aligned} h_{\text{ion},j}^{\text{DK, str. drive}} &\approx 1 - \frac{\omega_{\nabla n_j}}{\omega} + \frac{\omega_{j,\kappa} + \omega_{j,\nabla B}}{\omega} \\ &\quad - \frac{(\omega_{\nabla n_j} + \omega_{\nabla T_j})(\omega_{j,\nabla B} + \omega_{j,\kappa})}{\omega^2} \quad (\text{D11}) \end{aligned}$$

such that the discrepancy between the Padé approximation and the full-FLR model vanishes. This re-matching between Padé and full-FLR solution can be traced back to the vanishing of the $d^2(b_j\Gamma_0(b_j))/db_j^2$ term in the expression for $J_{j,\perp}^{(2)}$ in Eqn. (D2) in this limit, such that only $\Gamma_0(b_j)$ and its first-derivative, evaluated at $b = 0$, make an explicit appearance in the drift-kinetic limit of the ion-density kernel. Meanwhile, as the first-order Maclaurin series of $1/(1+b_j)$

matches that of $\Gamma_0(b_j)$, the Padé approximation accurately both predicts $\Gamma_0(b_j)$ and its first derivative at $b_j = 0$, causing the coefficients of the surviving terms to match. Additionally we note that any further discrepancy between the various approximations for the drift models Eqn. (29) also vanishes, as Eqn. (D11) only depends on the sum of the drift components $\omega_{j,\nabla B} + \omega_{j,\kappa}$, which through the mappings $\omega_{j,\alpha} \rightarrow \omega_{j,\kappa} + \omega_{j,\nabla B}$ and $\omega_{j,\neq\alpha} \rightarrow 0$ for $\alpha = \{\kappa, \nabla B\}$ remains invariant, conform the findings from Ref. 70.

¹ J. M. Canik, D. T. Anderson, F. S.B. Anderson, K. M. Likin, J. N. Talmadge, and K. Zhai. Experimental demonstration of improved neoclassical transport with quasihelical symmetry. *Physical Review Letters*, 98(8), 2007.

² C. D. Beidler, H. M. Smith, A. Alonso, T. Andreeva, J. Baldzuhn, M. N. A. Beurskens, M. Borchardt, S. A. Bozhnikov, K. J. Brunner, H. Damm, M. Drevlak, O. P. Ford, G. Fuchert, J. Geiger, P. Helander, U. Hergenbahn, M. Hirsch, U. Höfel, Ye. O. Kazakov, R. Kleiber, M. Krychowiak, S. Kwak, A. Langenberg, H. P. Laqua, U. Neuner, N. A. Pablant, E. Pasch, A. Pavone, T. S. Pedersen, K. Rahbarnia, J. Schilling, E. R. Scott, T. Stange, J. Svensson, H. Thomsen, Y. Turkin, F. Warmer, R. C. Wolf, D. Zhang, I. Abramovic, S. Äkäslompolo, J. Alcúsn, P. Aleynikov, K. Aleynikova, A. Ali, A. Alonso, G. Anda, E. Ascasibar, J. P. Böhner, S. G. Baek, M. Balden, M. Banduch, T. Barbui, W. Behr, A. Benndorf, C. Biedermann, W. Biel, B. Blackwell, E. Blanco, M. Blatzheim, S. Ballinger, T. Bluhm, D. Böckenhoff, B. Böswirth, L.-G. Böttger, V. Borsuk, J. Boscary, H.-S. Bosch, R. Brakel, H. Brand, C. Brandt, T. Bräuer, H. Braune, S. Brezinsek, K.-J. Brunner, R. Burhenn, R. Bussiahn, B. Buttenschön, V. Bykov, J. Cai, I. Calvo, B. Cannas, A. Cappa, A. Carls, L. Carraro, B. Carvalho, F. Castejon, A. Charl, N. Chaudhary, D. Chauvin, F. Chernyshev, M. Cianciosi, R. Citarella, G. Claps, J. Coenen, M. Cole, M. J. Cole, F. Cordella, G. Cseh, A. Czarnecka, K. Czerski, M. Czerwinski, G. Czymek, A. da Molin, A. da Silva, A. de la Pena, S. Degenkolbe, C. P. Dhard, M. Diben, A. Dinkelage, T. Dittmar, P. Drewelow, P. Drews, F. Durodie, E. Edlund, F. Effenberger, G. Ehrke, S. Elgeti, M. Endler, D. Ennis, H. Esteban, T. Estrada, J. Fellinger, Y. Feng, E. Flom, H. Fernandes, W. H. Fietz, W. Figacz, J. Fontdecaba, T. Fornal, H. Frerichs, A. Freund, T. Funaba, A. Galkowski, G. Gantenbein, Y. Gao, J. García Regaña, D. Gates, B. Geiger, V. Giannella, A. Gogoleva, B. Goncalves, A. Gorlaev, D. Gradic, M. Grahl, J. Green, H. Greuner, A. Grosman, H. Grote, M. Gruca, O. Grulke, C. Guerard, P. Hacker, X. Han, J. H. Harris, D. Hartmann, D. Hathiramani, B. Hein,

- B. Heinemann, P. Helander, S. Henneberg, M. Henkel, U. Hergenhan, J. Hernandez Sanchez, C. Hidalgo, K. P. Hollfeld, A. Hölting, D. Höschen, M. Houry, J. Howard, X. Huang, Z. Huang, M. Hubeny, M. Huber, H. Hunger, K. Ida, T. Ilkei, S. Illy, B. Israeli, S. Jablonski, M. Jakubowski, J. Jelonnek, H. Jenzsch, T. Jesche, M. Jia, P. Junghanns, J. Kacmarczyk, J.-P. Kallmeyer, U. Kamionka, H. Kasahara, W. Kasperek, N. Kenmochi, C. Killer, A. Kirschner, T. Klinger, J. Knauer, M. Knaup, A. Knieps, T. Kobarg, G. Kocsis, F. Köchl, Y. Kolesnichenko, A. Könies, R. König, P. Korniejew, J.-P. Koschinsky, F. Köster, M. Krämer, R. Krampitz, A. Krämer-Flecken, N. Krawczyk, T. Kremeyer, J. Krom, I. Ksiazek, M. Kubkowska, G. Kühner, T. Kurki-Suonio, P. A. Kurz, M. Landreman, P. Lang, R. Lang, S. Langish, H. Laqua, R. Laube, S. Lazerson, C. Lechte, M. Lennartz, W. Leonhardt, C. Li, C. Li, Y. Li, Y. Liang, C. Linsmeier, S. Liu, J.-F. Lob-sien, D. Loesser, J. Loizu Cisquella, J. Lore, A. Lorenz, M. Losert, A. Lücke, A. Lumsdaine, V. Lutsenko, H. Maaßberg, O. Marchuk, J. H. Matthew, S. Marsen, M. Marushchenko, S. Masuzaki, D. Maurer, M. Mayer, K. McCarthy, P. McNeely, A. Meier, D. Mellein, B. Mendelevitch, P. Mertens, D. Mikkelsen, A. Mishchenko, B. Missal, J. Mittelstaedt, T. Mizuchi, A. Mollen, V. Moncada, T. Mönnich, T. Morisaki, D. Moseev, S. Murakami, G. Náfrádi, M. Nagel, D. Naujoks, H. Neilson, R. Neu, O. Neubauer, T. Ngo, D. Nicolai, S. K. Nielsen, H. Niemann, T. Nishizawa, R. Nocentini, C. Nührenberg, J. Nührenberg, S. Obermayer, G. Offermanns, K. Ogawa, J. Ölmans, J. Ongena, J. W. Oosterbeek, G. Orozco, M. Otte, L. Pacios Rodriguez, N. Panadero, N. Panadero Alvarez, D. Papenfuß, S. Paqay, E. Pawelec, T. S. Pedersen, G. Pelka, V. Perseo, B. Peterson, D. Pilopp, S. Pingel, F. Pisano, B. Plum, G. Plunk, P. Pölöskei, M. Porkolab, J. Proll, M.-E. Puiatti, A. Puig Sitjes, F. Purps, M. Rack, S. Récssei, A. Reiman, F. Reimold, D. Reiter, F. Remppel, S. Renard, R. Riedl, J. Riemann, K. Risse, V. Rohde, H. Röhlinger, M. Romé, D. Rondeshagen, P. Rong, B. Roth, L. Rudischhauser, K. Rummel, T. Rummel, A. Runov, N. Rust, L. Ryc, S. Ryosuke, R. Sakamoto, M. Salewski, A. Samartsev, E. Sánchez, F. Sano, S. Satake, J. Schacht, G. Satheeswaran, F. Schauer, T. Scherer, A. Schlaich, G. Schlisio, F. Schluck, K.-H. Schlüter, J. Schmitt, H. Schmitz, O. Schmitz, S. Schmuck, M. Schneider, W. Schneider, P. Scholz, R. Schrittwieser, M. Schröder, T. Schröder, R. Schroeder, H. Schumacher, B. Schweer, S. Sereda, B. Shanahan, M. Sibilia, P. Sinha, S. Sipliä, C. Slaby, M. Slecicka, W. Spiess, D. A. Spong, A. Spring, R. Stadler, M. Stejner, L. Stephey, U. Stridde, C. Suzuki, V. Szabó, T. Szabolics, T. Szepesi, Z. Szökefalvi-Nagy, N. Tamura, A. Tancetti, J. Terry, J. Thomas, M. Thumm, J. M. Traverso, P. Traverso, J. Tretter, H. Trimino Mora, H. Tsuchiya, T. Tsujimura, S. Tulipán, B. Unterberg, I. Vakulchik, S. Valet, L. Vanó, P. van Eeten, B. van Milligen, A. J. van Vuuren, L. Vela, J.-L. Velasco, M. Vergote, M. Vervier, N. Vianello, H. Viebke, R. Vilbrandt, A. von Stechow, A. Vorköper, S. Wadle, F. Wagner, E. Wang, N. Wang, Z. Wang, T. Wauters, L. Wegener, J. Weggen, T. Wegner, Y. Wei, G. Weir, J. Wendorf, U. Wenzel, A. Werner, A. White, B. Wiegel, F. Wilde, T. Windisch, M. Winkler, A. Winter, V. Winters, S. Wolf, R. C. Wolf, A. Wright, G. Wurden, P. Xanthopoulos, H. Yamada, I. Yamada, R. Yasuhara, M. Yokoyama, M. Zanini, M. Zarnstorff, A. Zeitler, H. Zhang, H. Zhu, M. Zilker, A. Zocco, S. Zoletnik, and M. Zuin. Demonstration of reduced neoclassical energy transport in Wendelstein 7-X. *Nature*, 596(7871):221–226, 8 2021.
- ³Ulrich Stroth. A comparative study of transport in stellarators and tokamaks. *Plasma Physics and Controlled Fusion*, 40(1):9, 1 1998.
- ⁴J W Connor and H R Wilson. Survey of theories of anomalous transport. *Plasma Physics and Controlled Fusion*, 36(5):719–795, 5 1994.
- ⁵F. Jenko, W. Dorland, M. Kotschenreuther, and B. N. Rogers. Electron temperature gradient driven turbulence. *Physics of Plasmas*, 7(5):1904, 4 2000.
- ⁶F Merz and F Jenko. Nonlinear interplay of TEM and ITG turbulence and its effect on transport. *Nuclear Fusion*, 50(5):054005, 4 2010.
- ⁷W.M. Tang. Microinstability theory in tokamaks. *Nuclear Fusion*, 18(8):1089–1160, 8 1978.
- ⁸W. Horton. Drift waves and transport. *Reviews of Modern Physics*, 71(3):735–778, 4 1999.
- ⁹P. Mulholland, M.J. Pueschel, J.H.E. Proll, K. Aleynikova, B.J. Faber, P.W. Terry, C.C. Hegna, and C. Nührenberg. Finite- β turbulence in Wendelstein 7-X enhanced by sub-threshold kinetic ballooning modes. *Nuclear Fusion*, 65(1):016022, 1 2025.
- ¹⁰M. J. Pueschel, M. Kammerer, and F. Jenko. Gyrokinetic turbulence simulations at high plasma beta. *Physics of Plasmas*, 15(10), 10 2008.
- ¹¹H. Doerk, F. Jenko, M. J. Pueschel, and D. R. Hatch. Gyrokinetic microtearing Turbulence. *Physical Review Letters*, 106(15):155003, 4 2011.
- ¹²P. H. Rutherford and E. A. Frieman. Drift Instabilities in General Magnetic Field Configurations. *Physics of Fluids*, 11(3):569–585, 3 1968.
- ¹³P J Catto, W M Tang, and D E Baldwin. Generalized gyrokinetics. *Plasma Physics*, 23(7):639–650, 7 1981.
- ¹⁴Thomas M. Antonsen and Barton Lane. Kinetic equations for low frequency instabilities in inhomogeneous plasmas. *The Physics of Fluids*, 23(6):1205–1214, 6 1980.
- ¹⁵A. J. Brizard and T. S. Hahm. Foundations of nonlinear gyrokinetic theory. *Reviews of Modern Physics*, 79(2):421, 4 2007.
- ¹⁶G. Rewoldt, L.-P. Ku, and W. M. Tang. Comparison of microinstability properties for stellarator magnetic geometries. *Physics of Plasmas*, 12(10), 10 2005.
- ¹⁷J. A. Alcúson, P. Xanthopoulos, G. G. Plunk, P. Helander, F. Wilms, Y. Turkin, A. Von Stechow, and O. Grulke. Suppression of electrostatic micro-instabilities in maximum-J stellarators. *Plasma Physics and Controlled Fusion*, 62(3):035005, 1 2020.
- ¹⁸J.H.E. Proll, G.G. Plunk, B.J. Faber, T. Görler, P. Helander, I.J. McKinney, M.J. Pueschel, H.M. Smith, and P. Xanthopoulos. Turbulence mitigation in maximum-J stellarators with electron-density gradient. *Journal of Plasma Physics*, 88(1):905880112, 2 2022.
- ¹⁹E. A. Belli, G. W. Hammett, and W. Dorland. Effects of plasma shaping on nonlinear gyrokinetic turbulence. *Physics of Plasmas*, 15(9), 9 2008.
- ²⁰Motoki Nakata, Akinobu Matsuyama, Nobuyuki Aiba, Shinya Maeyama, Masanori Nunami, and Tomo-Hiko Watanabe. Local Gyrokinetic Vlasov Simulations with Realistic Tokamak MHD Equilibria. *Plasma and Fusion Research*, 9(0):1403029–1403029, 2014.
- ²¹M C L Morren, J H E Proll, J van Dijk, and M J Pueschel. Influence of collisions on trapped-electron modes in tokamaks and low-shear stellarators. *Physics of Plasmas*, 31(5):052508, 5 2024.
- ²²H. E. Mynick, P. Xanthopoulos, and A. H. Boozer. Geometry dependence of stellarator turbulence. *Physics of Plasmas*, 16(11):110702, 11 2009.
- ²³Matt Landreman, Jong Youl Choi, Caio Alves, Prasanna Balaprakash, Michael Churchill, Rory Conlin, and Gareth Roberg-Clark. How does ion temperature gradient turbulence depend on magnetic geometry? Insights from data and machine learning. *Journal of Plasma Physics*, 91(4):E120, 8 2025.
- ²⁴J. C. Adam, W. M. Tang, and P. H. Rutherford. Destabilization of the trapped-electron mode by magnetic curvature drift resonances. *Physics of Fluids*, 19(4):561–566, 4 1976.
- ²⁵J. H.E. Proll, P. Helander, J. W. Connor, and G. G. Plunk. Resilience of Quasi-Isodynamic Stellarators against Trapped-Particle Instabilities. *Physical Review Letters*, 108(24):245002, 6 2012.
- ²⁶Marshall N. Rosenbluth. Low-Frequency Limit of Interchange Instability. *Physics of Fluids*, 11(4):869–872, 4 1968.
- ²⁷Alan G. Goodman, Pavlos Xanthopoulos, Gabriel G. Plunk, Håkan Smith, Carolin Nührenberg, Craig D. Beidler, Sophia A. Henneberg, Gareth Roberg-Clark, Michael Drevlak, and Per Helander. Quasi-Isodynamic Stellarators with Low Turbulence as Fusion Reactor Candidates. *PRX Energy*, 3(2):023010, 6 2024.
- ²⁸Katia Camacho Mata, Gabriel G. Plunk, and Rogerio Jorge. Direct construction of stellarator-symmetric quasi-isodynamic magnetic configurations. *Journal of Plasma Physics*, 88(5):905880503, 10 2022.
- ²⁹E. Sánchez, J.L. Velasco, I. Calvo, and S. Mulas. A quasi-isodynamic configuration with good confinement of fast ions at low plasma β . *Nuclear Fusion*, 63(6):066037, 6 2023.
- ³⁰Wei Wang, Kenji Imadera, Haruki Seto, and Masatoshi Yagi. Global gyrokinetic study of magnetic shaping effects on linear trapped electron mode instability in normal/reversed magnetic shear plasmas. *Nuclear Fusion*, 62(11):112006, 11 2022.
- ³¹M. J. Gerard, M. J. Pueschel, B. Geiger, R. J. J. Mackenbach, J. M. Duff, B. J. Faber, C. C. Hegna, and P. W. Terry. On the effect of flux-surface shaping on trapped-electron modes in quasi-helically symmetric stellarators. *Physics of Plasmas*, 31(5), 5 2024.
- ³²E. Rodríguez, P. Helander, and A.G. Goodman. The maximum- $\langle i \rangle$ property in quasi-isodynamic stellarators. *Journal of Plasma Physics*, 90(2):905900212, 4 2024.
- ³³G. G. Plunk, P. Helander, P. Xanthopoulos, and J. W. Connor. Collisionless microinstabilities in stellarators. III. The ion-temperature-gradient mode. *Physics of Plasmas*, 21(3):032112, 3 2014.

- ³⁴E. Rodríguez and A. Zocco. The kinetic ion-temperature-gradient-driven instability and its localisation. *Journal of Plasma Physics*, 91(1):E21, 2 2025.
- ³⁵J H E Proll, H E Mynick, P Xanthopoulos, S A Lazerson, and B J Faber. TEM turbulence optimisation in stellarators. *Plasma Physics and Controlled Fusion*, 58(1):014006, 1 2016.
- ³⁶H E Mynick, N Pomphrey, and P Xanthopoulos. Optimizing Stellarators for Turbulent Transport. *Physical Review Letters*, 105(9):95004, 8 2010.
- ³⁷J.M. Duff, B.J. Faber, C.C. Hegna, M.J. Pueschel, and P.W. Terry. Suppressing trapped-electron-mode-driven turbulence via optimization of three-dimensional shaping. *Nuclear Fusion*, 65(4):046020, 4 2025.
- ³⁸H Mynick, P Xanthopoulos, B Faber, M Lucia, M Rorvig, and J N Talmadge. Turbulent optimization of toroidal configurations. *Plasma Physics and Controlled Fusion*, 56(9):094001, 9 2014.
- ³⁹G. T. Roberg-Clark, G. G. Plunk, P. Xanthopoulos, C. Nührenberg, S. A. Henneberg, and H. M. Smith. Critical gradient turbulence optimization toward a compact stellarator reactor concept. *Physical Review Research*, 5(3):L032030, 9 2023.
- ⁴⁰R. Jorge, W. Dorland, P. Kim, M. Landreman, N. R. Mandell, G. Merlo, and T. Qian. Direct microstability optimization of stellarator devices. *Physical Review E*, 110(3):035201, 9 2024.
- ⁴¹P. Kim, S. Buller, R. Conlin, W. Dorland, D.W. Dudt, R. Gaur, R. Jorge, E. Kolemen, M. Landreman, N.R. Mandell, and D. Panici. Optimization of nonlinear turbulence in stellarators. *Journal of Plasma Physics*, 90(2):905900210, 4 2024.
- ⁴²P.G. Ivanov and T. Adkins. An analytical form of the dispersion function for local linear gyrokinetics in a curved magnetic field. *Journal of Plasma Physics*, 89(2):905890213, 4 2023.
- ⁴³A. Zocco, P. Xanthopoulos, H. Doerk, J. W. Connor, and P. Helander. Threshold for the destabilisation of the ion-temperature-gradient mode in magnetically confined toroidal plasmas. *Journal of Plasma Physics*, 84(1):715840101, 2 2018.
- ⁴⁴H. Biglari, P. H. Diamond, and M. N. Rosenbluth. Toroidal ion-pressure-gradient-driven drift instabilities and transport revisited. *Physics of Fluids B: Plasma Physics*, 1(1):109, 6 1998.
- ⁴⁵Ivan Calvo, Felix I. Parra, Hanne Thienpondt, and Jose Manuel Garcia-Regaña. Modification of ion-temperature-gradient turbulence by impurities in stellarator plasmas. 10 2025.
- ⁴⁶A. Zocco, G. G. Plunk, P. Xanthopoulos, and P. Helander. Geometric stabilization of the electrostatic ion-temperature-gradient driven instability. I. Nearly axisymmetric systems. *Physics of Plasmas*, 23(8), 8 2016.
- ⁴⁷P. Helander and G.G. Plunk. The universal instability in general geometry. *Physics of Plasmas*, 22(9):090706, 9 2015.
- ⁴⁸P. Helander, J. H. E. Proll, and G.G. Plunk. Collisionless microinstabilities in stellarators. I. Analytical theory of trapped-particle modes. *Physics of Plasmas*, 20(12):122505, 12 2013.
- ⁴⁹G. G. Plunk, J. W. Connor, and P. Helander. Collisionless microinstabilities in stellarators. Part 4. The ion-driven trapped-electron mode. *Journal of Plasma Physics*, 83(4), 8 2017.
- ⁵⁰In order for a gyrokinetic treatment to be sensible $\omega/\Omega_s \ll 1$ and $k_\perp \rho_{Ts} \sim \mathcal{O}(1)$ need to be respected by each species s , otherwise requiring a fully kinetic description. Additionally, we have assumed $\omega_{ts}/\omega \ll 1$ for the approximate treatment of the non-adiabatic part of the impurity distribution in Eqn. (7) with index $i \rightarrow s$. As we assume these requirements to be met by the main (hydrogenic) ion species, and $\Omega_s = (Z_s m_i/m_s)\Omega_i$, $\rho_{Ts} = (\sqrt{T_s/T_i} \sqrt{m_s/m_i/Z_s})\rho_{Ti}$, $\omega_{ts} = \sqrt{T_s/T_i} \sqrt{m_i/m_s} \omega_{ti}$, it follows that the treatment of impurities is only potentially limited by the $\omega/\Omega_s \ll 1$ assumption, as the mass of the impurity species increases faster than the ionisation state.
- ⁵¹B. B. Kadomtsev and O. P. Pogutse. Turbulence in Toroidal Systems. In M A Leontovich, editor, *Reviews of Plasma Physics*, pages 249–400. Springer US, Boston, MA, 1970.
- ⁵²W. Horton, B. G. Hong, and W. M. Tang. Toroidal electron temperature gradient driven drift modes. *Physics of Fluids*, 31(10):2971–2983, 10 1988.
- ⁵³Chuan Sheng Liu. Instabilities in a Magnetoplasma with Skin Current. *Physical Review Letters*, 27(24):1637–1640, 12 1971.
- ⁵⁴Y. C. Lee, J. Q. Dong, P. N. Guzdar, and C. S. Liu. Collisionless electron temperature gradient instability. *Physics of Fluids*, 30(5):1331–1339, 5 1987.
- ⁵⁵A. Hirose. Electron temperature gradient modes in tokamaks. *Physics of Fluids B: Plasma Physics*, 2(4):850–853, 4 1990.
- ⁵⁶Matt Landreman, Thomas M. Antonsen, and William Dorland. Universal instability for wavelengths below the ion Larmor scale. *Physical Review Letters*, 114(9):095003, 3 2015.
- ⁵⁷P. Costello, J.H.E. Proll, G.G. Plunk, M.J. Pueschel, and J.A. Alcusón. The universal instability in optimised stellarators. *Journal of Plasma Physics*, 89(4):905890402, 8 2023.
- ⁵⁸J L Luxon. A design retrospective of the DIII-D tokamak. *Nuclear Fusion*, 42(5):614, 5 2002.
- ⁵⁹F Hofmann, J B Lister, W Anton, S Barry, R Behn, S Bernel, G Besson, F Buhlmann, R Chavan, M Corboz, M J Dutch, B P Duval, D Fasel, A Favre, S Franke, A Heym, A Hirt, C Hollenstein, P Isoz, B Joye, X Llobet, J C Magnin, B Marletaz, P Marmillod, Y Martin, J M Mayor, J M Moret, C Nieswand, P J Paris, A Perez, Z A Pietrzyk, R A Pitts, A Pochelon, R Rage, O Sauter, G Tonetti, M Q Tran, F Troyon, D J Ward, and H Weisen. Creation and control of variably shaped plasmas in TCV. *Plasma Physics and Controlled Fusion*, 36(12B):B277–B287, 12 1994.
- ⁶⁰F. Simon B. Anderson, Abdulgader F. Almagri, David T. Anderson, Peter G. Matthews, Joseph N. Talmadge, and J. Leon Shohet. The Helically Symmetric Experiment, (HSX) Goals, Design and Status. *Fusion Technology*, 27(3T):273–277, 4 1995.
- ⁶¹Craig Beidler, Günter Grieger, Franz Herrnegger, Ewald Harmeyer, Johann Kisslinger, Wolf Lotz, Henning Maassberg, Peter Merkel, Jürgen Nührenberg, Fritz Rau, Jörg Sapper, Francesco Sardei, Ruben Scardovelli, Arnulf Schlüter, and Horst Wobig. Physics and Engineering Design for Wendelstein VII-X. *Fusion Technology*, 17(1):148–168, 1 1990.
- ⁶²E A Belli and J Candy. Implications of advanced collision operators for gyrokinetic simulation. *Plasma Physics and Controlled Fusion*, 59(4):045005, 2 2017.
- ⁶³J. W. Connor, R. J. Hastie, and J. B. Taylor. Shear, Periodicity, and Plasma Ballooning Modes. *Physical Review Letters*, 40(6):396, 2 1978.
- ⁶⁴R. L. Dewar and A. H. Glasser. Ballooning mode spectrum in general toroidal systems. *Physics of Fluids*, 26(10):3038–3052, 10 1983.
- ⁶⁵J. Candy, R. E. Waltz, and M. N. Rosenbluth. Smoothness of turbulent transport across a minimum- $\langle \mathbf{q} \cdot \mathbf{i} \rangle$ surface. *Physics of Plasmas*, 11(5):1879–1890, 5 2004.
- ⁶⁶Gregory G. Howes, Steven C. Cowley, William Dorland, Gregory W. Hammett, Eliot Quataert, and Alexander A. Schekochihin. Astrophysical Gyrokinetics: Basic Equations and Linear Theory. *The Astrophysical Journal*, 651(1):590–614, 11 2006.
- ⁶⁷J B Taylor and R J Hastie. Stability of general plasma equilibria - I formal theory. *Plasma Physics*, 10(5):479–494, 1 1968.
- ⁶⁸J W Connor, R J Hastie, and J B Taylor. Stability of general plasma equilibria. III. *Plasma Physics*, 22(7):757–769, 7 1980.
- ⁶⁹F. Romanelli. Ion temperature-gradient-driven modes and anomalous ion transport in tokamaks. *Physics of Fluids B: Plasma Physics*, 1(5):1018–1025, 5 1989.
- ⁷⁰P. Terry, W. Anderson, and W. Horton. Kinetic effects on the toroidal ion pressure gradient drift mode. *Nuclear Fusion*, 22(4):487–497, 4 1982.
- ⁷¹S. C. Cowley, R. M. Kulsrud, and R. Sudan. Considerations of ion-temperature-gradient-driven turbulence. *Physics of Fluids B: Plasma Physics*, 3(10):2767, 6 1998.
- ⁷²N. Dominguez, B. A. Carreras, V. E. Lynch, and P. H. Diamond. Dissipative trapped electron modes in $l=2$ torsatrons. *Physics of Fluids B: Plasma Physics*, 4(9):2894, 9 1992.
- ⁷³B. J. Faber, M. J. Pueschel, J. H.E. Proll, P. Xanthopoulos, P. W. Terry, C. C. Hegna, G. M. Weir, K. M. Likin, and J. N. Talmadge. Gyrokinetic studies of trapped electron mode turbulence in the Helically Symmetric eXperiment stellarator. *Physics of Plasmas*, 22(7):072305, 7 2015.
- ⁷⁴Tilman Dannert and Frank Jenko. Gyrokinetic simulation of collisionless trapped-electron mode turbulence. *Physics of Plasmas*, 12(7):072309, 7 2005.
- ⁷⁵J. M. García-Regaña, M. Barnes, I. Calvo, F. I. Parra, J. A. Alcusón, R. Davies, A. González-Jerez, A. Mollén, E. Sánchez, J. L. Velasco, and A. Zocco. Turbulent impurity transport simulations in Wendelstein 7-X plasmas. *Journal of Plasma Physics*, 87(1):855870103, 2 2021.
- ⁷⁶T. S. Hahm and W. M. Tang. Nonlinear theory of collisionless trapped ion modes. *Physics of Plasmas*, 3(1):242–247, 1 1996.
- ⁷⁷William Denis D’haeseleer, William Nicholas Guy Hitchon, James D. Callen, and J. Leon Shohet. *Flux Coordinates and Magnetic Field Struc-*

- ture. Springer Berlin Heidelberg, Berlin, Heidelberg, 1 edition, 1991.
- ⁷⁸L.D. Landau. ON THE VIBRATIONS OF THE ELECTRONIC PLASMA. In D. ter Haar, editor, *Collected Papers of L.D. Landau*, pages 445–460. Elsevier, 1 1965.
- ⁷⁹B J Frei, A C D Hoffmann, and P Ricci. Local gyrokinetic collisional theory of the ion-temperature gradient mode. *Journal of Plasma Physics*, 88(3):905880304, 2022.
- ⁸⁰Michael Alan Beer. *GYROFLUID MODELS OF TURBULENT TRANSPORT IN TOKAMAKS*. PhD thesis, Princeton University, 1 1995.
- ⁸¹Rahul Gaur, Rory Conlin, David Dickinson, Jason F. Parisi, Daniel Dudt, Dario Panici, Patrick Kim, Kaya Unalmis, William D. Dorland, and Egemen Kolemen. Omnigenous stellarator equilibria with enhanced stability. 10 2024.
- ⁸²Jason F. Parisi, Felix I. Parra, Colin M. Roach, Carine Giroud, William Dorland, David R. Hatch, Michael Barnes, Jon C. Hillesheim, Nobuyuki Aiba, Justin Ball, Plamen G. Ivanov, and JET contributors. Toroidal and slab ETG instability dominance in the linear spectrum of JET-ILW pedestals. *Nuclear Fusion*, 60(12):126045, 12 2020.
- ⁸³Milton Abramowitz and Irene A Stegun. *Handbook of mathematical functions with formulas, graphs, and mathematical tables*, volume 55. US Government printing office, Washington D.C., 1968.
- ⁸⁴L. Podavini, P. Helander, G.G. Plunk, and A. Zocco. Energetic bounds on gyrokinetic instabilities. Part 5. Contrasting optimal and normal modes over the geometric landscape. *Journal of Plasma Physics*, 91(3):E79, 6 2025.
- ⁸⁵Burton D. Fried and Samuel D. Conte. *The Plasma Dispersion Function*. Academic Press, New York, 1961.
- ⁸⁶Ö. Gültekin and Ö. D. Gürcan. Generalized curvature modified plasma dispersion functions and Dupree renormalization of toroidal ITG. *Plasma Physics and Controlled Fusion*, 62(2):025018, 2 2020.
- ⁸⁷Ö.D. Gürcan. Numerical computation of the modified plasma dispersion function with curvature. *Journal of Computational Physics*, 269:156–167, 7 2014.
- ⁸⁸D R Hatch, P W Terry, F Jenko, F Merz, and W M Nevins. Saturation of Gyrokinetic Turbulence through Damped Eigenmodes. *Physical Review Letters*, 106(11):115003, 3 2011.
- ⁸⁹M. J. Pueschel, B. J. Faber, J. Citrin, C. C. Hegna, P. W. Terry, and D. R. Hatch. Stellarator Turbulence: Subdominant Eigenmodes and Quasilinear Modeling. *Physical Review Letters*, 116(8):085001, 2 2016.
- ⁹⁰X. Garbet, P. Donnel, L. De Gianni, Z. Qu, Y. Melka, Y. Sarazin, V. Grandgirard, K. Obrejan, E. Bourne, and G. Dif-Pradalier. The effect of shaping on trapped electron mode stability: an analytical model. *Nuclear Fusion*, 64(10):106055, 10 2024.
- ⁹¹Zhe Gao, H. Sanuki, K. Itoh, and J. Q. Dong. Short wavelength ion temperature gradient instability in toroidal plasmas. *Physics of Plasmas*, 12(2), 2 2005.
- ⁹²Hua-sheng Xie and Bo Li. Global theory to understand toroidal drift waves in steep gradient. *Physics of Plasmas*, 23(8), 8 2016.
- ⁹³Matt Landreman and Peter J. Catto. Omnigenity as generalized quasisymmetry. *Physics of Plasmas*, 19(5):56103, 5 2012.
- ⁹⁴John R Cary and Svetlana G Shasharina. Omnigenity and quasihelicity in helical plasma confinement systems. *Physics of Plasmas*, 4(9):3323–3333, 9 1997.
- ⁹⁵R. E. Waltz and A. H. Boozer. Local shear in general magnetic stellarator geometry. *Physics of Fluids B: Plasma Physics*, 5(7):2201, 6 1993.
- ⁹⁶T. Rafiq and C. C. Hegna. Dissipative trapped-electron instability in quasihelically symmetric stellarators. *Physics of Plasmas*, 13(6):062501, 6 2006.
- ⁹⁷R J Hastie and J B Taylor. Stability theory of general plasma equilibria. II. Multipoles. *Plasma Physics*, 13(4):265–288, 4 1971.
- ⁹⁸F. Y. Gang, P. H. Diamond, and M. N. Rosenbluth. A kinetic theory of trapped-electron-driven drift wave turbulence in a sheared magnetic field. *Physics of Fluids B: Plasma Physics*, 3(1):68, 6 1991.
- ⁹⁹P.G. Ivanov, P. Luhadiya, T. Adkins, and A.A. Schekochihin. The gyrokinetic field invariant and electromagnetic temperature-gradient instabilities in ‘good-curvature’ plasmas. *Journal of Plasma Physics*, 91(4):E95, 8 2025.
- ¹⁰⁰P. Helander and G. G. Plunk. Energetic bounds on gyrokinetic instabilities. Part I. Fundamentals. *Journal of Plasma Physics*, 88(2):905880207, 12 2022.
- ¹⁰¹G.G. Plunk and P. Helander. Energetic bounds on gyrokinetic instabilities. Part 2. Modes of optimal growth. *Journal of Plasma Physics*, 88(3):905880313, 6 2022.
- ¹⁰²B. Coppi and F. Pegoraro. Theory of the ubiquitous mode. *Nuclear Fusion*, 17(5):969, 10 1977.
- ¹⁰³X. Garbet, L. Laurent, F. Mourgues, J.P. Roubin, and A. Samain. Variational calculation of electromagnetic instabilities in tokamaks. *Journal of Computational Physics*, 87(2):249–269, 4 1990.
- ¹⁰⁴Ksenia Aleynikova and Alessandro Zocco. Quantitative study of kinetic ballooning mode theory in simple geometry. *Physics of Plasmas*, 24(9):092106, 8 2017.
- ¹⁰⁵C. Bourdelle, J. Citrin, B. Baiocchi, A. Casati, P. Cottier, X. Garbet, and F. Imbeaux. Core turbulent transport in tokamak plasmas: bridging theory and experiment with QuaLiKiz. *Plasma Physics and Controlled Fusion*, 58(1):014036, 11 2015.
- ¹⁰⁶C Bourdelle, X Garbet, F Imbeaux, A Casati, N Dubuit, R Guirlet, and T Parisot. A new gyrokinetic quasilinear transport model applied to particle transport in tokamak plasmas. *Physics of Plasmas*, 14(11):112501, 11 2007.
- ¹⁰⁷Cole Darin Stephens and Ping-Yu Li. A Ritz variational principle for local collisionless gyrokinetic instabilities. *Journal of Plasma Physics*, 91(4):E124, 8 2025.
- ¹⁰⁸Katsuhisa Ohta. Time-dependent variational principle with constraints. *Chemical Physics Letters*, 329(3-4):248–254, 10 2000.
- ¹⁰⁹Heinz Jürgen Wagner. Schrödinger quantization and variational principles in dissipative quantum theory. *Zeitschrift für Physik B*, 95(2):261–273, 6 1994.
- ¹¹⁰Ángel S. Sanz and Salvador Miret-Artés. *A Trajectory Description of Quantum Processes. I. Fundamentals*. Lecture Notes in Physics. Springer Berlin Heidelberg, Berlin, Heidelberg, 1 edition, 2012.
- ¹¹¹M. A. Beer, S. C. Cowley, and G. W. Hammett. Field-aligned coordinates for nonlinear simulations of tokamak turbulence. *Physics of Plasmas*, 2(7):2687–2700, 7 1995.
- ¹¹²Mike F. Martin, Matt Landreman, Pavlos Xanthopoulos, Noah R. Mandell, and William Dorland. The Parallel Boundary Condition for Turbulence Simulations in Low Magnetic Shear Devices. *Plasma Physics and Controlled Fusion*, 60(9):095008, 3 2018.
- ¹¹³B. J. Faber, M. J. Pueschel, P. W. Terry, C. C. Hegna, and J. E. Roman. Stellarator microinstabilities and turbulence at low magnetic shear. *Journal of Plasma Physics*, 84(5):905840503, 10 2018.
- ¹¹⁴P. Xanthopoulos and F. Jenko. Clebsch-type coordinates for nonlinear gyrokinetics in generic toroidal configurations. *Physics of Plasmas*, 13(9):092301, 9 2006.
- ¹¹⁵P. Xanthopoulos, W. A. Cooper, F. Jenko, Yu Turkin, A. Runov, and J. Geiger. A geometry interface for gyrokinetic microturbulence investigations in toroidal configurations. *Physics of Plasmas*, 16(8):082303, 8 2009.
- ¹¹⁶T. Görler, X. Lapillonne, S. Brunner, T. Dannert, F. Jenko, F. Merz, and D. Told. The global version of the gyrokinetic turbulence code GENE. *Journal of Computational Physics*, 230(18):7053–7071, 8 2011.
- ¹¹⁷Per Helander. Theory of plasma confinement in non-axisymmetric magnetic fields. *Reports on Progress in Physics*, 77(8):087001, 8 2014.
- ¹¹⁸E. Sánchez, J. M. García-Regana, A. Banón Navarro, J. H.E. Proll, C. Mora Moreno, A. González-Jerez, I. Calvo, R. Kleiber, J. Riemann, J. Smoniewski, M. Barnes, and F. I. Parra. Gyrokinetic simulations in stellarators using different computational domains. *Nuclear Fusion*, 61(11):116074, 10 2021.
- ¹¹⁹J. H. E. Proll, P. Xanthopoulos, and P. Helander. Collisionless microinstabilities in stellarators. II. Numerical simulations. *Physics of Plasmas*, 20(12):122506, 12 2013.
- ¹²⁰A Marinoni, S Brunner, Y Camenen, S Coda, J P Graves, X Lapillonne, A Pochelon, O Sauter, and L Villard. The effect of plasma triangularity on turbulent transport: modeling TCV experiments by linear and nonlinear gyrokinetic simulations. *Plasma Physics and Controlled Fusion*, 51(5):055016, 5 2009.
- ¹²¹G Merlo, S Brunner, O Sauter, Y Camenen, T Görler, F Jenko, A Marinoni, D Told, and L Villard. Investigating profile stiffness and critical gradients in shaped TCV discharges using local gyrokinetic simulations of turbulent transport. *Plasma Physics and Controlled Fusion*, 57(5):054010, 5 2015.
- ¹²²Clemente Angioni. Impurity transport in tokamak plasmas, theory, modelling and comparison with experiments. *Plasma Physics and Controlled Fusion*, 63(7):073001, 7 2021.
- ¹²³J. M. García-Regaña, I. Calvo, F.I. Parra, and H. Thienpondt. Reduction or Enhancement of Stellarator Turbulence by Impurities. *Physical Review Letters*, 133(10):105101, 9 2024.

- ¹²⁴A. Mariani, S. Brunner, J. Dominski, A. Merle, G. Merlo, O. Sauter, T. Görler, F. Jenko, and D. Told. Identifying microturbulence regimes in a TCX discharge making use of physical constraints on particle and heat fluxes. *Physics of Plasmas*, 25(1), 1 2018.
- ¹²⁵T. Romba, F. Reimold, R. J. E. Jaspers, A. J. Edmondson, O. P. Ford, B. Geiger, S. Jabłowski, M. Kubkowska, T. W. C. Neelis, P. Zs. Poloskei, L. Vanó, and T. Klinger. Evaluation and validation of radial impurity density profiles from CXRS using neutral beam modelling in W7-X. *Plasma Physics and Controlled Fusion*, 65(7):075011, 7 2023.
- ¹²⁶B. A. Grierson, G. M. Staebler, W. M. Solomon, G. R. McKee, C. Holland, M. Austin, A. Marinoni, L. Schmitz, R. I. Pinsker, and DIII-D Team. Multi-scale transport in the DIII-D ITER baseline scenario with direct electron heating and projection to ITER. *Physics of Plasmas*, 25(2):022509, 2 2018.
- ¹²⁷R. C. Wolf, A. Alonso, S. Äkäslopola, J. Baldzuhn, M. Beurskens, C. D. Beidler, C. Biedermann, H. S. Bosch, S. Bozhakov, R. Brakel, H. Braune, S. Brezinsek, K. J. Brunner, H. Damm, A. Dinklage, P. Drewelow, F. Effenberg, Y. Feng, O. Ford, G. Fuchert, Y. Gao, J. Geiger, O. Grulke, N. Harder, D. Hartmann, P. Helander, B. Heinemann, M. Hirsch, U. Höfel, C. Hopf, K. Ida, M. Isobe, M. W. Jakubowski, Y. O. Kazakov, C. Killer, T. Klinger, J. Knauer, R. König, M. Krychowiak, A. Langenberg, H. P. Laqua, S. Lazerson, P. McNeely, S. Marsen, N. Marushchenko, R. Nocentini, K. Ogawa, G. Orozco, M. Osakabe, M. Otte, N. Pablant, E. Pasch, A. Pavone, M. Porkolab, A. Puig Sitjes, K. Rahbarnia, R. Riedl, N. Rust, E. Scott, J. Schilling, R. Schroeder, T. Stange, A. Von Stechow, E. Strumberger, T. Sunn Pedersen, J. Svensson, H. Thomson, Y. Turkin, L. Vano, T. Wauters, G. Wurden, M. Yoshinuma, M. Zanini, D. Zhang, and Wendelstein 7-X team. Performance of Wendelstein 7-X stellarator plasmas during the first divertor operation phase. *Physics of Plasmas*, 26(8):082504, 8 2019.
- ¹²⁸M. Siccino, W. Biel, M. Cavedon, E. Fable, G. Federici, F. Janky, H. Lux, F. Maviglia, J. Morris, F. Palermo, O. Sauter, F. Subba, and H. Zohm. DEMO physics challenges beyond ITER. *Fusion Engineering and Design*, 156:111603, 7 2020.
- ¹²⁹M. Siccino, J. P. Graves, R. Kembleton, H. Lux, F. Maviglia, A. W. Morris, J. Morris, and H. Zohm. Development of the plasma scenario for EU-DEMO: Status and plans. *Fusion Engineering and Design*, 176:113047, 3 2022.
- ¹³⁰P. Manas, Y. Camenen, S. Benkadda, H. Weisen, C. Angioni, F. J. Casson, C. Giroud, M. Gelfusa, and M. Maslov. Gyrokinetic modeling of impurity peaking in JET H-mode plasmas. *Physics of Plasmas*, 24(6), 6 2017.
- ¹³¹K. Ida, M. Yoshinuma, M. Osakabe, K. Nagaoka, M. Yokoyama, H. Funaba, C. Suzuki, T. Ido, A. Shimizu, I. Murakami, N. Tamura, H. Kasahara, Y. Takeiri, K. Ikeda, K. Tsumori, O. Kaneko, S. Morita, M. Goto, K. Tanaka, K. Narihara, T. Minami, and I. Yamada. Observation of an impurity hole in a plasma with an ion internal transport barrier in the Large Helical Device. *Physics of Plasmas*, 16(5), 5 2009.
- ¹³²J. M. Duff, B. J. J. Faber, C. C. Hegna, M. J. Pueschel, and P. W. Terry. Effect of triangularity on ion-temperature-gradient-driven turbulence. *Physics of Plasmas*, 29(1), 1 2022.
- ¹³³C. D. Stephens, X. Garbet, J. Citrin, C. Bourdelle, K. L. van de Plassche, and F. Jenko. Quasilinear gyrokinetic theory: a derivation of QuaLiKiz. *Journal of Plasma Physics*, 87(4):905870409, 8 2021.
- ¹³⁴R. J. J. Mackenbach, J. M. Duff, M. J. Gerard, J. H. E. Proll, P. Helander, and C. C. Hegna. Bounce-averaged drifts: Equivalent definitions, numerical implementations, and example cases. *Physics of Plasmas*, 30(9):093901, 9 2023.
- ¹³⁵C. G. Broyden. A class of methods for solving nonlinear simultaneous equations. *Mathematics of Computation*, 19(92):577–593, 1965.
- ¹³⁶C. G. Broyden. On the discovery of the "good Broyden" method. *Mathematical Programming*, 87(2):209–213, 4 2000.
- ¹³⁷Larry Armijo. Minimization of functions having Lipschitz continuous first partial derivatives. *Pacific Journal of Mathematics*, 16(1):1–3, 1 1966.
- ¹³⁸J. J. Moré and J. A. Trangenstein. On the global convergence of Broyden's method. *Mathematics of Computation*, 30(135):523–540, 1976.
- ¹³⁹Toon Demeester, Nicolas Delaissé, E. Harald van Brummelen, Rob Haelterman, and Joris Degroote. On the effect of nonlinearity and Jacobian initialization on the convergence of the generalized Broyden quasi-Newton method. *International Journal for Numerical Methods in Engineering*, 123(17), 2022.
- ¹⁴⁰D. W. Decker and C. T. Kelley. BROYDEN'S METHOD FOR A CLASS OF PROBLEMS HAVING SINGULAR JACOBIAN AT THE ROOT. *SIAM Journal on Numerical Analysis*, 22(3), 1985.
- ¹⁴¹A. G. Goodman, K. Camacho Mata, S. A. Henneberg, R. Jorge, M. Landreman, G. G. Plunk, H. M. Smith, R. J. J. Mackenbach, C. D. Beidler, and P. Helander. Constructing precisely quasi-isodynamic magnetic fields. *Journal of Plasma Physics*, 89(5):905890504, 10 2023.
- ¹⁴²It should be noted that HSX was designed and constructed at the turn of the millennium, while through advancements in optimisation techniques in recent years magnetic fields achieving significantly higher degree of quasi-symmetry can be achieved^{145–148}. Likewise for W7-X, magnetic fields with much higher degree of quasi-isodynamicity and maximum-J-ness even at low β can be constructed through modern optimisation targets^{28,29,141}.
- ¹⁴³Jürgen Nührenberg. Development of quasi-isodynamic stellarators. *Plasma Physics and Controlled Fusion*, 52(12):124003, 11 2010.
- ¹⁴⁴A. A. Subbotin, M. I. Mikhailov, V. D. Shafranov, M. Yu. Isaev, C. Nührenberg, J. Nührenberg, R. Zille, V. V. Nemov, S. V. Kasilov, V. N. Kalyuzhnyj, and W. A. Cooper. Integrated physics optimization of a quasi-isodynamic stellarator with poloidally closed contours of the magnetic field strength. *Nuclear Fusion*, 46(11):921–927, 11 2006.
- ¹⁴⁵Matt Landreman and Elizabeth Paul. Magnetic Fields with Precise Quasisymmetry for Plasma Confinement. *Physical Review Letters*, 128(3):035001, 1 2022.
- ¹⁴⁶R. Jorge, W. Sengupta, and M. Landreman. Construction of quasisymmetric stellarators using a direct coordinate approach. *Nuclear Fusion*, 60(7):076021, 7 2020.
- ¹⁴⁷Andrew Giuliani. Direct stellarator coil design using global optimization: application to a comprehensive exploration of quasi-axisymmetric devices. *Journal of Plasma Physics*, 90(3):905900303, 6 2024.
- ¹⁴⁸Andrew Giuliani, Eduardo Rodríguez, and Marina Spivak. A comprehensive exploration of quasisymmetric stellarators and their coil sets. 4 2025.
- ¹⁴⁹In toroidal geometry the presence of the magnetic drifts provides another potential driving mechanism for UI modes, though the contribution from drift effects to the growth rate is much smaller^{57,150}.
- ¹⁵⁰J. Chowdhury, R. Ganesh, S. Brunner, J. Vaclavik, and L. Villard. Toroidal universal drift instability: A global gyrokinetic study. *Physics of Plasmas*, 17(10):102105, 10 2010.
- ¹⁵¹M. J. Pueschel, D. R. Hatch, D. R. Ernst, W. Guttenfelder, P. W. Terry, J. Citrin, and J. W. Connor. On microinstabilities and turbulence in steep-gradient regions of fusion devices. *Plasma Physics and Controlled Fusion*, 61(3):034002, 3 2019.
- ¹⁵²M. K. Han, Zheng-Xiong Wang, J. Q. Dong, and Huarong Du. Multiple ion temperature gradient driven modes in transport barriers. *Nuclear Fusion*, 57(4):046019, 4 2017.
- ¹⁵³Gabriele Merlo, Mattia Dicorato, Bryce Allen, Tilman Dannert, Kai Germaschewski, and Frank Jenko. On the effect of negative triangularity on ion temperature gradient turbulence in tokamaks. *Physics of Plasmas*, 30(10), 10 2023.
- ¹⁵⁴W. Dorland and G. W. Hammett. Gyrofluid turbulence models with kinetic effects. *Physics of Fluids B: Plasma Physics*, 5(3):812–835, 3 1993.
- ¹⁵⁵Donald B. Owen. Tables for Computing Bivariate Normal Probabilities. *The Annals of Mathematical Statistics*, 27(4), 1956.
- ¹⁵⁶C. Z. Cheng and K. T. Tsang. Electrostatic drift wave eigenmodes in tokamaks. *Nuclear Fusion*, 21(6):643–650, 6 1981.
- ¹⁵⁷C. Z. Cheng. Kinetic theory of collisionless ballooning modes. *Physics of Fluids*, 25(6):1020–1026, 6 1982.
- ¹⁵⁸J. W. Connor, R. J. Hastie, and P. Helander. Stability of the trapped electron mode in steep density and temperature gradients. *Plasma Physics and Controlled Fusion*, 48(6):885, 5 2006.
- ¹⁵⁹Wendell Horton, Duk-In Choi, and W. M. Tang. Toroidal drift modes driven by ion pressure gradients. *Physics of Fluids*, 24(6):1077–1085, 6 1981.
- ¹⁶⁰G. Rewoldt, W. M. Tang, and M. S. Chance. Electromagnetic kinetic toroidal eigenmodes for general magnetohydrodynamic equilibria. *Physics of Fluids*, 25(3):480–490, 3 1982.
- ¹⁶¹C. Bourdelle, X. Garbet, G. T. Hoang, J. Ongena, and R. V. Budny. Stability analysis of improved confinement discharges: internal transport barriers in Tore Supra and radiative improved mode in TEXTOR. *Nuclear Fusion*, 42(7):312, 7 2002.
- ¹⁶²J. Citrin, C. Bourdelle, F. J. Casson, C. Angioni, N. Bonanomi, Y. Camenen, X. Garbet, L. Garzotti, T. Görler, Ö. Gürcan, F. Koechl, F. Imbeaux, O. Linder, K. van de Plassche, P. Strand, and G. Szepesi. Tractable flux-

driven temperature, density, and rotation profile evolution with the quasilinear gyrokinetic transport model QuaLiKiz. *Plasma Physics and Controlled Fusion*, 59(12):124005, 11 2017.

¹⁶³A Najlaoui, Y Camenen, C Bourdelle, and A Loarte. Verifying turbulence model reduction in high β tokamak plasmas. *Plasma Physics and Controlled Fusion*, 67(4):045016, 4 2025.

¹⁶⁴S C Guo, L Chen, S T Tsai, and P N Guzdar. Ion temperature gradient instability and anomalous transport. *Plasma Physics and Controlled Fusion*, 31(3):423–430, 3 1989.

¹⁶⁵A. Casati, C. Bourdelle, X. Garbet, F. Imbeaux, J. Candy, F. Clairet, G. Dif-Pradalier, G. Falchetto, T. Gerbaud, V. Grandgirard, Ö.D. Gürcan, P. Hennequin, J. Kinsey, M. Ottaviani, R. Sabot, Y. Sarazin, L. Vermare, and R.E. Waltz. Validating a quasi-linear transport model versus nonlinear simulations. *Nuclear Fusion*, 49(8):085012, 8 2009.

¹⁶⁶H.G. Dudding, F.J. Casson, D. Dickinson, B.S. Patel, C.M. Roach, E.A. Belli, and G.M. Staebler. A new quasilinear saturation rule for tokamak turbulence with application to the isotope scaling of transport. *Nuclear Fusion*, 62(9):096005, 9 2022.

¹⁶⁷T. Xie, M. J. Pueschel, and D. R. Hatch. Quasilinear modeling of heat flux from microtearing turbulence. *Physics of Plasmas*, 27(8):082306, 8 2020.

¹⁶⁸Ellert van der Velden. CMasher: Scientific colormaps for making accessible, informative and 'cmashing' plots. *Journal of Open Source Software*, 5(46), 2020.

¹⁶⁹T G Northrop. Adiabatic Theory of Charged Particle Motion. In Billy M McCormac, editor, *Radiation Trapped in the Earth's Magnetic Field*, pages 26–44, Dordrecht, 1966. Springer Netherlands.

¹⁷⁰Hua-Sheng Xie. BO: A unified tool for plasma waves and instabilities analysis. *Computer Physics Communications*, 244:343–371, 11 2019.

¹⁷¹In regions where either $\omega_{j,\kappa}$ or $\omega_{j,\nabla B}$ is close to vanishing, there may even at modest β be a mismatch between the signs of the curvature and ∇B drifts. In such cases, however, the curvature or ∇B model (depending on which of the components is closest to vanishing) from Eqn. (29) is expected to provide an adequate approximation to the case of full toroidal drive by both components.

¹⁷²A. I. Smolyakov, M. Yagi, and Y. Kishimoto. Short Wavelength Temperature Gradient Driven Modes in Tokamak Plasmas. *Physical Review Letters*, 89(12):125005, 8 2002.

¹⁷³Joan Adler. Series Expansions. *Computers in Physics*, 8(3):287–295, 5 1994.

Supplementary Material for “Fast electrostatic microinstability evaluation in arbitrary toroidal magnetic geometry using a variational approach”

M.C.L. Morren,¹ P. Mulholland,¹ J.H.E. Prohl,^{1,2} M.J. Pueschel,^{1,3,4} L. Podavini,² D.D. Kiszkiel,¹ J.A. Schuurmans,¹ and A. Zocco²

¹*Department of Applied Physics and Science Education, Eindhoven University of Technology, 5600 MB Eindhoven, The Netherlands*

²*Max-Planck-Institut für Plasmaphysik, 17491 Greifswald, Germany*

³*Dutch Institute for Fundamental Energy Research, 5612 AJ Eindhoven, The Netherlands*

⁴*Department of Physics & Astronomy, Ruhr-Universität Bochum, 44780 Bochum, Germany*

(*Electronic mail: m.c.l.morren@tue.nl)

(Dated: 5 December 2025)

S1. EXTENDING THE FLUX-TUBE GEOMETRY INTO BALLOONING SPACE

When expressed in (normalised) Boozer coordinates (s, θ, ζ) , the metric tensor \underline{g}_B obeys the two-fold 2π physical periodicity of the torus, i.e. $g_B^{nm}(s, \theta, \zeta + 2\pi) = g_B^{nm}(s, \theta + 2\pi, \zeta) = g_B^{nm}(s, \theta, \zeta)$ for all components of the metric tensor. Using Eqn. (21) from the main text, the metric tensor for the flux-tube coordinate system \underline{g}_{FT} are obtained in terms of the Boozer system as

$$\begin{aligned} g_{FT}^{xx} &= \nabla x \cdot \nabla x \approx \frac{L_{ref}^2}{4s_0} g_B^{ss} \\ g_{FT}^{xy} &= \nabla x \cdot \nabla y \approx \frac{L_{ref}^2}{2} \left(g_B^{s\theta} - \frac{g_B^{s\zeta}}{q_0} + \frac{\theta g_B^{ss}}{q_0} \frac{dq}{ds} \Big|_{s=s_0} \right) \\ g_{FT}^{xz} &= \nabla x \cdot \nabla z \approx \frac{L_{ref}}{2\sqrt{s_0}} g_B^{s\theta} \\ g_{FT}^{yy} &= \nabla y \cdot \nabla y \approx L_{ref}^2 s_0 \left(g_B^{\theta\theta} + \frac{g_B^{\zeta\zeta} - 2q_0 g_B^{s\zeta}}{q_0^2} + \left(\frac{\theta}{q_0} \frac{dq}{ds} \Big|_{s=s_0} \right)^2 g_B^{ss} + \frac{2\theta (q_0 g_B^{s\theta} - q_B^{s\zeta})}{q_0^2} \frac{dq}{ds} \Big|_{s=s_0} \right) \\ g_{FT}^{yz} &= \nabla y \cdot \nabla z \approx L_{ref} \sqrt{s_0} \left(g_B^{\theta\theta} - \frac{g_B^{s\zeta}}{q_0} + \frac{\theta g_B^{s\theta}}{q_0} \frac{dq}{ds} \Big|_{s=s_0} \right) \\ g_{FT}^{zz} &= \nabla z \cdot \nabla z = g_B^{\theta\theta} \end{aligned} \quad (S1)$$

where the thin flux-tube approximation was invoked to neglect the small variation in s after evaluating the gradients, as the equilibrium quantities vary on radial scales comparable to the minor radius. Note that unlike the Boozer coordinate system, the metric tensor in the flux-tube coordinates no longer satisfies the two-fold 2π physical symmetry in the torus due to the secular terms in θ arising in $g_{FT}^{xy}, g_{FT}^{yy}, g_{FT}^{yz}$. As the secularity only arises in the field-aligned coordinate $z = \theta$, it follows that 2π periodicity is still preserved in the toroidal direction, i.e. $g_{FT}^{mn}(s_0, \theta, \zeta + 2\pi) = g_{FT}^{mn}(s_0, \theta, \zeta + 2\pi)$, though a $\theta \rightarrow \theta + 2\pi N_{pol}$ revolution now results into an interrelation

between the metric components

$$\begin{aligned} g_{FT}^{xy}(s_0, \theta + 2\pi N_{pol}, \zeta) &= g_{FT}^{xy}(s_0, \theta, \zeta) \\ &\quad + \frac{2s_0}{q_0} \frac{dq}{ds} \Big|_{s=s_0} 2\pi N_{pol} g_{FT}^{xx}(s_0, \theta, \zeta) \\ g_{FT}^{yy}(s_0, \theta + 2\pi N_{pol}, \zeta) &= g_{FT}^{yy}(s_0, \theta, \zeta) \\ &\quad + \frac{4s_0}{q_0} \frac{dq}{ds} \Big|_{s=s_0} 2\pi N_{pol} g_{FT}^{xy}(s_0, \theta, \zeta) \\ &\quad + \left(\frac{2s_0}{q_0} \frac{dq}{ds} \Big|_{s=s_0} \right)^2 (2\pi N_{pol})^2 g_{FT}^{xx}(s_0, \theta, \zeta) \\ g_{FT}^{yz}(s_0, \theta + 2\pi N_{pol}, \zeta) &= g_{FT}^{yz}(s_0, \theta, \zeta) \\ &\quad + \frac{2s_0}{q_0} \frac{dq}{ds} \Big|_{s=s_0} 2\pi N_{pol} g_{FT}^{xz}(s_0, \theta, \zeta) \end{aligned} \quad (S2)$$

which causes the secular terms to be experience a non-periodic upshift due to finite magnetic shear, whilst other metric components remain periodic in θ .

Since the remaining flux tube geometric quantities outlined in Section III A are all derived from \underline{g}_{FT} , they are also affected by the secularity. As shall be clear momentarily, it will suffice to investigate how the secularity of the metric seeps into the metric quantities $\gamma^1 = g_{FT}^{xx} g_{FT}^{yy} - (g_{FT}^{xy})^2$, $\gamma^2 = g_{FT}^{yz} g_{FT}^{xx} - g_{FT}^{xz} g_{FT}^{xy}$, $\gamma^3 = g_{FT}^{xz} g_{FT}^{yy} - g_{FT}^{xy} g_{FT}^{yz}$. Using Eqn. (S2) a little algebra yields

$$\begin{aligned} \gamma^1(s_0, \theta + 2\pi N_{pol}, \zeta) &= \gamma^1(s_0, \theta, \zeta) \\ \gamma^2(s_0, \theta + 2\pi N_{pol}, \zeta) &= \gamma^2(s_0, \theta, \zeta) \\ \gamma^3(s_0, \theta + 2\pi N_{pol}, \zeta) &= \gamma^3(s_0, \theta, \zeta) \\ &\quad - \frac{2s_0}{q_0} \frac{dq}{ds} \Big|_{s=s_0} 2\pi N_{pol} \gamma^2(s_0, \theta, \zeta) \end{aligned} \quad (S3)$$

where by virtue of the similarity in the interrelations between secular and non-secular components, most of the secular contributions cancel out in these combinations. As within the flux tube the normalised magnetic field strength is given by $B_N(s_0, \theta, \zeta) = \sqrt{\gamma^1(s_0, \theta, \zeta)}$ it follows that the field strength retains the two-fold 2π symmetry of the torus, like it should since it is a physical quantity. Corollary, with regard to magnetic drift-operators [Eqn. (23) from the main text], it follows

that the derivatives of B_N also satisfy this symmetry, and hence from Eqn. (S3) it follows that

$$\begin{aligned}\mathcal{L}_x(s_0, \theta + 2\pi N_{\text{pol}}, \zeta) &= \mathcal{L}_x(s_0, \theta, \zeta) \\ \mathcal{L}_y(s_0, \theta + 2\pi N_{\text{pol}}, \zeta) &= \mathcal{L}_y(s_0, \theta + 2\pi N_{\text{pol}}, \zeta) \\ &\quad - \frac{\gamma^2(s_0, \theta, \zeta)}{\gamma^1(s_0, \theta, \zeta)} \frac{\partial B_N(s_0, \theta, \zeta)}{\partial z} \bigg|_{x,y} \frac{4\pi N_{\text{pol}} s_0}{q_0} \frac{dq}{ds} \bigg|_{s=s_0}\end{aligned}$$

We may write these relations more succinctly in interrelated forms mimicking those of Eqns. (S2) and (S3), by invoking the definition of the drift-operators from Eqn. (23) in the main text as

$$\begin{aligned}\mathcal{L}_x(s_0, \theta + 2\pi N_{\text{pol}}, \zeta) &= \mathcal{L}_x(s_0, \theta, \zeta) \\ \mathcal{L}_y(s_0, \theta + 2\pi N_{\text{pol}}, \zeta) &= \mathcal{L}_y(s_0, \theta, \zeta) + \frac{4\pi N_{\text{pol}} s_0}{q_0} \frac{dq}{ds} \bigg|_{s=s_0} \times \\ &\quad \left(\mathcal{L}_x(s_0, \theta, \zeta) + \frac{\partial B_N(s_0, \theta, \zeta)}{\partial y} \bigg|_{x,z} \right)\end{aligned}\tag{S4}$$

with identical relations also holding for the curvature drift-operators $\mathcal{K}_x = \mathcal{L}_x$ and $\mathcal{K}_y = \mathcal{L}_y + d\beta_{\text{ref}}/dx / (2B_N)$ as the pressure correction term in the latter is strictly non-secular. Lastly, the determinant of the (contravariant) metric tensor may be directly given by $\det[\underline{g}_{\text{FT}}] = g_{\text{FT}}^{zz}\gamma^1 - g_{\text{FT}}^{yz}\gamma^2 - g_{\text{FT}}^{xz}\gamma^3$, such that by combining Eqns. (S2) and (S3) it follows that $\sqrt{g}(s_0, \theta + 2\pi N_{\text{pol}}, \zeta) = \sqrt{g}(s_0, \theta, \zeta)$, where $\sqrt{g} = 1/\det[\underline{g}_{\text{FT}}]$.

The secular mappings from Eqns. (S2) and (S4) apply to a $2\pi N_{\text{pol}}$ poloidal revolution on the flux surface at a fixed toroidal angle ζ , thus corresponding to the same physical location on the torus. The ends of a flux tube are, however, toroidally displaced by $\Delta\zeta = q_0\Delta\theta$ to maintain a fixed field-line label α . Applying Eqns. (S2) and (S4) in general toroidal configuration will result in discrepancies as the metric tensor $g_B^{nm}(s, \theta, \zeta) \neq g_B^{nm}(s, \theta + 2\pi N_{\text{pol}}, \zeta + 2q_0\pi N_{\text{pol}})$, lest the system be axisymmetric or the flux tube is located on a rational surface where $q_0 N_{\text{pol}} \in \mathbb{Z}$. To alleviate this issue we proceed to invoke a *pseudo-axisymmetric* approximation, whereby assuming that $q_0\Delta\theta/L_\zeta \ll 1$, where L_ζ is the smallest characteristic toroidal gradient scale length for the metric tensor $1/L_\zeta = \max \partial \ln g^{nm} / \partial \zeta$, the variation of the geometry along the toroidal direction can be considered negligible with respect to the variation along the poloidal direction. This *pseudo-axisymmetric* approximation implies that $\partial B_N / \partial y|_{x,z} \approx 0$, as under this assumption we have $B_N(s_0, \theta, \zeta) \rightarrow \sqrt{\gamma^1(s_0, \theta)}$, and from Eqn. (21) of the main text it follows that a variation in y (at fixed θ) can only be due to a variation in ζ . Hence, by additionally neglecting $\partial B_N / \partial y|_{x,z}$ Eqns. (S1), (S2) and (S4) agree with Eqn. (26) from the main text, where we additionally used Eqn. (21) from the main text to write $2(s_0/q_0) dq/ds|_{s=s_0} = \hat{s}$, and by induction the formulae were generalised to making $2\pi p N_{\text{pol}}$ poloidal revolutions where $p \in \mathbb{Z}$.

The impact of the *pseudo-axisymmetric* approximation on the reconstructed geometry beyond the original $2\pi N_{\text{pol}}$ extend

of the flux tube is visualised in Figure S1, where we compare the extended geometry in ballooning space $\theta \in [-12\pi, 12\pi]$ for an $N_{\text{pol}} = 1$ and $N_{\text{pol}} = 5$ flux tube generated from an axisymmetric and stellarator equilibrium. For the tokamak case, the extended geometry from the $N_{\text{pol}} = 1$ flux tube generated by Eqn. (26) from the main text perfectly agrees with the $N_{\text{pol}} = 5$ flux-tube geometry (and its extension), which is to be expected due to the exact axisymmetry of the equilibrium. In the stellarator case, however, deviations between the $N_{\text{pol}} = 1$ and $N_{\text{pol}} = 5$ geometry occur beyond the center 2π range, which is due to the violation of the *pseudo-axisymmetric* approximation. The extended geometry generated by Eqn. (26) from the main text then again overlaps at the 2π interval at $\theta = \pm 10\pi$, where the extensions from $N_{\text{pol}} = 1$ and $N_{\text{pol}} = 5$ synchronise (at $p = \pm 5$ and $p = \pm 1$, respectively) since the global shear \hat{s} determining the secular shifts is identical for both flux tubes. Furthermore, the role of the secularity is clearly observable from $\|\mathbf{k}_\perp\|$, the variation of which under the assumption of $k_x = 0$ is determined by $k_y \sqrt{g^{yy}(s_0, \theta, \zeta)}$, and the drift-operator \mathcal{L}_y , whose extreme values increase with every $2\pi N_{\text{pol}}$ iteration due to global shear, with the effect being noticeably stronger in the axisymmetric case due to the higher shear. The violation of the *pseudo-axisymmetric* approximation in stellarator geometry results in discontinuities in e.g. the drift operators and $\|\mathbf{k}_\perp\|$ at every successive $2\pi N_{\text{pol}}$, with the discontinuity proportional to the global shear^{S1}.

S2. RESULT FOR ADDITIONAL GRADIENT-DRIVE SCENARIOS

Here we present additional results obtained with the global dispersion model for both adiabatic (a/L_{Ti} scan without impurities and a/L_{nC} scan with C^{6+} impurity at concentration of $Z_{\text{eff}} = 1.4$) and kinetic-electron scenarios (a/L_n scan for pure density-gradient driven TEM and simultaneous $a/L_{Ti}, a/L_{Te}$ variation with fixed density gradient) in the flux-tube geometries DIII-D tokamak, quasi-symmetric configuration of the HSX stellarator and high-mirror configuration of the W7-X stellarator not discussed in the main text. The relevant information about the range of considered gradients and numerical resolutions used for the GENE simulations are discussed in Section III B and Table II of the main text, respectively.

A. Adiabatic-electron scenarios

Figure S2 shows results in the case of driving-gradient scan of the ion-temperature gradient in absence of impurities. As expected from the ITG instability, growth rates monotonically increase and propagation frequency monotonically shifts in the direction of the ion diamagnetic direction across all length scales with increasing ion temperature gradient. This is most apparent in DIII-D, where for the lowest temperature gradient of $a/L_{Ti} = 3$ modes no instabilities are observed in GENE simulations beyond a wavenumber of $k_y \rho_{ss} \geq 1.6$, whereas an increase in temperature gradient of $a/L_{Ti} = 4$

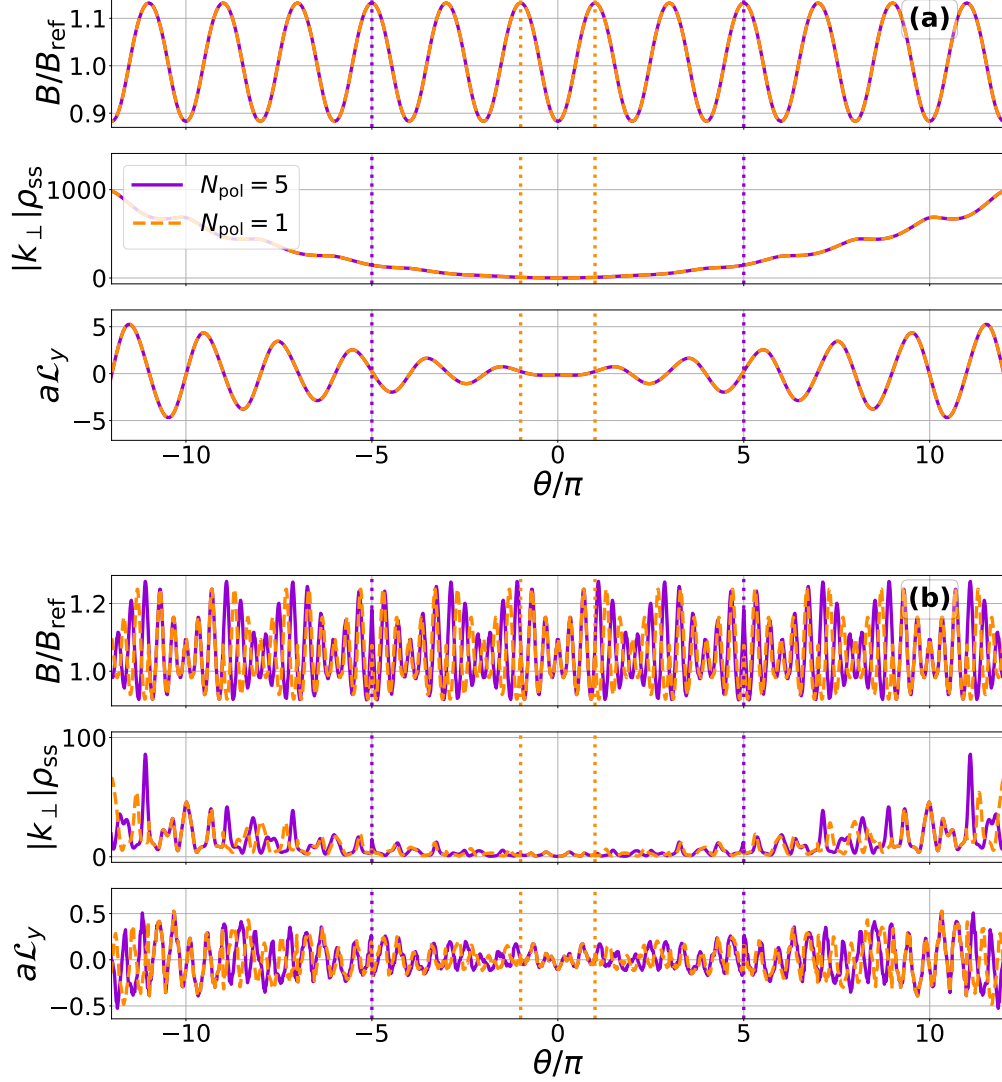


FIG. S1: Extended flux tube geometries into ballooning-space reconstructed from $N_{\text{pol}} = 1$ (dashed orange) and $N_{\text{pol}} = 5$ (solid purple) geometric data using Eqn. (26) from the main text under the *pseudo-axisymmetric* approximation for (a) a tokamak equilibrium and (b) the high-mirror configuration of W7-X. For both configurations, an $\alpha = 0$ flux tube is considered at the $s_0 = 0.5$ flux surface, where the global magnetic shear is given by $\hat{s} \approx 0.8$ and $\hat{s} \approx -0.11$ for (a) and (b), respectively. Vertical dotted lines indicate the extent of the original “raw” geometric data. Here we focus on most important geometric features for the ITG-TEM dispersion relation, being the arrangement of trapping regions through B , the magnetic drift wells through the bi-normal component of the ∇B drift-operator \mathcal{L}_y , and the FLR damping through $\|\mathbf{k}_\perp\|$, where we taken a wavenumber of $k_x \rho_{\text{ref}} = 0$, $k_y \rho_s = 1$ for visualisation purposes.

subsequently destabilises these high wavenumber modes, as also reproduced by the global dispersion model. In both stellarator configurations, unstable modes occur at all length scales, even at the smallest gradient of $a/L_{Ti} = 3$, with several mode transitions occurring at lower wavenumber range, until the eigenmodes become strongly ballooned around $\theta = 0$ for intermediate-high wavenumbers, with the transition point shifting to smaller k_y as temperature gradient is increased. Regardless of the eigenmode, propagation frequencies shift further into the ion diamagnetic direction and growth rates in-

crease as a/L_{Ti} is increased, like in DIII-D, which is reproduced by the dispersion model. The dispersion model performs quantitatively better in HSX, with a smaller growth rate overprediction and tighter match of propagation frequencies. At the transition wavenumber, the global dispersion model consistently estimates a propagation frequency in the electron diamagnetic direction, while GENE simulations only result in modes traversing in the ion diamagnetic direction. In HSX a few modes are also found to propagate in the electron diamagnetic direction at the transition wavenumber, though there this

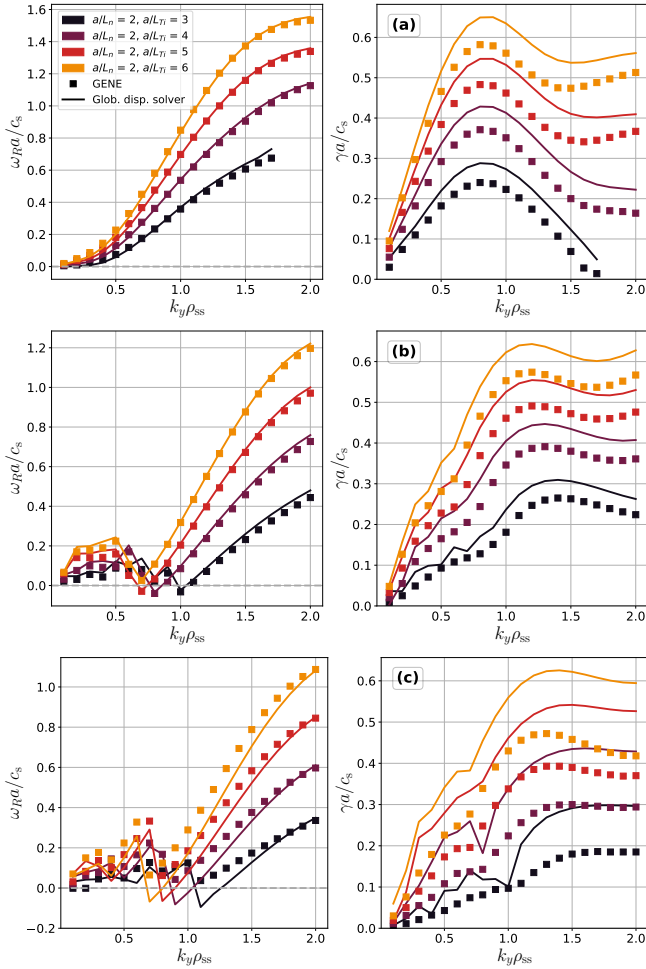


FIG. S2: Eigenfrequency solutions obtained by the global dispersion model (solid lines) contrasted with GENE simulations (symbols) for adiabatic-electron ITG while varying the ion-temperature gradient a/L_{Ti} (lighter colours indicate a stronger temperature gradient). Shown are results for (a) the DIII-D tokamak, (b) the HSX stellarator and (c) the high-mirror configuration of the W7-X stellarator. In all cases the density gradient is fixed at $a/L_n = 2$ and no C^{6+} impurities are considered.

matches the behaviour observed from GENE simulations. The model, however, does correctly reproduce the stronger dispersion of growth rates at high wavenumber in HSX, compared to virtually constant growth rates (with exception of $a/L_{Ti} = 6$) in W7-X.

When impurities are considered, a second dilution effect beyond the reduction of the (main) ion concentration, as considered in the main text, may occur due to the shape of the impurity density profile^{S2}. To maintain ambipolarity, the profile of the (main) ion density has to adjust itself such that the net positive charge gradient equals the electron density gradient (see Eqn. (25) in the main text). Unlike the density-dilution effect, this gradient dilution may result in either reduction/enhancement of ITG drive by the main ion species if

the impurity profile is more/less steep than the electron density gradient. The results of a scan in a/L_{nC} probing the two-sided effect of this drive dilution are shown in Figure S3, where we consider both peaked impurity density profiles – over a range where the impurity density gradient both exceeds and is eclipsed by a/L_{ne} – and hollow profiles (indicated by $a/L_{nC} < 0$), at a fixed impurity concentration. Unlike in Figure S2 where the ion-temperature gradient is modified, the shift of propagation frequency towards ion diamagnetic direction as a/L_{nC} is diminished (corresponding to an increase in a/L_{ni}) is less pronounced than the destabilisation of the growth rates. This may be attributed to the fact that the changes in the ion density gradient are comparatively moderate (ranging from $a/L_{ni} \in [1.652, 2.522]$), such that the overall diamagnetic frequency is not significantly impacted. In general both the growth rate and propagation frequency exhibit similar trends in model performance when a/L_{nC} is varied as when a/L_{Ti} was varied in absence of impurities, thus showing that the global dispersion model correctly captures the physics associated with the density dilution effect on adiabatic-electron ITG modes.

B. Kinetic-electron scenarios

In Figure S4 we present results for the density-gradient drive scan including kinetic-electron effects, where neither ITG nor ∇T_e -TEM can occur, and thus predominantly density-gradient-driven TEMs are expected. Indeed, in DIII-D only TEMs are found below $k_y \rho_s \approx 1.0$, while for larger wavenumbers the ubiquitous mode (UM) occurs, with the transition point where the frequency crosses into the ion diamagnetic direction slightly shifting towards lower wavenumber as the density gradient is increased. Growth rates increase monotonically with wavenumber, though the largest increase is obtained between $a/L_n = 1$ and $a/L_n = 2$, as also reproduced by the model. The global dispersion relation model, however, makes a larger error at high k_y where the UMs occur compared to low wavenumber where TEMs occur. In HSX, nearly all eigenmodes are found in the electron diamagnetic direction, indicating they correspond to different branches of TEMs. As the density gradient is increased, a new cluster of modes appear around $0.2 \leq k_y \rho_s \leq 0.6$ in a separate frequency band, which are distinctly stronger destabilised as a/L_n is increased compared to the TEMs. These instabilities are characterised by significantly more extended eigenmodes without strong preferential localisation to any of the magnetic or drift wells and correspond to cases of the universal instability (UI)^{S3,S4}. Similar modes also occur in the high-mirror configuration of W7-X, though only for the higher density gradients of $a/L_n = 3, 4$ in the smaller wavenumber region of $0.2 \leq k_y \rho_s \leq 0.4$, with the remainder of the instabilities corresponding to ion-driven trapped electron modes (iTEMs)^{S5}. Both of these observations regarding the UI may be explained in terms of the shear-dependent threshold density gradient which is necessary for this instability to thrive^{S3}, with the shear in W7-X being larger by an order of magnitude, however, simultaneously the instability

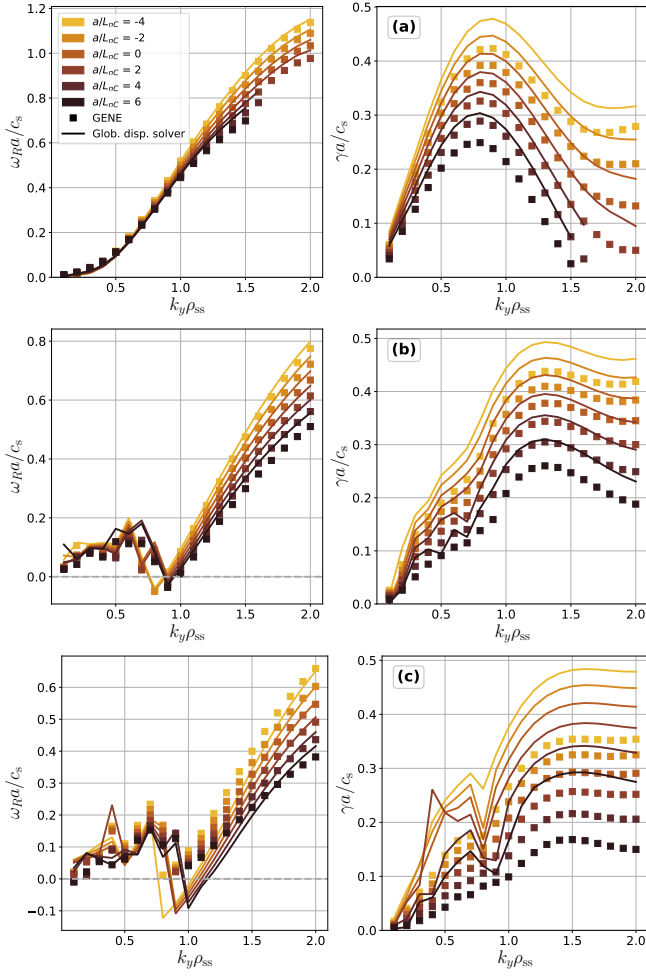


FIG. S3: Eigenfrequency solutions obtained by the global dispersion model (solid lines) contrasted with GENE simulations (symbols) for adiabatic-electron ITG while varying the impurity density gradient a/L_{nC} (darker colours indicate a stronger density gradient). Shown are results for (a) the DIII-D tokamak, (b) the HSX stellarator and (c) the high-mirror configuration of the W7-X stellarator. In all cases the electron density gradient is fixed at $a/L_{ne} = 2$ while the ion density gradient a/L_{ni} is modified to respect ambipolarity, the temperature gradient is fixed at $a/L_{Ts} = 4$ for both deuterium ions and carbon impurity, while the C^{6+} impurity content is fixed to maintain a value of $Z_{\text{eff}} = 1.4$.

drive for (i)TEMs being smaller by an order of the trapped-electron fraction because of the lack of unfavourable bounce-average curvature due to the maximum- J property of the configuration. Aside from the UIs – for which the dispersion relation model fails to predict accurate growth rate attributable to lack of kinetic response for passing electrons – the global dispersion relation does reproduce the fact that growth rates are significantly smaller in W7-X compared to either DIII-D or HSX for a given wavenumber and density gradient, indicating the weaker drive of iTEMs compared to conventional TEMs. However, the frequency of these iTEMs is not as accu-

ately predicted by the model compared to frequency of conventional TEMs, with low wavenumber modes being assigned a frequency in the electron diamagnetic direction, opposed iTEMs being characterised by propagation frequencies in the ion diamagnetic direction. Comparing the output of the model to eigenfrequencies obtained by GENE simulations, there is an overall downshift of propagation frequencies into the electron diamagnetic direction and an overprediction of growth rates, which are significantly larger compared to the errors made for TEMs in DIII-D and HSX. This may be attributed to the diminished influence of trapped electrons, which are strictly necessary to make the model variational, and the increased importance of passing electrons, which are only accounted for adiabatically. This hypothesis is further confirmed in Section S3 where the negative mirror configuration is examined, which is distinctively not maximum- J . Most notably, with the exception of the UI modes, the accuracy of the model to reproduce GENE eigenfrequencies decreases with increasing a/L_n universally across all three geometries.

Lastly in Figure S5, we consider the scenario of realistic profiles where finite ion- and electron-temperature gradient coexist, where both situations with a dominant effect of ion temperature gradient ($a/L_{Ti} > a/L_{Te}$, indicated by reddish hues) and dominant electron temperature gradient ($a/L_{Te} > a/L_{Ti}$, indicated by blueish hues) are considered around a nominal scenario with balanced gradients ($a/L_{Ti} = a/L_{Te} = a/L_n$, indicated in purple). For each of the two dominant scenarios, we consider a case with low temperature gradient ($a/L_{Ts} = a/L_n$, indicated by lighter colour) and high temperature gradient ($a/L_{Ts} > a/L_n$, indicated by darker colour) to also probe for $\eta_s = L_{Ts}/L_n$ effects, where $s = i, e$. Across the three geometries, both the model and GENE simulations indicate that the ion temperature gradient plays a more determining role on the type of instabilities that occur, with the most significant changes in propagation frequency occurring when a/L_{Ti} is changed from its nominal value of 3 to 5 or 1. When the ion temperature gradient is kept fixed, both the model and the GENE simulations predict an increase in the growth rate as a/L_{Te} increases, particularly at high wavenumbers. In particular, the inclusion of finite temperature gradient for both species is sufficient for UI modes to no longer appear in the high-mirror configuration of W7-X (though they may persist as subdominant unstable mode), resulting in improved agreement between the model and GENE simulations at low wavenumber. For the $a/L_{Ti} = 5, a/L_{Te} = 3$ case, growth rates in W7-X are however significantly overestimated by the model for $k_y \rho_{ss} > 1$ compared to other gradients. Like with high ion temperature gradient case discussed in the main text, this corresponds to a scenario of iTEM transitioning into a higher-excitation state of ITG, for which, as explained in the main text, any error made in the growth rate as a result from the lack of Landau damping from ion parallel streaming is subsequently enhanced. Similar observations can also be made about the ion-temperature-gradient dominated cases in DIII-D, where the high- k_y large- a/L_{Ti} mode growth rates (maroon curve) obtained by the model continue to grow without bound, while the GENE simulations clearly show that those modes are stabilised as k_y increases as a result

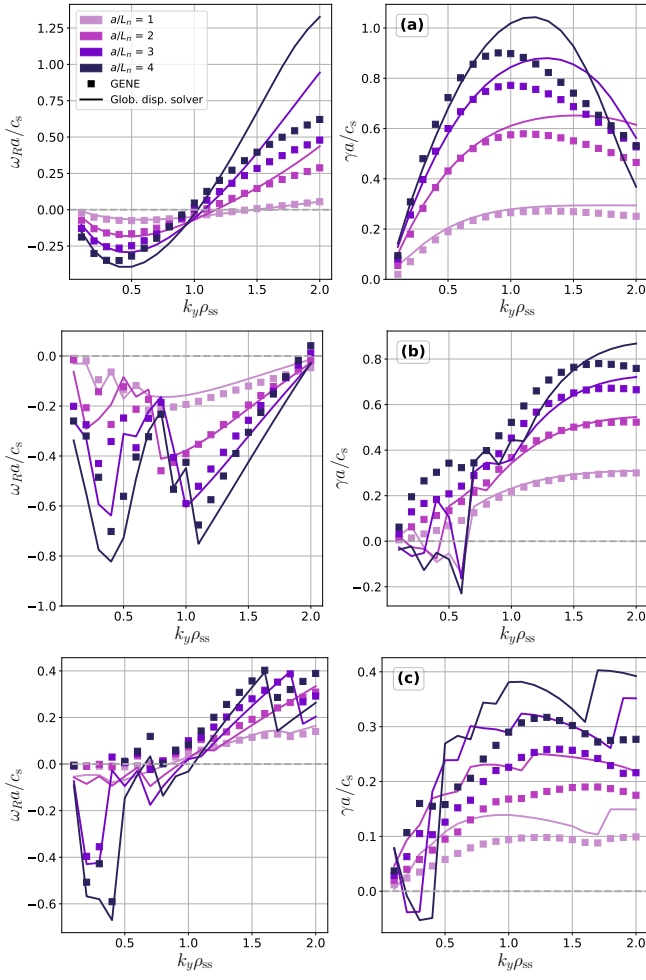


FIG. S4: Eigenfrequency solutions obtained by the global dispersion model (solid lines) contrasted with GENE simulations (symbols) including kinetic-electrons while varying the density gradient a/L_n (darker colours indicate a stronger density gradient). Shown are results for (a) the DIII-D tokamak, (b) the HSX stellarator and (c) the high-mirror configuration of the W7-X stellarator. In all cases both temperature gradients are suppressed ($a/L_{Ti} = a/L_{Te} = 0$).

of FLR damping. This behaviour of the model is robust to changes in numerical resolution used to calculate the resonant ion integrals as well as change of root finding algorithm from the Broyden method^{S6} to a conventional Newton method, and is deemed a numerical artifact as a result of geometric details of the DIII-D flux-tube – presumably the high global shear – rather than a physical aspect predicted by the model in axisymmetric configurations. Indeed, as will be shown in Section S3, the dispersion relation model accurately predicts both growth rates and propagation frequencies for identical gradients in the TCV tokamak – where the shear is reduced by more than a factor of two compared to DIII-D – which closely follow the trends observed in the GENE simulations. Unlike the pure a/L_{Ti} case, however, these high- k_y high- a/L_{Ti}

modes do not correspond to a higher excitation-state ITG, but are some form of hybrid UM-ITG as there are no mode transitions observed in the propagation frequency. It should also be remarked that only in the $a/L_{Ti} = 3, a/L_{Te} = 1$ case we observe the issue for intermediate-to-high- k_y UMs identified in the main text – being that the model predicts simultaneously large propagation frequency and small growth rates – while this issue is resolved in the $a/L_{Ti} = 3, a/L_{Te} = 3$ case. This indicates that as the electron temperature gradient is increased the trapped-electron contribution to the dispersion relation gains more prominence, which, containing the regularisation physics through the bounce-average of the electrostatic potential, aids to alleviate the issue arising from the ion contribution. The model's sensitivity to high global shear would also explain why the global dispersion relation model does not suffer from similar divergences (aside from the aforementioned higher excitation state ITG mode in W7-X) in both stellarator configurations, where the shear is substantially lower.

S3. INVESTIGATION OF CONFIGURATION EFFECTS

The results from Section IV of the main text and Section S2 show that the global dispersion relation model can accurately account for inherent geometric differences between different classes of toroidal magnetic confinement devices. Consequently, the differences in geometric features between these devices are significant. To test whether the model is equally sensible to more subtle changes in the local geometric flux-tube quantities, we performed additional tests between two configurations of the same device. For this, both a positive and negative-triangularity equilibrium of the TCV tokamak and the negative-mirror configuration of the W7-X stellarator (to be compared with the high-mirror configuration discussed in the main text) are chosen. The differences in the most important flux-tube geometric quantities between these configurations are shown in Figure S6. The main differences between the TCV configurations are found in the FLR term, which increases faster in the $\delta > 0$ configuration, where δ denotes the triangularity, and the magnetic-drift well, which is both steeper and more stretched out in the $\delta < 0$ configuration. Meanwhile, the magnetic field strength is nearly identical between the configurations, aside from a slightly shallower and flatter magnetic well observed in the $\delta < 0$ configuration, corresponding to the straight section of the D-shaped flux-surface coinciding with the low-field side. By contrast, both the magnetic-drift wells and FLR term are nearly identical between the two W7-X configurations, while the magnetic field strengths differ significantly. As a consequence, the magnetic wells and regions of bad curvature are again aligned in the negative-mirror configuration, rendering the negative-mirror flux tube unstable to conventional TEMs.

Comparing positive and negative triangularity TCV

In Figure S7 results for adiabatic-electron scenarios are presented for both TCV configurations. In general the model

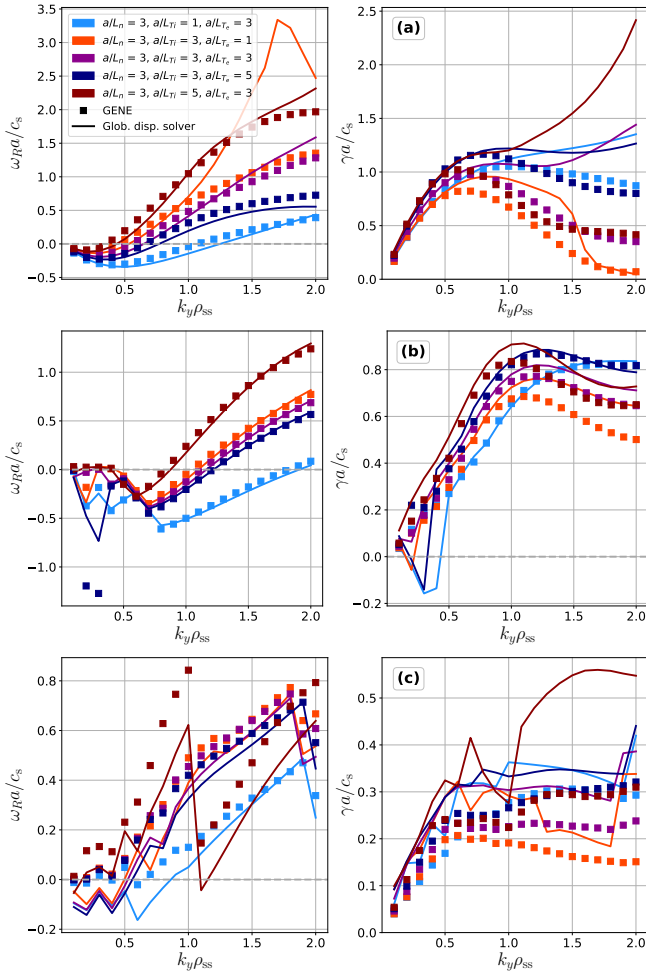


FIG. S5: Eigenfrequency solutions obtained by the global dispersion model (solid lines) contrasted with GENE simulations (symbols) including kinetic-electrons for realistic non-flat kinetic profiles of both species. Both the ion- and electron-temperature gradient are varied simultaneously, with blue and red hues indicating cases of dominant electron-temperature gradient ($\eta_e > \eta_i$) and dominant ion-temperature gradient ($\eta_i > \eta_e$), respectively, with darker hues indicating a stronger (dominant) temperature gradient. Shown are results for (a) the DIII-D tokamak, (b) the HSX stellarator and (c) the high-mirror configuration of the W7-X stellarator. In all cases the density gradient is fixed at $a/L_n = 3$.

captures the trend that peak growth rates are both smaller and shifted to lower wavenumber in the negative triangularity flux-tube compared to its positive-triangularity counterpart. At very low wavenumbers $k_y \rho_{ss} \leq 0.3$, ITG modes are, however, marginally more unstable in the negative-triangularity configuration as a result of the aforementioned shift in growth rate peak – as observed in both GENE simulations and solutions to the global dispersion model. The model does qualitatively capture that (in absence of impurities) there is a weaker dispersion in growth rates in the negative triangularity case,

with growth rates being nearly constant as a function of k_y at higher wavenumber in both the GENE simulations and solutions to the dispersion model. Whereas the overprediction of growth rates by the model is virtually constant in the positive triangularity case, the negative triangularity case displays near-accurate growth rates for low-wavenumber while a significantly larger error is made for high-wavenumber modes, which contributes to the disparity observed between the GENE simulations and the global dispersion model with regards to the preferential role of negative triangularity for ITG stability. Setting aside this discrepancy in the large-wavenumber regime, the results here are in agreement with earlier investigations on the effects of triangularity in on adiabatic-electron ITG^{S7–S9}, though it should be emphasized that the beneficial role of negative triangularity is not a general property and depends on other details of the magnetic configuration under investigation, most notably the (global) magnetic shear^{S7}. These observed trends about the model's performance mostly extrapolate to the cases where impurity effects are included, where both dilution effects observed in the Gene simulations are qualitatively reproduced by the model. Noticeable exceptions, however, occur for a handful of high-wavenumber modes when the dilution effects are strongest (particularly $k_y \rho_{ss} = 1.5, 1.6, 1.8$ for $Z_{\text{eff}} = 2.0$, $k_y \rho_{ss} = 1.4, 1.5$ for $a/L_{nC} = 4$ and $k_y \rho_{ss} = 1.3-2$ for $a/L_{nC} = 6$) where both frequency and growth rate are significantly overpredicted by the model, though this only occurs for the positive triangularity configuration. The eigenmodes corresponding to those cases show a significantly broader structure with weaker localisation to the out-board mid-plane, and are contrast to conventional ITG modes observed at other wavenumbers. As these discrepancies only occur for the aforementioned modes, it may be possible that this disparity between the model and high-fidelity simulations is a result of the neglect of the effect of particle streaming.

To investigate the model's sensitivity to configuration effects from triangularity we split the kinetic-electron scenarios in two cases: those with and without a finite ion temperature gradient to focus on pure TEM scenarios and mixed ITG-TEM scenarios, with results shown in Figures S8 and S9, respectively. Akin to the adiabatic-electron ITG case, both the global dispersion model and GENE simulations show lower peak growth rates with the peak shifted to smaller wavenumbers in the negative-triangularity configuration for density-gradient-driven TEM, with the model closely following GENE results. Again, the shift of growth-rate peak to smaller k_y results in a marginal destabilisation of low k_y modes when going from $\delta > 0$ to $\delta < 0$ (most notably in the region $k_y \rho_{ss} \leq 0.3$, though the effect persists up to $k_y \rho_{ss} = 0.5$ at the largest gradient), though simultaneously the growth rates are erroneously predicted to be constant at high k_y in the negative-triangularity configuration by the model. However, this situation changes when the effects of a finite electron-temperature gradient are considered. For $\eta_e \leq 1$, where $\eta_e = L_n/L_{Te}$, aside from a shift in propagation frequency into the electron diamagnetic direction, the stability properties of positive and negative triangularity configurations are unchanged. By contrast, when $\eta_e > 1$, a peak in growth rate spectrum eludes both GENE simulations and results from the global dispersion model, with both indi-

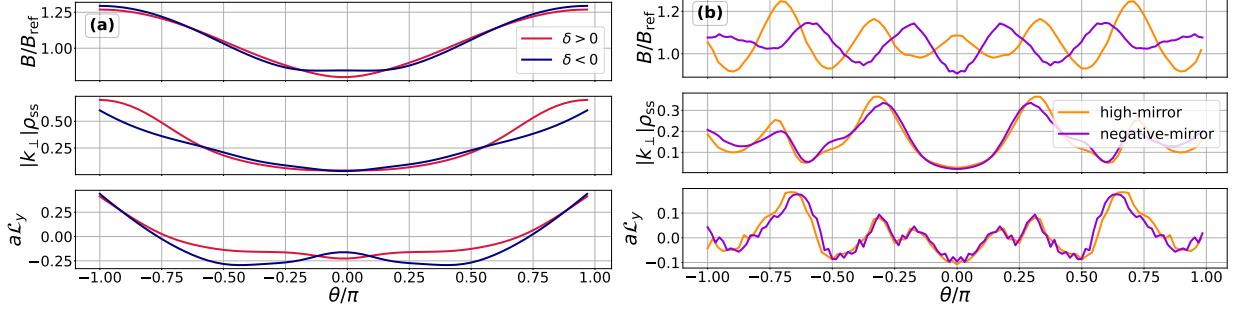


FIG. S6: Comparison of flux-tube geometric quantities between (a) positive- (red) and negative-triangularity (blue) configurations of the TCV tokamak and (b) high- (orange) and negative-mirror (purple) configurations of the W7-X stellarator. Shown are the variation of the magnetic field strength (top panel), magnitude of the perpendicular wavenumber (middle panel) and bi-normal component of the ∇B drift (bottom panel). For $\|\mathbf{k}_\perp\|$ we have consider a wavenumbers of $k_x \rho_{ss} = 0$ and $k_y \rho_{ss} = 0.3$, to facilitate comparisons with Figures 1 and 2 from the main text.

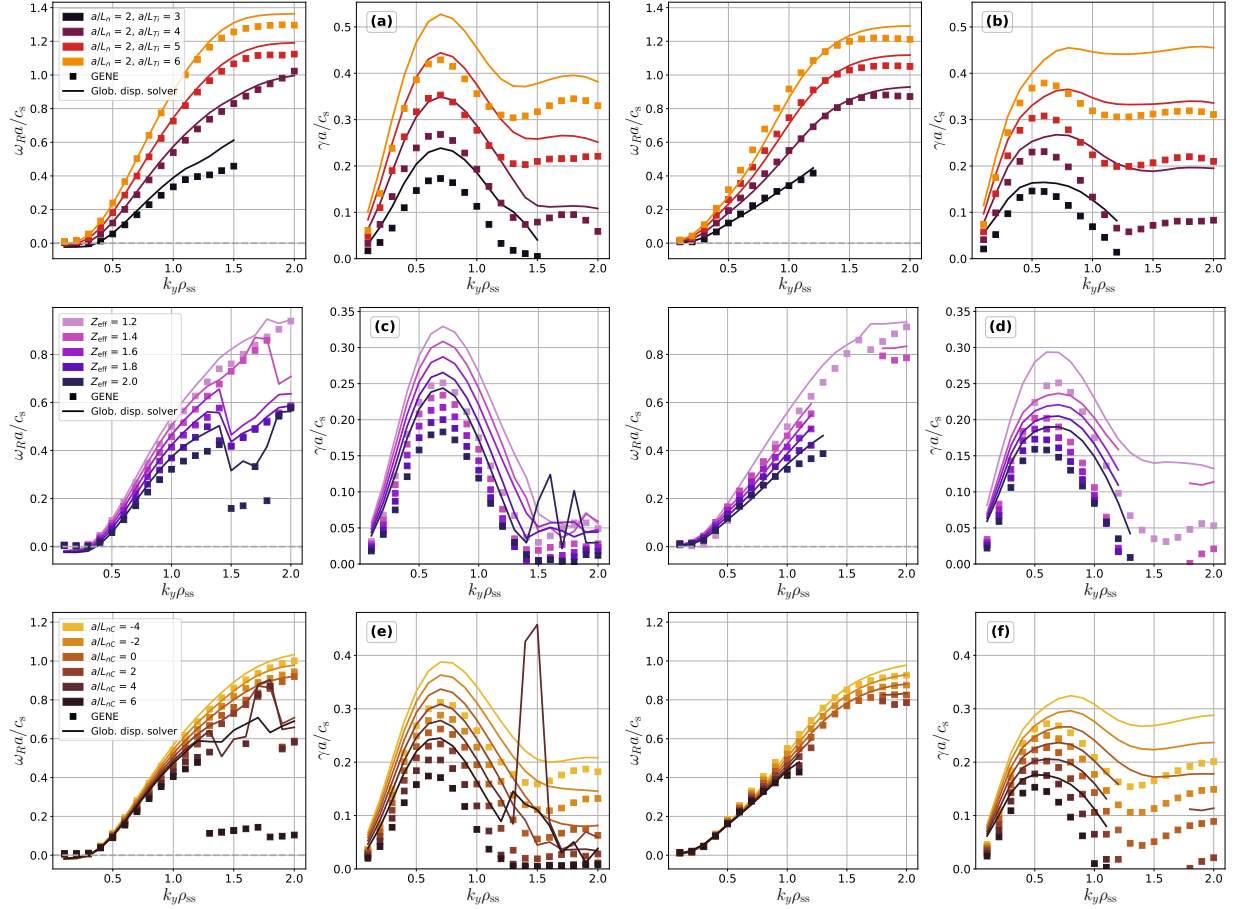


FIG. S7: Eigenfrequency solutions obtain by the global dispersion model (solid lines) contrasted with GENE simulations (symbols) for adiabatic-electron scenarios in positive triangularity TCV flux tube (left column) and negative triangularity flux tube (right column) of the TCV tokamak. Shown are results while varying (a)-(b) ion-temperature gradient a/L_{Ti} [no C^{6+} impurities], (c)-(d) impurity concentration Z_{eff} [with ambipolar gradients $a/L_{ni} = a/L_{nC} = 2$], and (e)-(f) impurity density gradient a/L_{nC} [at fixed $Z_{\text{eff}} = 1.4$]. In all cases the electron density gradient is fixed at $a/L_{ne} = 2$, with ion and impurity density (gradient) determined by ambipolarity constraints [Eqn. (25) in main text]. Note that the axis limits for both ω_R and γ are matched between left and right columns to facilitate quantitative comparison.

cating that high k_y modes are progressively more destabilised in the negative triangularity configuration compared to its positive triangularity counterpart as a/L_{Te} is increased. This effect can be attributed to the behaviour of the propagation frequency, where the shift into the electron diamagnetic direction of the propagation frequency is more pronounced in the negative triangularity configuration, making resonant excitation of temperature-gradient-driven TEMs ($\omega_R < 0$) with the electron precession drift over non-resonant excitation from UMs ($\omega_R > 0$) possible. Additionally, as the drift-well in the negative triangularity is both deeper and wider, all but the most shallowly trapped-electrons will have more destabilising bounce-averaged magnetic drift compared to the positive triangularity configuration^{S10}. Unlike for the adiabatic-electron ITG scenario, there is no clear consensus on whether negative triangularity should have beneficial effects over positive triangularity for TEM – though it would be expected based on the strong reduction in electron heat diffusivity observed in both experiments^{S11} and non linear simulations^{S10,S12} in TCV – with previous studies reporting both a stabilising and destabilising effect depending on wavenumber, gradients and geometric details of the chosen flux tube^{S7,S10,S12,S13}.

When the effect of a finite ion temperature gradient is included [see Figure S9] the instability classification becomes more complex as modes propagating in the ion diamagnetic direction may be either UM or ITGs, and unlike the DIII-D case discussed in Figure 5 of the main text and Figure S5 there is an absence of clear mode transitions. Rather, in both TCV configurations we observe that as the ion temperature gradient is increased (in absence of electron temperature gradient) there is a gradual change in the dispersive behaviour, with propagation frequencies and growth rates no longer approximately linearly increasing and decreasing, respectively, at high k_y , but instead flattening off and attaining a second smaller instability peak, respectively, as the ion temperature gradient is increased. This would suggest the possibility of hybrid UM-ITG modes. Regardless of the nature of these modes, we observe that the global dispersion model closely follows the trends observed in the GENE simulations, which like the adiabatic-electron ITG case and pure TEM case show that the negative triangularity configuration has increased resilience to instability at intermediate-high k_y , though is marginally more unstable at low k_y compared to its positive triangularity counterpart. In particular the increased stabilisation is more pronounced compared to the pure TEM cases from Figure S8. When in addition to the a/L_{Ti} also the electron temperature gradient is reintroduced, a combination of the aforementioned effect occurs, though the difference between positive and negative triangularity is most pronounced for cases where the ion temperature gradient dominates ($a/L_{Ti} \geq a/L_{Te}$, corresponding to red and purple curves). For cases with a dominant electron temperature gradient $a/L_{Te} > a/L_{Ti}$ high (low) wavenumber modes are only marginally (de)stabilised by negative triangularity in GENE simulations, though as a result of larger growth-rate estimation in $\delta < 0$ configuration, the opposite effect is predicted by the global dispersion model at the highest wavenumbers.

Results for W7-X negative-mirror configuration

Results for adiabatic-electron and kinetic-electron scenarios in the flux-tube geometry of the negative-mirror configuration of W7-X are shown in Figures S10 and S11, respectively. Comparing Figure S10 to Figures S2 and S3 and Figure 3 of the main text we notice that there are only marginal differences in the dispersion of adiabatic-electron ITG between the negative-mirror and high-mirror configurations of W7-X in both the GENE simulations and the global dispersion model. This can be explained from the near-identicalness of both the magnetic-drift wells and perpendicular wavenumber $\|\mathbf{k}_\perp\|$ between these configurations [see Figure S6], such that instability drive by regions of unfavourable magnetic curvature and FLR damping effects on the ITG mode are approximately equal, unlike for the TCV case.

Significant differences (more pronounced than those observed between the positive- and negative-triangularity configurations of TCV in Figures S8 and S9) with the high-mirror configuration are, however, observed for kinetic-electron cases when comparing Figure S11 with Figure S4 and Figures 4 and 5 of the main text. Due to (re)alignment of magnetic wells and regions of bad-curvature conventional TEMs prevail in the negative mirror configuration in situations without an ion temperature gradient ($a/L_{Ti} = 0$), where in the high-mirror configuration predominantly iTEMs occurred. Most notably in the aforementioned scenarios the growth rates are approximately twice as large in the negative-mirror configuration compared to the high-mirror configuration – a feature which is also closely reproduced by the global dispersion model – which can be attributed to the additional instability drive from trapped-electrons residing in regions of bad-bounce-averaged magnetic curvature in the former configuration. Despite being unstable against conventional TEMs, a handful of UI modes still appear in the negative-mirror configuration for $k_y \rho_{ss} = 0.2-0.4$ at large density gradient $a/L_n = 4$, being in a similar wavenumber range where UIs are observed in the high-mirror configuration. Qualitatively different behaviour between both configurations is also observed when a finite ion temperature gradient is considered. For $k_y \rho_{ss} \geq 0.6$ the eigenfrequency monotonously transitions from electron-diamagnetic direction to ion-diamagnetic direction as the ion temperature gradient is increased, with a simultaneous increase of peak growth rate and shift of growth-rate-maximum to lower k_y , analogous to what was previously observed in HSX [see Figure 5 of the main text], and thus by similar conventions being identified as iTEM. Unlike the high-mirror configuration, however, a transition to a second branch of higher excitation states of ITG at higher ion-temperature gradients is absent, which may also be attributed to the additional drive of trapped-electrons to iTEMs, as in the wavenumber range of $k_y \rho_{ss} \geq 0.6$ growth rates for the negative mirror configuration exceed those found in the high-mirror configuration [see Figure 5]. In the low-wavenumber region of $k_y \rho_s \leq 0.5$ we observe a transition from conventional TEMs to ITG for $a/L_{Ti} = 5, 6$, much akin to the iTEM-ITG transition observed in the high-mirror configuration, though unlike the latter, there is a threshold temperature gradient for this transition to occur.

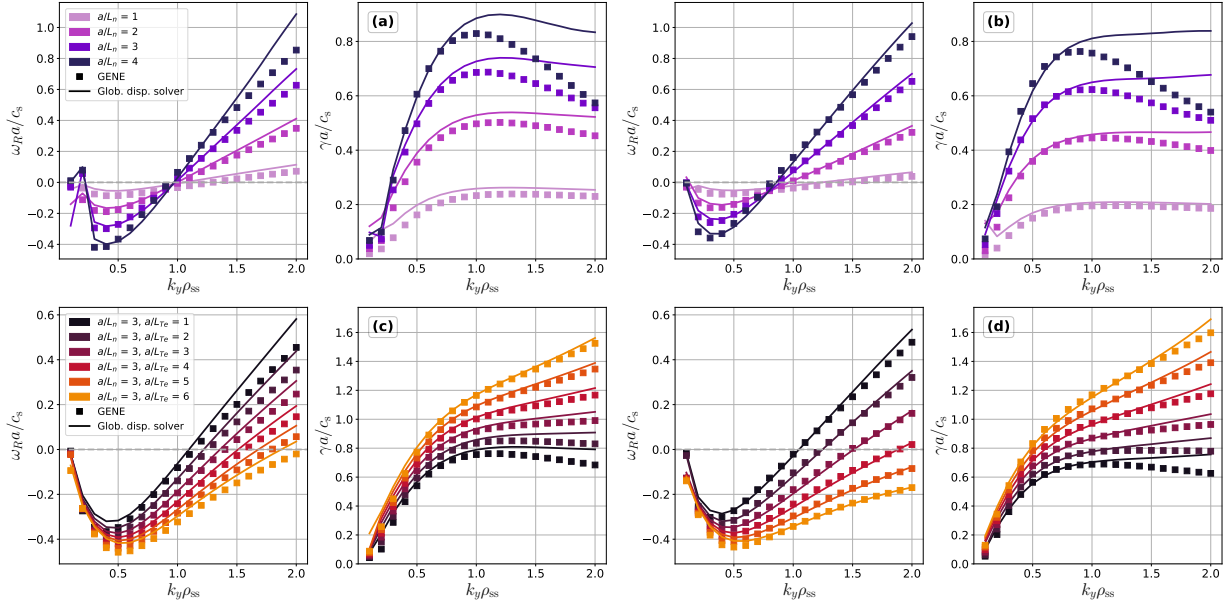


FIG. S8: Eigenfrequency solutions obtain by the global dispersion model (solid lines) contrasted with GENE simulations (symbols) for kinetic-electron scenarios in response to TEM driving gradients in positive triangularity TCV flux tube (left column) and negative triangularity flux tube (right column) of the TCV tokamak. Shown are results while varying (a)-(b) the density gradient a/L_n with suppressed electron temperature gradient ($a/L_{Te} = 0$), (c)-(d) the electron temperature gradient a/L_{Te} at a fixed density gradient of $a/L_n = 3$. In all cases the ion temperature gradient is suppressed ($a/L_{Ti} = 0$) to prevent the emergence of ITG modes. Note that the axis limits for both ω_R and γ are matched between left and right columns to facilitate quantitative comparison.

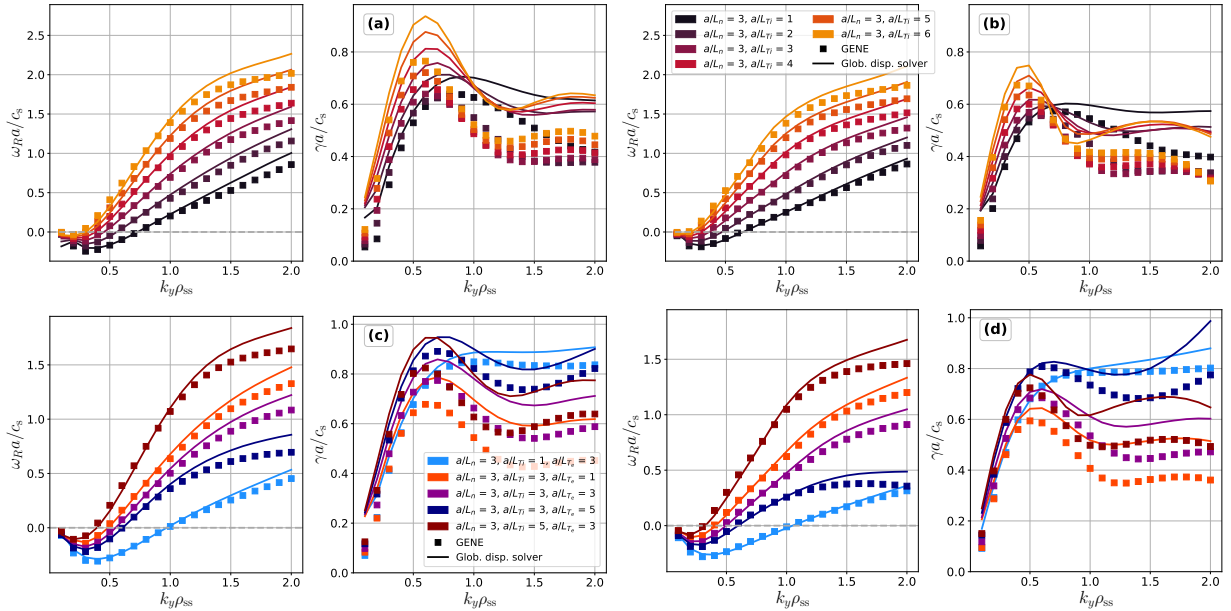


FIG. S9: Eigenfrequency solutions obtain by the global dispersion model (solid lines) contrasted with GENE simulations (symbols) for gradients supporting mixed ITG-TEM modes in positive triangularity TCV flux tube (left column) and negative triangularity flux tube (right column) of the TCV tokamak. Shown are results while varying (a)-(b) the ion temperature gradient a/L_{Ti} with suppressed electron temperature gradient ($a/L_{Te} = 0$), (c)-(d) both a/L_{Ti} , a/L_{Te} to create realistic non-flat kinetic profiles. In all cases the density gradient is fixed at $a/L_n = 3$. Note that the axis limits for both ω_R and γ are matched between left and right columns to facilitate quantitative comparison.

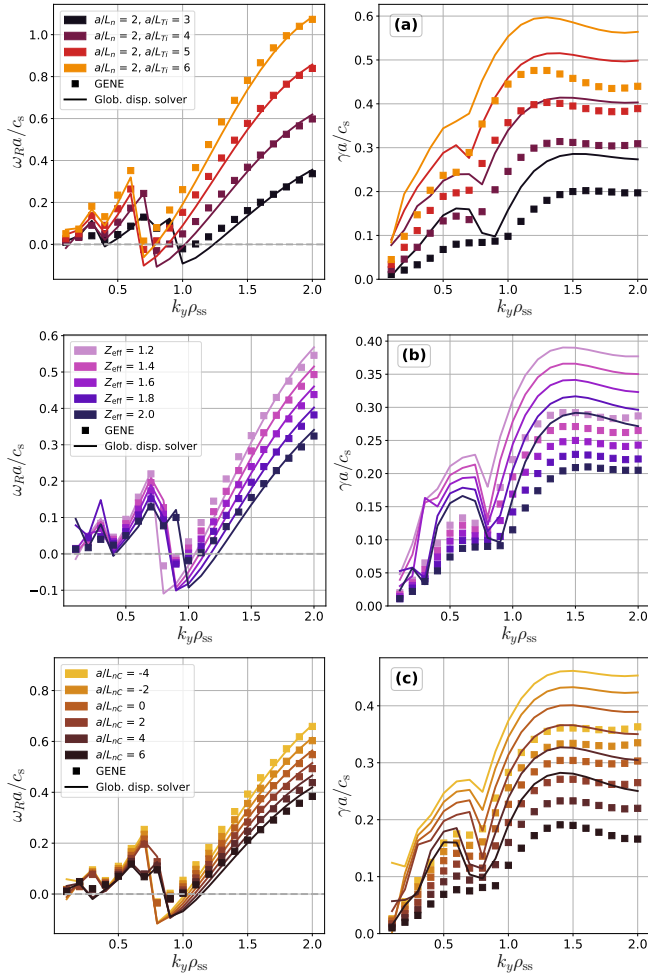


FIG. S10: Eigenfrequency solutions obtain by the global dispersion model (solid lines) contrasted with GENE simulations (symbols) for adiabatic-electron scenarios in the negative mirror configuration of W7-X. Shown are results while varying (a) ion-temperature gradient a/L_{Ti} [no C^{6+} impurities], (b) impurity concentration Z_{eff} [with ambipolar gradients $a/L_{ni} = a/L_{nC} = 2$], and (c) impurity density gradient a/L_{nC} [at fixed $Z_{eff} = 1.4$]. In all cases the electron density gradient is fixed at $a/L_{ne} = 2$, with ion and impurity density (gradient) determined by ambipolarity constraints [Eqn. (25) in main text].

Analogous observations also hold for the case with realistic

gradients when both ion- and electron temperature gradients are present. In general, the quantitative agreement between the global dispersion model and GENE simulations is significantly better in the negative-mirror configuration compared to the high-mirror configuration, which can be directly attributed to the diminished influence of trapped-electrons to the instability drive in the latter as a result of the configuration (approximately) satisfying the maximum- J criterion.

- [S1]Mike F. Martin, Matt Landreman, Pavlos Xanthopoulos, Noah R. Mandell, and William Dorland. The Parallel Boundary Condition for Turbulence Simulations in Low Magnetic Shear Devices. *Plasma Physics and Controlled Fusion*, 60(9):095008, 3 2018.
- [S2]Clemente Angioni. Impurity transport in tokamak plasmas, theory, modelling and comparison with experiments. *Plasma Physics and Controlled Fusion*, 63(7):073001, 7 2021.
- [S3]Matt Landreman, Thomas M. Antonsen, and William Dorland. Universal instability for wavelengths below the ion Larmor scale. *Physical Review Letters*, 114(9):095003, 3 2015.
- [S4]P. Helander and G.G. Plunk. The universal instability in general geometry. *Physics of Plasmas*, 22(9):090706, 9 2015.
- [S5]G. G. Plunk, P. Helander, P. Xanthopoulos, and J. W. Connor. Collisionless microinstabilities in stellarators. III. The ion-temperature-gradient mode. *Physics of Plasmas*, 21(3):032112, 3 2014.
- [S6]C. G. Broyden. A class of methods for solving nonlinear simultaneous equations. *Mathematics of Computation*, 19(92):577–593, 1965.
- [S7]Gabriele Merlo and Frank Jenko. Interplay between magnetic shear and triangularity in ion temperature gradient and trapped electron mode dominated plasmas. *Journal of Plasma Physics*, 89(1):905890104, 2 2023.
- [S8]Gabriele Merlo, Mattia Dicorato, Bryce Allen, Tilman Dannert, Kai Geraschewski, and Frank Jenko. On the effect of negative triangularity on ion temperature gradient turbulence in tokamaks. *Physics of Plasmas*, 30(10), 10 2023.
- [S9]J. M. Duff, B. J. Faber, C. C. Hegna, M. J. Pueschel, and P. W. Terry. Effect of triangularity on ion-temperature-gradient-driven turbulence. *Physics of Plasmas*, 29(1), 1 2022.
- [S10]A. Marinoni, S. Brunner, Y. Camenen, S. Coda, J P Graves, X Lapillonne, A Pochelon, O Sauter, and L Villard. The effect of plasma triangularity on turbulent transport: modeling TCV experiments by linear and nonlinear gyrokinetic simulations. *Plasma Physics and Controlled Fusion*, 51(5):055016, 5 2009.
- [S11]Y. Camenen, A. Pochelon, R. Behn, A. Bottino, A. Bortolon, S. Coda, A. Karpushov, O. Sauter, G. Zhuang, and the TCV team. Impact of plasma triangularity and collisionality on electron heat transport in TCV L-mode plasmas. *Nuclear Fusion*, 47(7):510–516, 7 2007.
- [S12]G. Merlo, S. Brunner, O. Sauter, Y. Camenen, T. Görler, F. Jenko, A. Marinoni, D. Told, and L. Villard. Investigating profile stiffness and critical gradients in shaped TCV discharges using local gyrokinetic simulations of turbulent transport. *Plasma Physics and Controlled Fusion*, 57(5):054010, 5 2015.
- [S13]X. Garbet, P. Donnel, L. De Gianni, Z. Qu, Y. Melka, Y. Sarazin, V. Grandgirard, K. Obrejan, E. Bourne, and G. Dif-Pradalier. The effect of shaping on trapped electron mode stability: an analytical model. *Nuclear Fusion*, 64(10):106055, 10 2024.

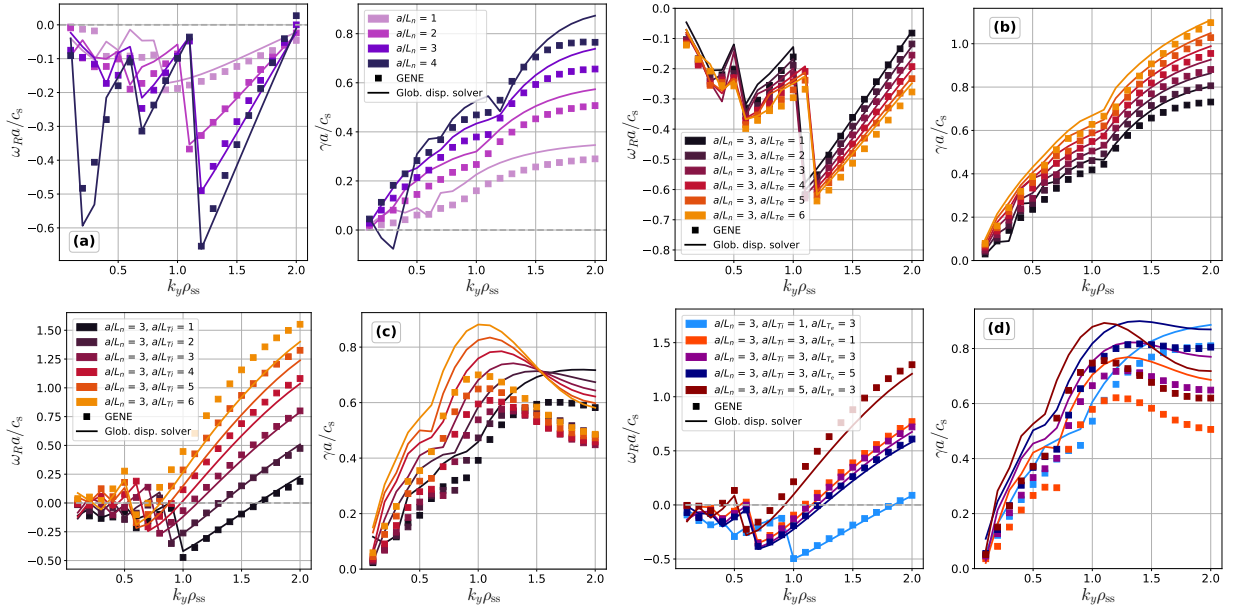


FIG. S11: Eigenfrequency solutions obtain by the global dispersion model (solid lines) contrasted with GENE simulations (symbols) for kinetic-electron scenarios in the negative mirror configuration of W7-X. Shown are results while varying (a) the density gradient a/L_n [both temperature gradients suppressed $a/L_{Ti} = a/L_{Te} = 0$], (b) the electron temperature gradient a/L_{Te} [suppressing ion temperature gradient $a/L_{Ti} = 0$], (c) the ion temperature gradient [suppressing electron temperature gradient $a/L_{Te} = 0$] and (d) both $a/L_{Ti}, a/L_{Te}$ corresponding to realistic non-flat kinetic profiles. In cases (b)-(d) with non-zero temperature gradients the density gradient is fixed at $a/L_n = 3$.